Analysis of Meso- and Microscale Hydrometeorological Fluxes in TERENO preAlpine using WRF-LES

Dissertation
zur Erlangung des Doktorgrades an der
Fakultät für angewandte Informatik
der Universität Augsburg

vorgelegt von

Cornelius Hald

Mai 2020

Erstgutachter: Prof. Dr. Harald Kunstmann
Zweitgutachter: PD Dr. Christoph Beck

Tag der mündlichen Prüfung: 02.12.2021

UNIVERSITÄT AUGSBURG

Abstract

Analysis of Meso- and Microscale Hydrometeorological Fluxes in TERENO preAlpine using WRF-LES

by Cornelius Hald

A Large-Eddy Simulation (LES) using the Weather Research and Forecasting (WRF) model is set up in a computationally efficient way, directly driving the single domain with reanalysis data as boundary conditions. The simulation represents two real episodes over a well-known and real area. It is shown that the model successfully produces turbulent structures as they are known from idealized LES in literature and that the inertial subrange of the turbulence spectrum is appropriately resolved. The simulated wind field is evaluated with measurements taken during the ScaleX-campaigns by a triple Doppler Lidar setup that can measure all three wind components with a high temporal and vertical resolution throughout the atmospheric boundary layer. Model results sufficiently recreate the measured wind speed and direction as well as the development of daytime and nocturnal boundary layers. The coarse spatial and temporal resolution of the boundary conditions limits the accuracy of the model, shown by the representation of low-level jets. A katabatic flow reveals that the model successfully produces local weather phenomena that are not present in the boundary conditions and proves that the model output can be considered as a four-dimensional representation of the flow structures for a known area. This is not achievable with measurements. The implementation of realistic soil information (moisture and temperature) allows for a simulation of the sensible and latent heat fluxes. The advantage of the model over measurements here lies in the possibility to evaluate the turbulent fluxes at every location and height and the chance to evaluate the dependence of the fluxes on the soil properties below. The presented setup can be used to gather in-depth knowledge of the small-scale flow structures in a known area or to generalize soil–atmosphere interactions for large–area climate models.

UNIVERSITÄT AUGSBURG

Zusammenfassung

Analysis of Meso- and Microscale Hydrometeorological Fluxes in TERENO preAlpine using WRF-LES

von Cornelius Hald

Die Dissertation beschreibt die Rechenzeit-effiziente Realisierung und Analyse einer *large eddy simulation* mit dem *Weather Research and Forecasting* Modell, bei der die meteorologischen Randbedingungen für die einzelne Domain direkt aus Reanalysedaten abgeleitet werden. Die Simulation erstreckt sich über zwei reale 48-Stunden lange Perioden in einem realen Gebiet. Das Modell produziert genau die turbulenten Strukturen, die aus idealisierten Simulationen aus der Literatur bekannt sind. Die *inertial subrange* ist deutlich zu erkennen. Messdaten von einem aus drei Doppler Lidar-Geräten bestehenden virtuellen Messturm, der die drei Windkomponenten in hoher zeitlicher und vertikaler Auflösung messen kann und während der ScaleX-Messkampagnen zum Einsatz kam, dienen zur Evaluierung des Modells. Gemessene Windgeschwindigkeiten und -richtungen werden im Modell gut abgebildet; die Grenzschichtentwicklung bei Tag und Nacht ist angemessen repräsentiert. Limitierungen zeigen sich in der Abbildung der gemessenen *low-level jets*, deren Genauigkeit durch die unzureichende räumliche und zeitliche Auflösung der Randbedingungen begrenzt ist. Am Beispiel eines katabatischen Kaltluftabflusses wird gezeigt, dass das Modell mikrometeorologische Phänomene erzeugt, die nicht aus den Randbedingungen stammen. Das bedeutet, dass die Modellergebnisse ein vierdimensionales Abbild der Strömungsverhältnisse in einem realen Gebiet darstellen. Mit Messungen ist das nicht erreichbar. Durch die Implementierung gemessener Bodenfeuchtigkeit und -temperatur in das Modell lassen sich realistische latente und sensible Wärmeströme berechnen. Im Modell können diese, im Gegensatz zu Messungen, an jedem Ort und in jeder Höhe bestimmt werden und die Abhängigkeit von der Bodenbeschaffenheit wird beschreibbar. Der gezeigte Modellansatz kann zur Untersuchung von kleinräumigen Strömungsmustern oder zur besseren Beschreibung kleinskaliger Effekte von Boden–Atmosphäre Wechselwirkungen in gröber aufgelösten Modellen verwendet werden.

Acknowledgements

At the end of the day, there is only one name for the author on the title page of such a doctoral thesis, but it's no secret that it takes the combined effort of many people to complete such a document. Some help with scientific information, other with strategical tips, some incite new ideas just through discussion, others make the Feierabend fun, and some just have an open ear when things don't go that well for a while.

Yet, there are a few people who were absolutely essential: A huge thanks goes to my supervisor / advisor team consisting of Harald Kunstmann, Patrick Laux and Matthias Mauder. Without you, I wouldn't have written a single line. Thanks for your input, your patience, your trust and your help and thanks for giving me the opportunity to work here in this innovative, inspiring, active and still relaxed environment here at IMK-IFU. Thanks also go to Matthias Zeeman, Benjamin Fersch, Ingo Völksch and Stefan Emeis for providing me the measurement data I needed and also for explaining the mode of operation of all the used devices. Special thanks to Matthias Zeeman for helping to get that paper through an exhausting review process.

Thanks go to the MICMoR graduate school, the steering committee and especially Elija Bleher, for financing my work and allowing me to travel to Vienna twice. MICMoR was not only the "pot of money" but also the opportunity to meet other PhD-students from all over the world.

Thanks go to all the people in my working group here, for all the short and long conversations in the hallway or the cafeteria, and to Verena Wedler for being the "good soul" of the group.

Thanks also go to Christoph Beck, Andreas Philipp and Jucundus Jacobeit from Uni Augsburg, who helped to spark my interest in all this science stuff, and without whom I might be doing something completely different with my life.

Thanks go to a multitude of Bachelor, Master and PhD students here at IMK-IFU, who were and are great friends. No names, because I'll forget someone.

Thanks also go to Christian Chwala for letting me work on one of his projects with enough time to finish my thesis.

Thanks to Gerhard Smiatek, my office buddy. Thanks for having an open ear in all situations!

And last (but not least) to Julia, who hated the long distance relationship even more than me, but gave me the time to finish. Thank you!

Contents

List of Figures

List of Tables

List of Abbreviations

ABL	**A**tmospheric **B**oundary **L**ayer
CBL	**C**onvective **B**oundary **L**ayer
DEM	**D**igital **E**levation **M**odel
DL	**D**oppler **L**idar
EBC	**E**nergy **B**alance **C**losure
EC	**E**ddy-**C**ovariance
HFX	sensible **H**eat **F**lu**x**
LES	**L**arge **E**ddy **S**imulation
LH	**L**atent **H**eat flux
LSM	**L**and **S**urface **M**odel
MO	**M**onin-**O**bukhov Similarity Theory
NBA	**N**onlinear **B**ackscatter and **A**nisotropy
NBL	**N**octurnal **B**oundary **L**ayer
PBL	**P**lanetary **B**oundary **L**ayer
RL	**R**esidual **L**ayer
SBL	**S**table **B**oundary **L**ayer
SGS	**S**ub**g**rid **S**cale
SMAG	**Smag**orinsky type SGS-model
TKE	**T**urbulent **K**inetic **E**nergy
TOS	**T**urbulent **O**rganized **S**tructure(s)
WPS	**W**RF **P**re-processing **S**ystem
WRF	**W**eather **R**esearch and **F**orecasting Model

Physical Constants

Gas constant of dry air	$R = 287.058\ Jkg^{-1}K^{-1}$
Gravitational constant	$g = 9.81\ ms^{-2}$
Specific heat capacity of dry air	$C_{p,d} = 1.005\ Jg^{-1}K^{-1}$
Specific heat capacity of water vapor	$C_{p,vap} = 2.02\ Jg^{-1}K^{-1}$
von Karman constant	$k = 0.4$ (dimensionless)

List of Symbols

$C_{d,h,q}$	bulk transfer coefficients from MO	[dimensionless]
$C_{1,2,b,s,e}$	NBA SGS-model coefficients	[dimensionless]
C_p	heat capacity of air at constant pressure	$Jg^{-1}K^{-1}$
$C_{p,d}$	heat capacity of dry air at constant pressure	$Jg^{-1}K^{-1}$
$C_{p,vap}$	heat capacity of water vapor at constant pressure	$Jg^{-1}K^{-1}$
e	turbulent kinetic energy (TKE)	$m^2\ s^{-2}$
F	kinematic momentum flux	$m\ s^{-1}\ m\ s^{-1}$
i, j, k	indices for coordinates, can be x, y, z	
K_h	eddy coefficient for heat	$m^2\ s^{-1}$
K_m	eddy coefficient for momentum	$m^2\ s^{-1}$
L	Obukhov length	m
L_v	latent heat released at phase change	$J\ kg^{-1}$
M	absolute horizontal wind speed	$m\ s^{-1}$
p	pressure	$hPa, mbar, N\ m^{-2}$
p_0	pressure at the surface	$hPa, mbar, N\ m^{-2}$
p_{qv}	water vapor pressure	$hPa, mbar, N\ m^{-2}$
p_{top}	pressure at the model top	$hPa, mbar, N\ m^{-2}$
$Q*$	net radiation	$W\ m^{-2}$
Q_H	kinematic heat flux	$K\ m\ s^{-1}$
$\overline{Q_H}$	dynamic heat flux	$W\ m^2$
Q_M	kinematic moisture flux	$kg\ kg^{-1}\ m\ s^{-1}$
$\overline{Q_M}$	dynamic moisture flux	$W\ m^2$
q_v	water vapor mixing ratio	$kg\ kg^{-1}$
q_*	moisture scale from MO	$kg\ kg^{-1}$
R	gas constant for dry air	$Jkg^{-1}K^{-1}$
R_{ij}	rotation rate tensor	$m^2\ s^{-2}$
Re	Reynolds number	[dimensionless]
Ri_b	bulk Richardson number	[dimensionless]
S_{ij}	strain rate tensor	$m^2\ s^{-2}$
T	absolute temperature	$K,^\circ C$
T_V	virtual absolute temperature	$K,^\circ C$
t	time	s
U	wind speed, east-west component	$m\ s^{-1}$
$U_{i,j,k}$	one wind component	$m\ s^{-1}$
u_*	friction velocity	$m\ s^{-1}$
V	wind speed, north-south component	$m\ s^{-1}$
W	wind speed, vertical component	$m\ s^{-1}$
w'	fluctuations of vertical wind	$m\ s^{-1}$
x, y, z	Cartesian coordinates	
z	height over ground / above sea level	m
z_0	roughness length	m
z_i	height of the boundary layer	m

Δ	generalized grid size	m
$\Delta_{x,y,z}$	model resolution in x, y, z direction	m
ζ	z/L, PBL height scale	[dimensionless]
Θ	potential temperature	$K,^\circ C$
Θ_v	virtual potential temperature	$K,^\circ C$
Θ_*	temperature scale from MO	$K,^\circ C$
κ	wave number	m^{-1}
ν	kinematic viscosity	$m^2\ s^{-1}$
ν_Θ	thermal diffusivity	$m^2\ s^{-1}$
ρ	density	$kg\, m^{-3}$
ρ_{air}	density of moist air	$kg\, m^{-3}$
Φ	geopotential	$m^2\ s^{-2}$
$\Phi_{h,m}$	similarity functions for temperature and momentum	[dimensionless]
$\psi_{h,m}$	integrated similarity functions	[dimensionless]

Chapter 1

Introduction

Almost all of human life takes place at the interface of earth's surface and the atmosphere. Here, both the large scale circulation of the atmosphere and the properties of the ground below influence a shallow part of the air hull around our planet that is called the atmospheric boundary layer (ABL).

Its properties are governed by a multitude of factors: The strength of the sun's radiation, the weather in the troposphere above, the nature of the ground, the vegetation on it and many more.

Due to its significance to human life it has been an object of many studies. Yet there is one property that complicates the investigation of the boundary layer, which is turbulence. When air moves over the ground it is slower near the surface than above. It begins to stumble and creates whirls. A similar process is happening when two layers of air with different speed or direction are above each other. This is called shear. Another origin of turbulence is buoyancy: Some surfaces are warmer than others and the air above these tends to rise. To balance the local pressure deficit it has to sink down at another place. At the interface the friction between rising and sinking air creates turbulence. Science has to this day not found a way to analytically describe turbulence. It can only be approximated.

The created turbulent structures are called eddys. Eddys are whirls of air and are present in all sizes. The largest in the boundary layer are as high as the layer itself. When those bump into each other or into obstacles like mountains, trees or buildings, they fall apart into smaller ones. The smallest are on the scale of millimeters, where they dissipate and transfer their kinetic energy finally into heat.

Turbulence in the boundary layer is the most prominent mechanism that governs the exchange of temperature, moisture, gases and aerosols between the surface and the air. Therefore, while being influenced by the large scale properties of weather and climate, it feeds back into these. Hence, to be able to forecast weather on a large scale, the interactions on the smallest scale have to be taken into account.

Weather forecasts are done with the help of computer models. In these models, the area of interest is discretized into grid boxes. Starting from initial and boundary conditions that come from measurements and other, often global models, changes within the model domain are calculated for discrete time steps. For every grid box, new values are calculated by using the surrounding values, and every grid box is in turn influencing its neighbors. One value, like temperature or wind speed is considered to represent the mean of this value within a grid box. Depending on the size of the box, this can be very coarse or very precise.

Picking the size of a grid box is always a trade off: With large and few boxes, a model can be calculated quickly and it can cover a large area. On the negative side, it will not be able to represent small scale features in the circulation. Mountains, for example, and the modifications they bring to weather through ridges, summits and valleys, can not be represented, if a grid box spans several dozens of kilometers in horizontal space and the elevation can only be represented by one number for the average elevation. Similarly, the turbulence present in the atmospheric boundary layer is too small to be explicitly resolved in such models. Its effects can only be parameterized.

Models with small grid boxes on the order of tens or hundreds of meters, on the other hand, can resolve small scale phenomena of the weather. The area can be properly described with much of its natural variability, and parts of the turbulence can be resolved. Yet, the smaller the grid boxes are, the smaller the area that can be treated by the model will become. Due to the complexity of the equations of motion that have to be solved, the required computing power rises exponentially.

If all scales of turbulence in the boundary layer, from the production range of sizes of hundreds of meters down to the dissipation range of millimeters, are of interest, a modeling approach called direct numerical simulation would have to be used. But the calculations within these models are so complicated that only very small areas could be considered, and even then, modern high performance computing systems would take so long for the calculations that the results will always be a hindcast instead of a forecast.

In between the two approaches of either parameterizing turbulence in the atmosphere or resolving it completely is a technique called large eddy simulation (LES). In such a simulation the grid boxes are on the order of 10 – 100 meters. Therefore, the larger portion of the turbulence, the large eddys, are explicitly resolved. Smaller eddys and the dissipation are parameterized by a subgrid-scale (SGS) model.

LES were introduced around 1970 (Deardorff, 1970; Deardorff, 1972), specifically as a tool for investigations of the boundary layer. Due to their complexity and the comparatively low available computing resources at that time, they were only applied to very idealized cases (e.g. Sommeria, 1976; Deardorff, 1980; Moeng, 1984). Represented were neutral stratifications over endlessly flat and homogeneous terrain. Only later the method was used for the more realistic stable (Mason and Derbyshire, 1990) and convective (Schmidt and Schumann, 1989; Mason, 1989) boundary layers. The insight gained about atmospheric turbulence through LES was used to improve the parameterizations for mesoscale weather models (e.g. Nieuwstadt et al., 1993; Andren et al., 1994).

Only around the year 2000, computing power became so readily available that LES were applied to more realistic cases, starting with valleys or patched surfaces (Albertson and Parlange, 1999; Bou-Zeid, Meneveau, and Parlange, 2004). Today it is possible to represent a grade of realism in LES that is only known from mesoscale weather models (Muñoz-Esparza et al., 2017; Rai et al., 2017). Yet, the time required for the solutions is way longer than real time, meaning that they are not used for forecasts but for case studies.

The LES for realistic cases are known to produce flow features that are very similar to those found in idealized studies, but that does not imply that the real flow follows the simulated patterns. To investigate this, a LES for a very well known region with substantial instrumentation is necessary. This provides the data that is needed to evaluate the model output and to make sure that the flow features are realistic.

Following the above, it is also possible with the appropriate instrumentation to measure the energy balance at a certain location, and to try and model it for the same region with LES. The knowledge derived from a small patch of land can then be transferred to larger regions and help to improve the climate modeling.

1.1 Objectives

The work presented in this study uses the LES capabilities of a weather model and applies them to an area that is, like described above, very well-known from a meteorological standpoint and is equipped with a wide variety of measurement systems for all kinds of variables.

Following the technical objectives of finding a working model configuration, a suitable period and measurements for the evaluation, four scientific questions will be treated:

- Is the LES capable of representing a real period over a real and well-known area?
- Can vertically resolved measurements of wind speed, taken from a virtual tower constructed with Lidar devices, be used to evaluate the model output?
- Can the simulation of realistic conditions successfully recreate the fluxes of latent and sensible heat?
- Which additional benefit has the spatially highly resolved representation of fluxes over point measurements or spatially averaged energy balances?

To find an answer to these questions, the model is set up in a way that requires comparatively low computing resources in order to keep the required time low and allow for more than one experiment to be carried out. In the next step it is ensured that the results of the simulations represent the typical LES results in terms of the development of turbulence. The third step is to validate the ability of the model to represent the measured large scale weather conditions while also allowing for local phenomena to develop. This is done by using measurement data as validation.

The innovation compared to other studies lies here in especially two points: First, the model setup is chosen in such a way that it is far more computationally efficient than comparable model setups, and second, the measurements used to evaluate the model data comes from a highly innovative measurement system consisting of three Lidar devices, that is able to provide high resolution wind measurements throughout the whole atmospheric boundary layer.

A part of the results has been published in 2019 under the title "Large-eddy simulations of real-world episodes in complex terrain based on ERA-reanalysis and validated by ground-based remote sensing data" by C. Hald, M. Zeeman, P. Laux, M. Mauder and H. Kunstmann in the journal *Monthly Weather Review*.

1.2 Structure

This work begins with introductions on the properties of the planetary boundary layer and the turbulence within (Chapter 2) and the mode of operation of large eddy simulations along with a review of the development of the method and the application of the EC-method to model data (Chapter 3). Chapter 4 describes the setup of the model along with the challenges that have to be navigated in order to find working settings. It also contains short descriptions of the *VirtualTower*, EC-station and *soilnet* measurement installations used to evaluate the model output. Chapter 5 contains the results of the conducted simulations and their discussion. It is split in sections on the general turbulence developments (5.1), comparisons with the *VirtualTower* (5.2) and the evaluation of the calculated fluxes (5.4). The document ends with a summary and outlook in Chapter 6.

Chapter 2

Description of the atmospheric boundary layer

The boundary layer is the lowest part of the atmosphere. Its mean depth is often given as about 1000 m (e.g Kaimal and Finnigan, 1994), but depending on time of the day and location on the earth it can vary from 100 m (e.g. Stull, 1988) up to 3000 m (e.g. Jacobson, 2005). Stull (1988, p. 2) defines it *as that part of the troposphere that is directly influenced by the presence of the earth's surface, and responds to surface forcings with a time scale of about an hour or less*. As the surface is, during the course of a day, reacting to the changing amount of sunlight that it receives, the boundary layer also shows a distinct diurnal cycle. This is shown in Figure 2.1.

For the explanation of the boundary layer dynamics, the concept of the potential temperature is beneficial. It is the temperature that air would have if it was brought to a reference pressure level, usually sea level pressure or 1000 hPa:

$$\Theta = T(\frac{p_0}{p})^{R/c_p} \tag{2.1}$$

Θ is the potential temperature, T the absolute air temperature as measured by a thermometer, p_0 is the reference pressure and p the pressure in the height where the absolute temperature is measured. R is the gas constant of air and c_p the specific heat capacity of air. R/c_p has the value 0.286.

As turbulence is air in motion, the weight or density becomes important. The heavier the air, the more energy is needed to move it. Water vapor has a lower density than air, so the more water vapor is in air, the lower the total density becomes. While the potential temperature removes the effect of pressure on temperature, the virtual potential temperature Θ_v removes both the effects of pressure and moisture. It is defined as the temperature that dry air would have if it had the same density as the observed moist air. It is therefore always higher than the potential or absolute temperature. If the air is not saturated it can be calculated as follows:

$$\Theta_v = \Theta \cdot (1 + 0.61 \cdot q_v) \tag{2.2}$$

where q_v is the mixing ratio of water vapor.

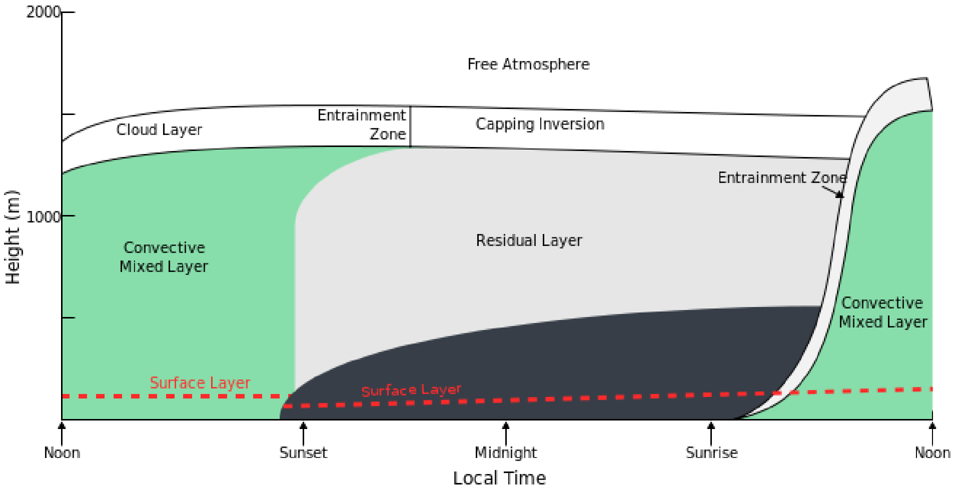

FIGURE 2.1: Temporal development of the atmospheric boundary layer. Modified after Stull (1988) by "NikNaks" and taken from `https://en.wikipedia.org/wiki/Planetary_boundary_layer#/media/File:Atmospheric_boundary_layer.svg`.

2.1 Temporal development

During daytime, while solar insolation is strong, the warm surface heats the air above, which is then warmer than its surroundings and subsequently starts to rise. The potential temperature gradient with height is negative. This unstable layering induces turbulence and mixes the properties of the air, the developing layer is called the *mixed layer* (green in Figure 2.1). Within the mixed layer, most properties are constant in the height profile due to the strong vertical mixing. The height of the mixed layer, z_i, is limited by an inversion at the top (i.e. a sudden increase in temperature) that separates it from the free atmosphere above that is not in the same way influenced by the ground. Exchange of air between these two layers is very limited. Turbulence produced by shear is one of the mechanisms that can mix air from the free troposphere in the boundary layer and vice versa. The stability of this boundary is often visible as the height where smog above polluted cities suddenly ends. Around sunset, the incoming solar radiation decreases and finally vanishes. The ground quickly begins to cool down and with it the air right above. This cool air is colder than the air above, so it will not rise but stay near the ground. This is called a stable layering, characterized by a positive gradient in potential temperature with height. Turbulence is dampened. A nocturnal boundary layer (NBL) develops. It grows in height during night due to the continued cooling. Above the NBL is a residual layer, the remains of the daytime boundary layer. Here, variables like humidity, temperature and pollutants are still well mixed, but without the energy input from the surface, the turbulence is dampened. The residual layer is characterized by neutral layering, meaning that potential temperature does not change with height. This layer is no longer influenced by the ground as it is shielded from below by the NBL. With sunrise at the next morning the ground quickly begins to heat up again. In theory, for a short moment the whole PBL is neutrally stratified up to the free troposphere and a real mixing with air from above can happen. In reality, the area with neutral stratification is moving from the ground upwards and the exact time when that happens is influenced by many factors, including the surface properties. With increasing solar radiation the strength of buoyancy grows and the layering becomes more and more unstable. Thermals rise up and start mixing the air from the former NBL and the residual layer. A new mixed layer develops.

Shown in Figure 2.1 with the red line is the *surface layer*, defined as the lowest 10% of the NBL or mixed layer (Stull, 1988). According to Kaimal and Finnigan (1994) its height is between 50 m and 100 m. Here, temperature, wind speed and humidity show the largest gradients. It is where the exchange processes between air and surface happen and where the conditions for the whole boundary layer are set.

2.2 Vertical profiles in the PBL

Depending on the time of day, variables in the boundary layer often show typical height profiles. These are different during day and during night. It was described above that the potential temperature is a good indicator for the state of the PBL. Wind speed and humidity also show characteristic profiles. The potential temperature profile of the daytime boundary layer shown in Figure 2.2 follows the outline given above. The heated soil warms the air above and gives it a strong gradient in the surface layer. Within the mixed layer, up to z_i, gradients are low and the air is well mixed. The PBL is limited on top by a stable layer. z_i is at the base of this stable layer. Its height is variable, which is why it is shown as a range in the figure. The wind speed has its lowest values in the surface layer, caused by the friction of the ground that decelerates the air. Due to its form when plotted it is often called a logarithmic wind profile. In the mixed layer the speed can vary due to changes in the meteorological drivers, but is relatively homogeneous within the layer. Above the PBL, speeds increase quickly to the speed of the geostrophic wind measured in the free atmosphere. Moisture shows a similar profile as the temperature: The highest gradient is in the surface layer where evaporation from the soil takes place. Almost no gradients are present in the mixed layer that reaches up to where moisture drastically drops, marking z_i.

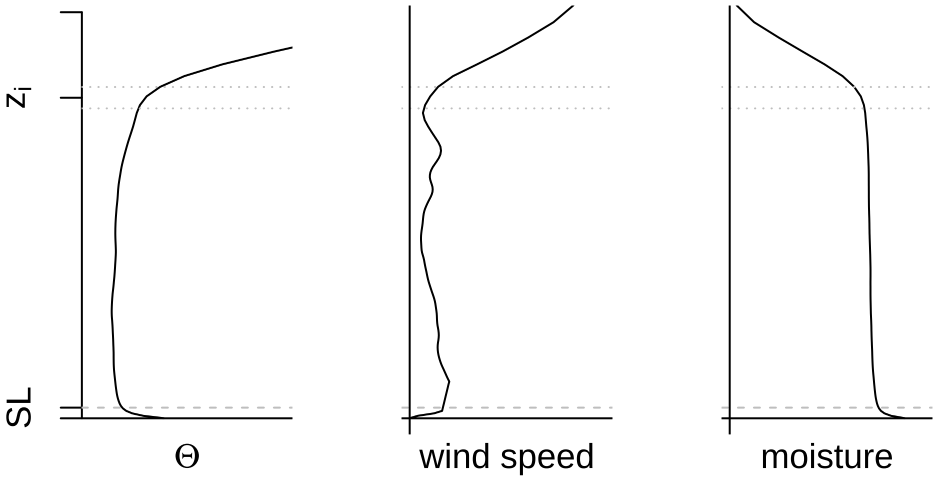

FIGURE 2.2: Height profiles of Θ, wind speed and moisture in the daytime boundary layer. SL is the height of the surface layer, z_i of the boundary layer. Data modified from LES.

At night, when the stable NBL is fully developed, the profiles look different (Figure 2.3). Air temperatures are lowest near the ground where they match the cool surface. They rise with height, forming the stable layering that defines the NBL. Above z_i the gradients are low. Here, the well mixed conditions from the mixed layer still prevail forming the residual layer. Like during day it is capped by an inversion with stable layering above which temperatures rise again. The wind speed shows its maximum in the lower troposphere at night often at the upper limit of the NBL where in many nights a low level jet (LLJ) forms. It can be described as a shallow sheet of fast moving air and can be caused by many factors, for example advection, orographic effects, land-sea breezes or inertial oscillations (Kraus, Malcher, and Schaller, 1985). Wind speed in the residual layer often matches the geostrophic wind above. Moisture profiles are most similar with daytime profiles. Total amounts are lower due to colder air and maximum values at the ground can be higher due to less mixing.

The profiles shown in Figures 2.2 and 2.3 are constructed using data from the large eddy simulations described later in this document. They therefore do not exactly correspond to those shown in textbooks. The real PBL is even more variable and measured profiles might therefore look very different.

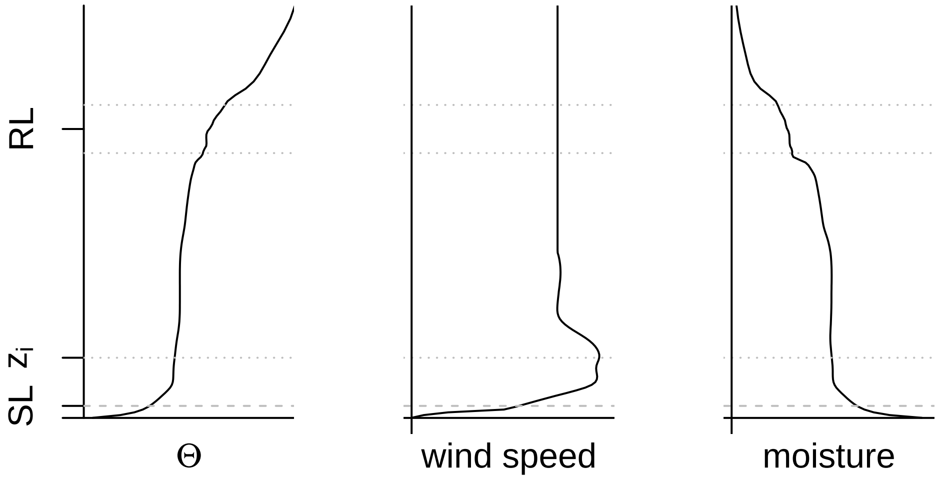

FIGURE 2.3: Height profiles of Θ, wind speed and moisture in the NBL. SL is the height of the surface layer, z_i of the boundary layer and RL the upper limit of the residual layer. Data modified from LES.

2.3 Determination of the PBL height

As described above, the potential temperature profile is a good indicator for the PBL height. According to Sullivan et al. (1998), z_i is where the gradient of the potential temperature with height is largest:

$$z_i(x, y) = z, \text{where } \frac{\delta\Theta(x, y, z)}{\delta z} \text{ is maximum} \tag{2.3}$$

x, y and z are coordinates in a Cartesian coordinate system. x is the east-west coordinate, y the north-south coordinate and z the height. This method is valid for the convective daytime boundary layer. It does not work in the NBL, because the largest gradients here are within the boundary layer itself. z_i is where the gradients decrease, showing the lower boundary of the residual layer. Therefore, the height of the NBL for this document is defined as the height where the gradient in potential temperature falls below 5% of the largest gradient measured below:

$$z_i(x, y) = z, \text{where } \frac{\frac{\delta\Theta(x,y,z)}{\delta z}}{(\frac{\delta\Theta(x,y,z)}{\delta z})_{max}} = 0.05 \tag{2.4}$$

There are other, more complex possibilities of determining z_i. Some can be found in Kaimal and Finnigan (1994) and in Sullivan et al. (1998). Another simple one is the definition of the PBL height by searching for certain thresholds in the temperature gradients (Wagner, Gohm, and Rotach, 2015).

2.4 Description of turbulence in the PBL

Turbulence in the atmosphere can be simply described as moving air. Moving air is expressed as wind. It is this wind that moves around the thermal energy that is temperature and other variables like moisture, trace gases, pollutants, pollen, particulate matter and many more. Wind itself contains kinetic energy (momentum).

On the large scale it is advective motions that change the concentration of all the variables mentioned above. On the spatial and temporal scales of the PBL, turbulence is the most important factor. Turbulence in the air, expressed as eddys, exists on all scales, spanning from thousands of meters and covering the PBL from top to bottom to millimeters. Turbulence is not separated from advection: eddys get advected by the mean wind. Due to the different time scales, it is possible to separate the turbulent from the advective parts of the wind. If U is the measured wind at a certain location, then

$$U = \overline{U} + u' \tag{2.5}$$

Here, $\overline{U}$ is the mean wind, where $(\overline{\ \ })$ marks a temporal mean and u' is the deviation from the mean. For a meaningful separation of the two parts the mean has to be calculated over a time in which the properties of the wind (speed and direction) vary as little as possible. Typical time windows are between 10 and 120 minutes.

The turbulent part of the wind transports temperature, moisture etc. Therefore, when measuring temperature for a period of time during which an eddy is advected along the thermometer, it is conceivable that the measured temperature at the front side of the eddy is different from the temperature at the back side. These differences can also be considered deviations from a mean temperature. Therefore, this decomposition can be performed for other quantities in the same manner, e.g. $\Theta = \overline{\Theta} + \Theta'$

2.4.1 The energy cascade in the atmosphere

If wind measurements are taken at the same location over several weeks or months in a very high temporal resolution of a second or smaller, one could imagine plotting this as a time series. The wind speed in Figure 2.4a shows large fluctuations within the shown three months, but on closer inspection certain periods appear: Mean high and low wind speeds changing with a period of about a week can be associated to the changes from high to low pressure influence. This cycle was shown to be present in climate data measurements at stations by Laux and Kunstmann (2008) but could not be confirmed in an evaluation of circulation patterns (Beck, 2012). Fluctuations on the scale of a day are caused by the diurnal cycle.

In Figure 2.4b the wind speed for only one day is shown. A clear difference between night and day is visible, but it is overlaid by fluctuations on smaller time scales of some 10 minutes and even on these fluctuations there are others on the scale of single minutes. These fluctuations are the eddys measured as they pass by the sensor. Longer periods in the fluctuation mean large eddys and shorter mean smaller eddys. If the resolution of the sensor is high enough, fluctuations on the order of fractions of seconds can be measured, the smallest scale of eddys in the atmosphere on which they dissipate into heat.

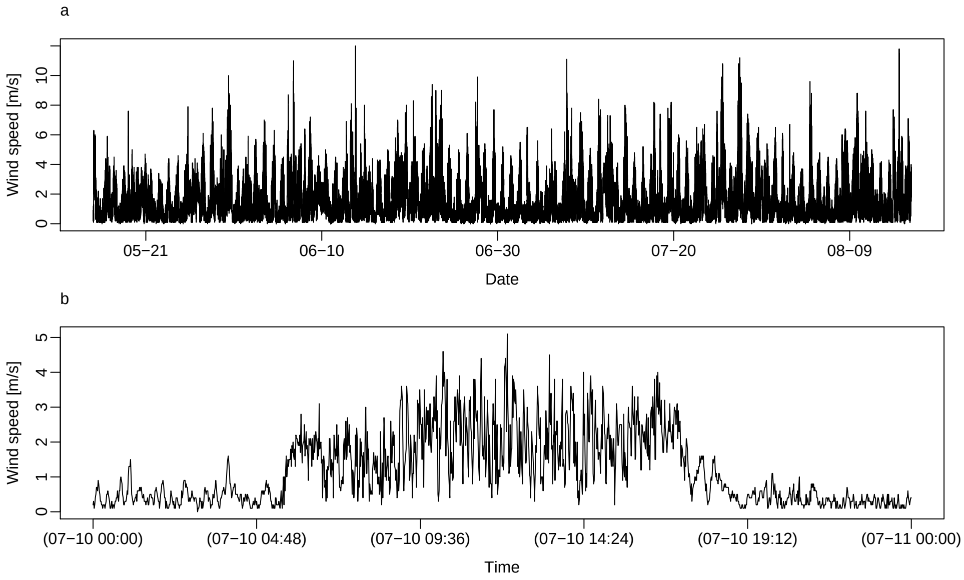

FIGURE 2.4: Time series of measured wind speeds, (a) spanning three months and (b) spanning one day. One data point per minute. Data from M. Zeeman.

Time series like these can be treated with a *Fourier Analysis*. This suggests that all the fluctuations present can be represented by the sum of an infinite row of sine and cosine functions. These functions have certain wavelengths or frequencies. Those frequencies can then be translated into a spectral domain and displayed. This then shows how much energy is present in the time series at a certain frequency.

One of the first of such spectra for wind in the atmosphere was produced by Van der Hoven (1957) and is shown in Figure 2.5. Three distinct peaks are visible. The one to the left with a periodicity of around 100 hours represents the change of high and low pressure systems. The smaller, second peak at cycles of around 20 hours represents the day and night cycle. On scales of single hours is what was called a spectral gap. The third peak on a periodicity of single minutes stands for the turbulence of the PBL. This spectrum was created using measurements from near the ground. Stull (1988) notes that there are actually motions of scales of an hour, like convective events leading to local cloud formation. This implies that the spectral gap is an artifact of the measurement. As described in Rotach et al. (2015), the assumption of a spectral gap is especially wrong in mountainous terrain, where orographic effects can induce motions of periodicity between a day and an hour.

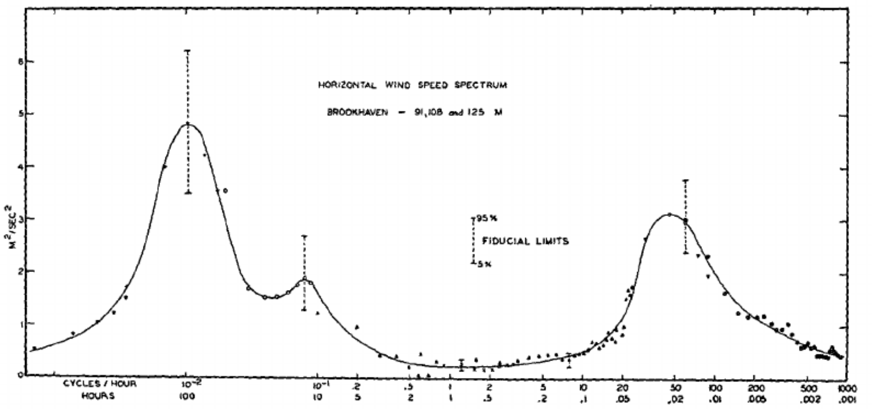

FIGURE 2.5: Idealized spectrum of horizontal wind speeds by Van der Hoven (1957). The three peaks represent, from left to right, frontal systems, the diurnal cycle and turbulence.

As the focus of this chapter is on the turbulence in the PBL, Figure 2.6 shows an idealized spectrum of turbulence taken from Kaimal and Finnigan (1994); κ is the wave number, $E(\kappa)$ is the energy spectral density or the energy contained in the turbulence of a certain wave number. The left and low-frequent part of it can be seen as the right side of the spectral gap shown in Figure 2.5. The turbulence spectrum is divided into three parts: (A) is the production range. On this scale, energy of any form (thermal, kinetic, potential etc.) in the atmosphere is transferred into turbulent energy, eddys are produced. (C) is the dissipation range, where the turbulent energy is dissipated into heat and the very small eddys disappear. (B) represents the inertial subrange. Eddys on this scale are believed to be isotropic and very similar to each other. Here, no new turbulent energy is produced or dissipated, but the energy is just passed down from larger to smaller and smaller eddys. In a logarithmic presentation the inertial subrange is parallel

TABLE 2.1: Kinematic fluxes

Name	Symbol	Units
heat	$Q_H = \Theta U$	$[K \cdot \frac{m}{s}]$
moisture	$Q_M = qU$	$[\frac{kg_{water}}{kg_{air}} \cdot \frac{m}{s}]$
momentum	$F = U_i U_j$	$[\frac{m}{s} \cdot \frac{m}{s}]$

to a line of the represented wave numbers to the power of –(5/3).

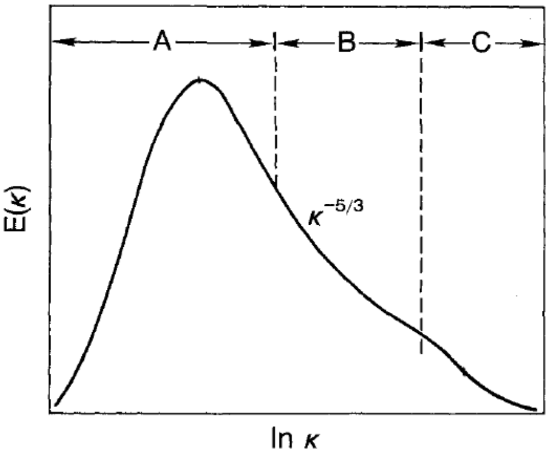

FIGURE 2.6: Idealized spectrum of turbulence by Kaimal and Finnigan (1994). A is the production range, B the inertial subrange and C the dissipation range.

2.4.2 Kinematic fluxes

The transport of heat, moisture and momentum can be expressed as a flux. Flux is the transport of a quantity through a specified area over a specified time. Yet, quantities like momentum or heat are not easily measured (Stull, 1988), but quantities like wind speed, temperature and moisture are. Fluxes in the PBL are therefore usually expressed as kinematic fluxes, which are the products of wind speed and the quantity in question. They are presented in Table 2.1

These kinematic fluxes can be multiplied with the density of air, ρ_{air}, and in the case of heat, with the air density and the specific heat of air ($\rho_{air} \cdot c_{p,air}$) to reach the dynamic flux. The kinematic momentum flux can be separated into three components, the indices i and j here can take the meaning of one of the three wind directions in Cartesian coordinates x, y and z. Corresponding to these three directions, wind is usually, and will in this document, be described with the letters U, V and W, describing the east-west,

TABLE 2.2: Turbulent fluxes

Name	Symbol
vertical turbulent heat flux	$\overline{w'\Theta'}$
vertical turbulent moisture flux	$\overline{w'q'}$
vertical turbulent momentum flux	$\overline{w'u'}$

north-south and vertical component. The three components of the kinematic momentum flux are then UV, UW and VW.

The fluxes described above are the total fluxes. As described in Equation 2.5, quantities can be separated in mean and turbulent parts. Using this, advective and turbulent fluxes can be described.

While being the smallest of the three wind components in terms of absolute value, w' is the most important part in turbulent transport. The vertical wind connects the soil with the atmosphere, transporting heat and moisture up and momentum down. Averaged over long periods and large surfaces, $\overline{W} = 0$. What is then measured are the turbulent parts of the vertical wind, w'. This turbulent part is responsible for the turbulent exchange in the PBL. The respective turbulent fluxes are therefore the covariance of the turbulent part of the quantity and the turbulent part of the vertical wind speed (see Table 2.2).

The time span to average the fluxes over is the same that the deviations and the mean were calculated in. Turbulent horizontal fluxes can be determined accordingly by switching w' with u' or v'. Units for these kinematic fluxes are the same as above.

2.4.3 Stresses in the PBL

When looking at the momentum fluxes described above, it shows that they are the representation of two wind directions (e.g. up and forward). When considering a cube of air at a random location, it can happen that air with different momentum fluxes is present in said cube. These differences lead to a deformation of the imaginary cube, the momentum exercises a stress on it.

Two different stresses are important in the turbulence of the PBL: Reynolds-stress and viscous stress. Reynolds stress describes the deformation due to several different directions present in the cube. Depending on where the direction and speed is different, a different face of the cube will be deformed. This deformation can be in three directions, x, y and z, depending on which wind vector is present (u, v, w). It can happen in all three Cartesian directions of the cube, resulting in three by three possible realizations of the Reynolds stress. Therefore, it is a tensor with nine elements, called $\tau_{Reynolds}$:

$$\tau_{Reynolds} := \begin{bmatrix} \overline{u'u'} & \overline{u'v'} & \overline{u'w'} \\ \overline{v'u'} & \overline{v'v'} & \overline{v'w'} \\ \overline{w'u'} & \overline{w'v'} & \overline{w'w'} \end{bmatrix} \tag{2.6}$$

Since this is a symmetrical matrix, there are six unique elements that describe the Reynolds stress. Reynolds stresses are a property of the flow, i.e. they only occur when a fluid is in motion.

Viscous stresses work on a molecular level and can be imagined as the friction working on molecules when shear is present between two layers of air. As this can also work in all three Cartesian directions of an imaginary cube of air, it is like the Reynolds stress described in a Tensor with nine total and 6 unique elements. It uses the symbol τ_{ij}, where ij can take any combination of the Cartesian coordinates x, y and z. Viscous stresses are a property of the fluid.

The magnitude of the viscous stress depends on the viscosity of air, which is very small. Therefore, the viscous stress is smaller than the Reynolds stress. The ratio of inertial to viscous stress is often given in terms of the Reynolds number (Stull, 1988):

$$Re = \frac{VL}{\nu} \tag{2.7}$$

V and L are in this case typical velocity and length scales. In the PBL, a typical velocity is on the order of 5 m s^{-1} and the length scale is 100 m. ν is the kinematic viscosity, which in the case of air takes the value of $1.5 \cdot 10^{-5}$ m^2 s^{-1}. The Reynolds number for the PBL is therefore very large; a typical value is 10^8 (Kosović, 1997).

2.4.4 Important scaling parameters in the boundary layer

Along with the boundary layer height z_i (see Section 2.3), there are other useful scaling variables that are used for investigations of the PBL. They are calculated from the values measured near the ground in the surface layer.

The first, z/z_i, is the quotient of a height where a quantity is measured and z_i. This allows for an easy comparability of values from different boundary layers.

There is also the friction velocity u_*. It is a velocity scale that is valid for the surface layer (Stull, 1988). It represents the wind stress (Reynolds stress) close to the ground and varies with the surface properties and the wind speed (Kaimal and Finnigan, 1994). It can be expressed through the total vertical flux of horizontal momentum at the surface, $\overline{u'w'_s}$ and $\overline{v'w'_s}$ where the subscript s stand for surface. The friction velocity is defined as:

$$u_*^2 = [\overline{u'w'_s}^2 + \overline{v'w'_s}^2]^{1/2} \tag{2.8}$$

u_* usually takes values between 0 and 0.5 m s^{-1}.

The Obukhov length (Monin and Obukhov, 1954) can, according to Stull (1988), be interpreted as the height over the surface where turbulence is no longer be mainly produced by shear (which is the main factor in the surface layer due to the strongly varying wind speeds in the logarithmic wind profile), but by buoyancy:

$$L = \frac{-\overline{\Theta_v} u_*^3}{kg(\overline{w'\Theta'_v})_s} \tag{2.9}$$

Here, k is the von Karman constant, a dimensionless number of empirical origin that is given the value 0.4 and is used for describing the logarithmic wind profile in the surface layer. g is the gravitational constant and $\overline{w'\Theta'_v}_s$ the kinematic turbulent flux of virtual potential temperature at the surface. The Obukhov length uses the assumption that the flux is constant with height.

Dividing the height of a measured quantity by L creates another possibility of comparing different boundary layers. This new scale, z/L, is often given the symbol ζ:

$$\zeta = \frac{z}{L} \tag{2.10}$$

It is also possible to calculate a ratio of the boundary layer height and the Obukhov length, z_i/L. This quantity can take a wide range of values, mostly depending on the value of L. While z_i is always positive, L can be both positive and negative: it is negative when the turbulent kinematic heat flux at the surface is positive, or directed upwards. It can obtain positive values when the flux is negative or directed downwards. As a result, z_i/L is positive when the boundary layer is stable and turbulence dampened. During day and unstable layering, the value is usually negative. Slightly negative values ($0 > z_i/L > -10$) hint at turbulence due to shear, while lower values are reached when buoyant forces are strong (e.g. Deardorff, 1972; LeMone, 1973).

2.5 Summary

The properties of the PBL described in this chapter have an idealized character. Especially the scaling variables rely on a multitude of assumptions. They require uniform and endlessly flat ground where surface fluxes are identical at every point. They do not consider any changes in weather conditions. The statistical properties of turbulence are fixed and fluxes are the same in every height. Changing solar radiation or condensation of moisture are not considered. Scientists were especially looking for areas that resemble these conditions when the first measurement campaigns on boundary layer turbulence were conducted. They found them in remote locations in USA (e.g. Lettau and Davidson, 1957; Izumi, 1971; Stull and Eloranta, 1984), Australia (e.g. Clarke and Brook, 1979) and Russia (Kaimal and Finnigan, 1994).

Obviously, these locations are very rare and not at all representative of most of the earth's surface and weather. Reality is characterized by varying surfaces with vegetation that is spanning over flats, hills, mountains and valleys of all shapes and forms. Dry and moist spells of weather follow in quick succession.

This study will therefore also contain statements on how well the theory above describes reality and how well the parameters can be applied to conditions that deviate strongly from the ideal ones they were derived in. For this purpose, a LES, whose mode of operation is based on the findings from ideal conditions, is applied to a real area. This real area is, as part of the TERENO infrastructure (see Section 4.4 for details), equipped with a multitude of measurement systems, meaning that the parameters necessary for turbulence evaluation are known for this area.

Chapter 3

Large Eddy Simulation

This chapter describes the functionality of large eddy simulations and their history. LES are a way of describing turbulent motions in fluids. One application is the simulation of the motions of air in the atmosphere. As described in Chapter 2, turbulence in the atmosphere is happening on all scales. Due to the nature of turbulence, a comprehensive description would require solving the governing equations on all spatial and temporal scales.

Even with modern computing systems it would not be possible to do this for the extents that the PBL exhibits (Sorbjan, 2004). LES therefore only simulates the larger scales of turbulence explicitly, i.e. it calculates the exact motion of large eddys as they appear and move depending on external or other resolved factors. These eddys are the ones that have irregular shapes due to boundary effects and they transport most of the energy present in the PBL. The smaller scales are considered to be close to isotropic and similar to each other. Hence it is sufficient for a complete description of the PBL to model these small eddys. This is done by expressing the motions on the small scale in terms of their average effect. Following the spectrum of atmospheric turbulence shown in Section 2.4, LES aims to explicitly resolve the production range and the inertial subrange. The dissipative range is modeled.

Numerical computer models on all scales discretize the volume in question in grid boxes and calculate the quantities of interest for these volumes. One calculated value can be considered as the mean of the grid volume. By making these grid points smaller, the solution becomes more exact but the whole domain size decreases when the computational effort is to be kept constant. Therefore, every numerical model is a trade-off between the extent of the considered volume and the precision of the results per grid point.

To resolve the turbulence in the PBL, grid points have to be in the order of 1 to 100 m in horizontal size, depending on the stability. If the resolution, or the size of a single grid point is Δx, then the smallest resolved eddy is in the order of $2\Delta x$, because it takes at least the data from two grid points to identify a rotating motion. Since vertical motions are one of the most important factors for boundary layer turbulence, the vertical resolution is often taken as about a third of the horizontal resolution. The total volume has to at least extent to the top of the boundary layer in the vertical and five times this height in the horizontal (e.g. Moeng et al., 2007).

3.1 Equations for the description of the PBL

The following equations are a subset of all the equations necessary to describe the state and changes in the atmosphere or the PBL. They are explained here in a little detail to point out what differentiates a LES from other atmospheric circulation models where turbulence is not considered in detail. Comprehensive descriptions of these models can, for example, be found in Jacobson (2005) and Pielke Sr (2013).

The presented equations have been invented, modified and compiled by a multitude of scientists over several centuries. For their derivations, the reader is referred to the standard works on the fundamentals of physics.

For the following equations, the indices i, j, k can take the values 1, 2, 3, representing the three Cartesian directions. Einstein summation notation is used.

3.1.1 The ideal gas law

This describes the state of a gas in terms of pressure, temperature and density.

$$p = \rho_{air}\, R\, T_v \tag{3.1}$$

where p is the pressure, ρ_{air} the density of moist air, R the gas constant for dry air and T_v the virtual absolute temperature.
This equation can be separated into mean and fluctuating parts as well. Since pressure fluctuations are very small they can usually be neglected in the boundary layer, leaving, after applying other simplifications and approximations:

$$\frac{\rho'}{\overline{\rho}} = -\frac{\Theta_v'}{\overline{\Theta_v}} \tag{3.2}$$

Using this simplification, the density needed for further calculations can be substituted by using the temperature which is much easier to be measured. The performed simplifications are described in Stull (1988).

3.1.2 Conservation of mass

The conservation of mass is described by a continuity equation:

$$\frac{d\rho}{dt} + \rho\frac{\delta U_j}{\delta x_j} = 0 \tag{3.3}$$

where t is the time and U_j the wind vector in x_j direction.
Assuming typical length and speed scales of the boundary layer it can be shown (Businger, 1982) that the pressure fluctuations are negligible. Using this incompressibility approximation, the conservation of mass is reduced to:

$$\frac{\delta U_j}{\delta x_j} = 0 \tag{3.4}$$

3.1.3 First law of thermodynamics

The first law of thermodynamics describes the conservation of heat. There are many forms of this equation, but one that can be used for the sake of reaching a description of the properties of LES is:

$$\begin{array}{ccccc} \frac{\delta\Theta}{\delta t} & +U_j\frac{\delta\Theta}{\delta x_j} & = \frac{\nu_\Theta\delta^2\Theta}{\delta x_j^2} & -\frac{1}{\rho C_p}\frac{\delta Q_j^*}{\delta x_j} & -\frac{L_v E}{\rho c_p} \\ \\ I & II & III & IV & V \end{array} \tag{3.5}$$

- Term I is the storage of heat.
- Term II is the advection of heat.
- Term III describes the molecular conduction of heat where ν_Θ is the thermal diffusivity.
- Term IV stands for the effects of incoming radiation on temperature. Q^* is the net radiation.
- Term V describes the temperature changes due to phase changes of water in the air.

3.1.4 Conservation of momentum

The momentum equation is another equation that describes the conservation of energy, in this case the conservation of kinetic energy:

$$\begin{array}{cccccc} \frac{\delta U_i}{\delta t} & +U_j\frac{\delta U_i}{\delta x_j} & = -\frac{1}{\rho}\frac{\delta p}{\delta x_i} & -2\epsilon_{ijk}\Omega_j U_k & -\delta_{i3}g & -\frac{\delta\tau_{ij}}{\delta x_j} \\ \\ I & II & III & IV & V & VI \end{array} \tag{3.6}$$

- Term I describes the storage of momentum.

- Term II describes the advection of momentum.
- Term III are the forces exercised by pressure gradients.
- Term IV stands for the Coriolis forces caused by the rotation of the earth. For an in-depth explanation see for example Jacobson (2005).
- Term V describes the gravitational effects on momentum, where δ_{ij} is the Kronecker Delta. It takes the value 1 if the indices are different, and 0 if they are identical.
- Term VI stands for the viscous and Reynolds stresses described in Section 2.4.3.

3.1.5 Other equations

Depending on the area of interest, similar equations to that of the conservation of heat can be established that describe other scalars. One important is that for the transport of moisture in the atmosphere. Others can describe the behavior of certain gases, for example carbon dioxide, methane or nitrous oxides as some of the most important greenhouse gases. Stull (1988) shows the similarities and specifics of these equations.

3.1.6 Filtering of the equations

The equations described above can be used for all scales of the motions in the boundary layer, if x_j and t are chosen according to the scale in question. In LES, not all scales are resolved and the focus is on the large turbulent motions. The small effects therefore have to be removed from the equations, which basically means applying a low-pass filter (e.g. Kirkil et al., 2012):

$$\overline{\phi}(x) = \int_{-\infty}^{\infty} G(x-y)\phi(y)dy \tag{3.7}$$

where ϕ is any quantity and $\overline{\phi}$ its filtered form.

There are several forms the filter kernel can take. Three typical ones are box, Gaussian and a Fourier expansion (Leonard, 1975). When it is mentioned at the beginning of Chapter 3 that a calculated value in a model represents the average of a grid box, this implies the application of a box-shaped filter. For such models, this filter is the most used (Sorbjan, 2004):

$$\overline{\phi}(x) = \frac{1}{2\Delta}\int_{x-\Delta}^{x+\Delta} \phi(y)dy \tag{3.8}$$

Δ depends on the size of the grid boxes (e.g. Kosović and Curry, 2000):

$$\Delta = (\Delta_x \cdot \Delta_y \cdot \Delta_z)^{1/3} \tag{3.9}$$

The steps to get from the general equations of motion to their filtered form involve the separation into average (resolved) and fluctuating (non-resolved) parts and Reynolds averaging them. Also, often a simplification called the *Boussinesq-Approximation* is applied. This implies that the fluctuations of the density are so small when they are not caused by gravity that they can be ignored. So, after filtering the equations for the conservation of mass, heat and momentum take the following form:

$$\frac{\delta \overline{U_j}}{\delta x_j} = 0 \tag{3.10}$$

$$\frac{\delta \overline{\Theta}}{\delta t} + \frac{\overline{U_j} \delta \overline{\Theta}}{\delta x_j} = \frac{\nu_\Theta \delta^2 \overline{\Theta}}{\delta x_j^2} - \frac{1}{\overline{\rho} C_p} \frac{\delta \overline{Q_j^*}}{\delta x_j} - \frac{L_v E}{\overline{\rho} C_p} - \frac{\delta(\overline{u_j' \Theta'})}{\delta x_j} \tag{3.11}$$

$$\frac{\delta \overline{U_i}}{\delta t} + \overline{U_j} \frac{\delta \overline{U_i}}{\delta x_j} = -\delta_{i3}\, g + f_c\, \epsilon_{ij3}\, \overline{U_j} - \frac{1}{\overline{\rho}} \frac{\delta \overline{P}}{\delta x_i} + \frac{\nu \delta^2 \overline{U_i}}{\delta x_j^2} - \frac{\delta(\overline{u_i' u_j'})}{\delta x_j} \tag{3.12}$$

Upon closer examination there are few differences to Equations 3.4, 3.5 and 3.6: Mainly the variables are now representing the filtered, resolved or averaged values that can be calculated in a grid based model. Additionally, the equations for the conservation of heat and momentum now contain one additional last term. They represent the effects of the motions on a scale that are smaller than the filter. Both are turbulent fluxes (for momentum, the viscous stress of the resolved motions is separated and written in the second to last term). It is not possible to derive prognostic equations for these covariances from the resolved motions which is why they can not be simulated but have to be modeled. This is what the subgrid scale modeling is for.

3.1.7 Subgrid-scale modeling

The parts of the equations that can not be solved prognostically are $\overline{u_j' \Theta'}$ and $\overline{u_i' u_j'}$. They represent the effects of the small scale, the non-resolved turbulence on the whole budget. The easiest way to solve them is to claim that these effects are a property of the large and resolved scale multiplied with a scalar that accounts for the small size of turbulence:

$$\overline{u_j' \phi'} = -K \frac{\delta \overline{\phi}}{\delta x_j} \tag{3.13}$$

where ϕ is the quantity of interest. K is called eddy coefficient or eddy viscosity with the unit [m^2 s^{-1}]. The eddy coefficient for heat (K_h) and momentum (K_m) are different, while that for most other scalars is equal to that of heat. For very easy applications, where energy exchange due to phase changes of water in the air is not considered, this model is sufficient for the effects of the unresolved scale on heat. If phase changes are important, the model becomes substantially more complicated and can be found in Sorbjan (2004).

For momentum, this model is too simple and will not produce any motions or effects that resemble turbulence. The first model that was proven to work and that is still used in many of today's applications is that of Smagorinsky (1963):

$$\overline{u_i'u_j'} = -2K_m(\overline{S}_{ij} - \frac{1}{3}\overline{S}_{kk}\delta_{ij}) \tag{3.14}$$

$\overline{S}_{ij}$ is here the resolved part of the stress caused by air moving into different directions, often called strain:

$$\overline{S}_{ij} = \frac{1}{2}(\frac{\delta \overline{u_i}}{\delta x_j} + \frac{\delta \overline{u_j}}{\delta x_i}) \tag{3.15}$$

This still leaves K as the unknown in the equation. It was also suggested by Smagorinsky (1963) that K could be determined the following way:

$$K = (c_{s,\Delta}\Delta)^2|\overline{S}| \tag{3.16}$$

Δ is here determined by the grid size of the simulation as shown in 3.9. $c_{s,\Delta}$ is a parameter that has to be determined experimentally. The first value was given by Lilly (1967). Later modifications for the use in LES were, for example, introduced by Deardorff (1970) and Mason (1994).

Another approach presented by Deardorff (1980) relates the value of K_m to the subgrid-scale turbulence e' that has to be calculated in an additional prognostic equation. It is in turn related to the turbulence kinetic energy (TKE) e, defined as:

$$e = \frac{1}{2}({u'}^2 + {v'}^2 + {w'}^2) \tag{3.17}$$

The eddy coefficient for momentum is then:

$$K_m = (c_{e,\Delta}\Delta)\sqrt{e'} \tag{3.18}$$

Deardorff (1980) defined $c_{e,\Delta}$ with a value of 0.1.

The described SGS-models determine the effects of small scale turbulence through the motions of the resolved scale. These approaches are often called Smagorinsky-type models (SMAG). There is no feedback from the small to the large scale. Additionally, the value for c is set as a constant and kept throughout a simulation. Later SGS-models work with dynamic determinations of c (e.g. Germano et al., 1991), allow backscatter of energy from the small to the large scale (Kosović, 1997, described in Section 3.3) or match the filter size depending on the size of the turbulent structures (e.g. Bou-Zeid, Meneveau, and Parlange, 2005). Others are mentioned in the following Section 3.2.

The main purpose of SGS-models is to represent the turbulence in the dissipation range. The resolved motions produce the kinetic energy in turbulence and pass it through the inertial subrange. On the subgrid scale, the energy is then dissipated into heat.

3.2 Development of LES and its applications

The development of the LES method is closely linked to the development of computers. Solving the differential equations presented above requires substantial processing power. Not surprisingly, the first experiments of Lilly (1967) fall in a time when computing systems became available to a wider range of users, for example universities.

LES can be used for turbulent flows of all liquids and therefore has a strong community in the field of hydrodynamics as well. Here, however, only atmospheric applications will be covered.

The birth of LES for the simulation of boundary layer flows is closely linked with the work of James Deardorff, who presented the first LES for a neutrally stratified boundary layer over flat and homogeneous terrain (Deardorff, 1970). It used, as most others later, cyclic or periodic boundary conditions, meaning that the conditions at the outflow side of the model are being used as new input on the inflow side. Deardorff extended the method to convective boundary layers (Deardorff, 1972) and found that turbulence takes different three-dimensional shapes depending on stability. Neutral and convective boundary layers were the focus of LES research in the first years. Only under these conditions, turbulent structures are large enough that they can be simulated with the available amount of grid points, limited by computing power, while still covering the vertical extent of the PBL.

The next experiments were done with a heated surface, giving a constant positive heat flux from the ground into the PBL (Deardorff, 1974). This was representing the conditions found during a measurement campaign, allowing for a comparison of the results. Sommeria (1976) included equations for the treatment of water vapor into Deardorff's framework, allowing the formation of clouds in his experiments.

This was picked up by Deardorff (1980), simulating a cloud-covered PBL and also presenting the SGS model that uses the turbulence kinetic energy for the prediction of subgrid stresses (see Section 3.1.7).

The work was continued by Moeng (1984) who wrote a new LES model, using the recently described algorithms for fast Fourier transformations (FFT) to construct a grid in a pseudospectral representation. This model was, among others, applied in Moeng (1986) and Moeng (1987) on a stratus-topped boundary layer with weak convection.

Mason (1989) and Schmidt and Schumann (1989) simulated the CBL with different computer codes. Both noticed the same structures in the spatial distribution of buoyancy-created turbulence: Large patches of downdrafts, often called cells, are surrounded by narrow bands of updrafts. The upward motions are generally faster than the downdrafts. Mason (1989) also noticed that the diffusivity of turbulent energy in Smagorinsky-type models is too low near the ground, showing the rising focus of research on the surface layer and the boundaries between air and surface. Under conditions where both shear and buoyancy act as producers of turbulence, Moeng and Sullivan (1994) found elongated vortex-like structures in their simulations that are orientated parallel to the mean wind direction. These rolls were first described from measurements by LeMone (1976).

A little later one of the first studies on the application of LES to a stable boundary layer was presented by Mason and Derbyshire (1990). The authors showed that the general method can be applied to stable conditions if enough grid points are available for the representation of small eddys. They also noticed that the Smagorinsky-type SGS models with their coefficients determined for the use in neutral or convective conditions are too dissipative in this case. They remove the energy so quickly that turbulence is dampened almost completely.

Up to here, all presented studies were conducted over flat and homogeneous terrain. This was changed in Hechtel, Stull, and Moeng (1990), where a regularly patched inhomogeneous ground was simulated by prescribing different surface heat fluxes. The authors could not find, due to the chosen patch size, any effects of the patches on the development of a CBL. A different approach was chosen by Walko, Cotton, and Pielke (1992) who first considered uneven terrain. In their model domain with sinusoidal hills they found a tendency for updrafts to originate on the hilltops, while downdrafts were more likely to be found in the valleys.

As was noted above, several authors noticed shortcomings of the SGS-model with a constant value for $c_{S,\Delta}$. It had to be changed depending on the stability criteria to reach reasonable dissipation. To alleviate this, Germano et al. (1991) developed a new SGS-model that dynamically computes the coefficient depending on subgrid-scale and resolved turbulent stresses. It showed good results in boundary layers with shear, near walls and during transitions between stability regimes. The importance of the chosen SGS-model was further illustrated by one of the first LES comparison studies by Nieuwstadt et al. (1993). The four used computer codes showed little differences in the resolved motions, but large differences in the subgrid part in the simulated CBL case without geostrophic winds. In a similar study on a case with strong horizontal winds (Andren et al., 1994), these results were confirmed.

Another approach for a new SGS-model was outlined in Mason and Thomson (1992) and further discussed in a LES method review article by Mason (1994). The coefficient in SMAG models has to represent all scales of eddys smaller than the filter, with all their different effects, near the surface as well as in the mixed layer. In the surface layer the distribution of eddy sizes is different than further up, leading to different effects. The authors here suggest to implement stochastic variations of the effects of subgrid stresses. This then also allows for backscatter, describing the transport from energy from a small (subgrid) scale back to resolved turbulence. During the same time, Sullivan, McWilliams, and Moeng (1994) described yet another alternative SGS-model: Here, the Smagorinsky form is kept and the TKE approach is used to calculate the eddy viscosity (Deardorff, 1980). Additionally, the model includes information about the mean flow and it lessens the influence of turbulent fluctuations at the ground. This model is shown to produce wind profiles that better match the ideal logarithmic wind profile for the surface layer. Even when used for a simulation of the SBL (Andren, 1995), the produced wind profiles show the required characteristics. Under stable conditions with high horizontal wind speeds it produces conditions in which a low-level jet can develop (Saiki, Moeng, and Sullivan, 2000).

Circulation models allow for a technique called nesting. Nesting describes putting a domain with a relatively smaller resolution into a domain with coarser resolution. The finer resolution allows for more precise results in the area of interest. The solutions from the coarse domain feed into the fine domain and drive the grid points here. This is called *one-way nesting*. If, in turn, the fine domain also feeds its results back to the coarse domain it is called *two-way nesting* (general discussion on the differences in Harris and Durran, 2010). The first nested LES was described by Sullivan, McWilliams, and Moeng (1996). Their two domains have the same horizontal size to be able to keep periodic boundary conditions, but the vertical is nested. This results in a higher resolution near the ground. Here they find the nesting especially beneficial, while no significant improvements are observed in the mixed layer.

In Sorbjan (1996) something that could be described as a temporal development of a PBL is investigated for the first time. The author varies the temperature gradient with height in a way that it represents the time during the progressing afternoon. This adds another evaluated property of a realistic PBL after the investigations on non-flat surfaces and varying surface properties. The author later continued the research on this topic and simulated the growth of the PBL from morning to afternoon with an increasing heat flux from the surface (Sorbjan, 2007). The morning transition from a stable NBL to a daytime CBL is shown in Beare (2008).

Kosović (1997) presented another SGS-model. It enables backscatter, uses non-linear behavior of the SGS motions and its anisotropic shape. It is therefore aptly called *Nonlinear backscatter and anisotropy* (NBA). As it is used in the simulations presented in this work, further information can be found in Section 3.3.3. In a comparison with other SGS-models it shows good results (Kosović and Curry, 2000). The model was later implemented into the WRF model by Mirocha, Lundquist, and Kosović (2010). A SGS-model using Lagrangian averages for the calculation of the constants leading to the eddy coefficients was presented by Bou-Zeid, Meneveau, and Parlange (2005). It is supposed to bring improvements over inhomogeneous terrain. Later, the model was extended to not only model SGS stresses but also fluxes by Stoll and Porté-Agel (2006). Another approach is shown in Chow et al. (2005): They use a smooth filter larger than the grid size filter to reconstruct a resolvable part of the motions smaller than the filter. It is applied to the flow around a real hill in Chow and Street (2009). Comparisons with the Smagorinsky type models in the NBL can be found in Ludwig, Chow, and Street (2009). A much simpler SGS-model is that of Basu and Porté-Agel (2006), where the coefficients are calculated dynamically based on only resolved temperature and velocity field.

LES have been shown to be able to represent the turbulence in the PBL, yet operational weather models could not and still can not be run in LES resolutions to produce the forecast for the next day. They rely on parameterizations for the effects of turbulence. Here, LES is a powerful tool for deducting the statistical effects of turbulence in order to use them for mesoscale models. One such approach is shown in Siebesma et al. (2003) where the conditions during a cumulus capped boundary layer are simulated with ten different LES frameworks. The results are used for improvements of the parameterizations for the cloud formation in mesoscale models. Some of the used codes are described in Cuxart, Bougeault, and Redelsperger (2000) and Cuijpers and Duynkerke (1993). The oldest in the list is the one of Moeng (1984) presented earlier. Better parameterizations for the stable BL are derived from LES in Huang and Bou-Zeid (2013) and formulated and implemented in Huang, Bou-Zeid, and Golaz (2013).

Near the surface, the turbulent eddys are smallest. Therefore, the SGS-model has to do more work here. An investigation on how well SGS-models perform here depending on the ratio of energy in the vertical velocity and the filter width can be found in Sullivan et al. (2003). The energy contained in the vertical wind depends on stability and distance from the ground.

Following the work of Hechtel, Stull, and Moeng (1990), where no influence of surface patches could be found, Shen and Leclerc (1995) showed that only patches larger than z_i influence the structure of the boundary layer, while smaller patches only influence the statistics of the simulated turbulence. Albertson and Parlange (1999) showed that the average surface stress is higher when the patches of different roughness are smaller. Avissar et al. (1998) combined different surface characteristics with height gradients in order to simulate an observed boundary layer. They found that the simulated eddys do not dissipate quickly enough under the convective conditions when using the TKE SGS closure. In Bou-Zeid, Meneveau, and Parlange (2004) different surfaces are defined by their roughness. A simulation for a neutral PBL was used to find the *blending height*, the height in which turbulence has mixed the properties originating from different surfaces well enough that the surface structure is no longer visible. Sühring and Raasch (2013) conducted a similar study for the convective boundary layer.

Parameterizations for turbulence in mesoscale models are used when the filter applied to the equations is much larger than the eddys. The model is a LES when the filter is much smaller than the large eddys. For the range in between, no modeling approach exists. To bridge this gap, or *terra incognita*, Wyngaard (2004) developed a SGS model for these scales. Shin and Hong (2013) describe how local and non-local mixing terms have to be included in this range by comparing 50 m LES with gradually coarser simulations up to 4000 m. Wagner, Gohm, and Rotach (2014) approach the problem from the other direction and compare LES of an idealized valley with simulations of the same area using kilometer-scale resolutions. They show that the coarse models miss most of the small scale motions due to the fact that they cannot reproduce the terrain features. The circulations within the valley are further described in Wagner, Gohm, and Rotach (2015).

The first intercomparison study of LES for the stable boundary layer is shown in Beare et al. (2006). Computing power now is sufficient and the SGS-models are educated enough to be used on the small turbulent eddys under stable conditions. The simulations presented here are run in a resolution of 2 m and compared to measurements. It was later shown by Sullivan et al. (2016) in simulations for the same conditions that refining the resolution to below 1 m still brings improvements.

Many authors have shown in their LES studies that the modeling approach is able to represent features of a real PBL when the sources or reasons for these features are implemented. Examples are different surfaces, varying elevation, moisture and the formation of clouds and temporal development. The next step is taken by Botnick and Fedorovich (2008) who initialize their simulations not with ideal but with measured profiles of temperature and wind. They do keep the periodic boundary conditions. Bou-Zeid et al. (2009) show that LES can be used to simulate the turbulence that is generated by flow around buildings. Their effects are studied in a neutral PBL on flat terrain.

One of the first studies using the LES capabilities of the Weather Research and Forecasting model (WRF, see Section 3.3) can be found in Moeng et al. (2007). The simulated cases are a neutral and a convective PBL over flat terrain and with periodic boundary conditions, closely resembling the beginnings of LES. The innovation lies in the application of WRF's nesting capabilities to LES: The periodic boundary conditions drive a LES with 150 m resolution. Within the domain is a nest with a resolution of 50 m. This nest is only fed by the outer domain and in turn, feeds its results back to the coarser domain (*two-way-nesting*). The authors notice that the mean of the vertical velocity is not zero, contradicting theory and measurements. They attribute this to the nest being too small for the largest eddys, resulting in the hint that the nest should be at least five times the PBL height in horizontal length. WRF-LES has also been used to study the development over an idealized valley under two forcing wind speeds (Catalano and Moeng, 2010). Height gradients are easily implemented in WRF. With several simulations of the neutral PBL, Hattori et al. (2010) show that the horizontal resolution in such a case has to be 50 m or better in order to resolve most of the turbulence under these conditions. Crosman and Horel (2012) used WRF-LES to simulate the circulations that originate from the different heat fluxes over land and water, called land-sea-breezes. The high resolution also allows for an investigation of lake breezes. This builds on earlier work by Antonelli and Rotunno (2007). With the easy availability and convertibility of WRF it was quickly used for many LES applications, motivating the first comparison of SGS-models by Kirkil et al. (2012). Under neutral conditions over flat surfaces and ideal valleys, the more complicated approaches performed better than the simple Smagorinsky type formulations.

WRF uses terrain-following coordinates (see Section 3.3). In high resolution simulations like LES with realistic terrain this can lead to numerical instabilities. To overcome this, Lundquist, Chow, and Lundquist (2010a) developed an immersed boundary method that is using a different kind of grid. The method is applied to a real hill (the same as in Chow and Street,

2009) in Bao, Chow, and Lundquist (2018).

With computing power becoming so easily available in the second decade of the 21st century, the studies using LES grew significantly. The focus from this point on is therefore on studies that motivated or influenced the experiments presented in this document. The outer domain is driven by reanalysis data. Results are compared to point measurements. Similar studies on other areas are shown in Muñoz-Esparza et al. (2017) and Rai et al. (2017). Here, turbulence metrics are investigated as well, pointing to the WRF problem of underdeveloped turbulence at the nest's inflow edges discussed later. Comparison of meteorological conditions with measurements show good agreement. Due to the nesting and parameterizations used, these simulations are computationally very expensive. Similarly to the development of WRF-LES from a mesoscale model to LES, this way was also gone with the ICON model (Zängl et al., 2015). The implemented LES capabilities (Dipankar et al., 2015) are extensively investigated in Heinze et al. (2017). Sub-kilometer simulations for the whole country of Germany during real periods are compared against mesoscale model output, other dedicated LES simulations and measurements. The LES shows much more detail in the simulated conditions.

Since WRF started as a mesoscale weather model, the implemented ways of calculating motions and parameterizing meteorological effects are not designed for the use in LES. WRF solves the fully compressible equations (c.f. Section 3.1). This is fine for motions of long periodicity, but pressure fluctuations on very small temporal scales, as they are present in LES, result in sound waves. Yamaguchi and Feingold (2012) show that these waves can lead to faster than realistic dissipation of clouds. They also show that some assumptions in the microphysics models that treat moisture in the air and phase changes of water can lead to unwanted release of latent heat. Gibbs and Fedorovich (2014) compare WRF-LES to the results of a specialized LES code (based on the one described by Nieuwstadt, 1990). They show that WRF attributes more energy to the larger eddys and that the simulations therefore produce less spatial variability.

The turbulent motions in the PBL are the driving mechanism for all exchange processes between surface and atmosphere. With the eddys resolved, a LES can show how all kinds of substances are distributed under turbulent conditions. Klose and Shao (2013) show how dust is mobilized by eddys. Chu et al. (2014) and Xue et al. (2016) discuss the dispersion of silver iodide and how it effects the development of clouds. In Nunalee, Kosović, and Bieringer (2014) the authors use WRF-LES to simulate the motions of plumes carrying sulfur hexafluoride around a mountain. Lang, Gohm, and

Wagner (2015) show how the presence of complex terrain features modifies the dispersion of pollutants in the PBL.

The nesting of LES in WRF is further investigated in Mirocha et al. (2013). Since the model does not transfer information about turbulence from the coarser to the finer domain, areas of underdeveloped turbulence at the inflow edge can be found. The paper investigates how quickly new turbulence develops using different SGS models. Both domains are LES, simulating a neutral BL. A similar investigation by Muñoz-Esparza et al. (2014b) nests LES in LES for a convective offshore boundary layer. Mirocha, Kosović, and Kirkil (2014) investigate how LES domains nested into mesoscale domains behave while simulating neutral and weakly convective PBLs. Results show that variability in the surface properties and convective conditions favor the development of turbulence in the LES domains. Muñoz-Esparza et al. (2014a) suggest implementing temperature fluctuations at the inflow boundaries to enhance the development of turbulence at the step from mesoscale to LES resolution. The used WRF-LES was, up to this time, only able to nest horizontally, meaning that the vertical size of the grid points is equal in all domains. The first version of a vertical nesting capability is presented in Daniels et al. (2016). The latest developments in improving the development of turbulence at the domain edges are shown in Muñoz-Esparza and Kosović (2018).

The growing demand for renewable energy resulted in the use of LES for the simulations of wind parks to investigate how the turbines influence each other. For this reason, Mirocha et al. (2014) implemented a module for the representation of turbines into WRF-LES, which is tested by Aitken et al. (2014) during the presence of a stable PBL. The general WRF setup for such cases was discussed in Lundquist, Mirocha, and Kosovic (2010). Earlier studies (Liu et al., 2011) used simulated wind fields in wind turbine rotor height to forecast energy yields.

A weakness of all available LES is still the coupling between surface and atmosphere. Just above ground the gradients in many quantities are so large that they cannot be represented in a discrete grid box. Udina et al. (2016) show that the usually used Monin-Obukhov (MO) similarity theory (details and limitations in Section 3.3.2) can not represent heat transfer by molecular thermal conduction. Basu and Lacser (2017) note that MO should not be used when the lowest model level is within the roughness sublayer. The roughness sublayer is the lowest part of the surface layer, defined by the height of the elements in it that define its roughness. Very recent developments show that MO could be substituted by using generalized canopy models that are normally used to simulate the flow within urban or forest canopys (Arthur et al., 2019).

This overview shows how the LES method developed: In the beginning, it was a very idealized framework for understanding the nature of turbulence. Only the simplest cases with stationary boundary layers, flat and homogeneous surfaces and periodic boundary conditions were investigated. The focus was on developing the method and improving the statistics given by the SGS models. With time, authors increasingly tried to approximate effects found in the real PBL in their simulations: patchy surfaces, hills and valleys, changing incoming radiation, meteorological boundary conditions that represent real weather. Yet, all these properties were tested individually, leaving still most of the drivers idealized. Only recently, studies emerged that really tried to represent real episodes over realistic terrain. They have in common that they, due to the nesting routines involved, require enormous amounts of computing power. The purpose of the following sections and chapters in this dissertation is to show that realistic conditions in a LES can be reached on lower computational costs.

3.3 LES in the Weather Research and Forecasting model

The Weather Research and Forecasting (WRF) model has been developed since the second half of the 1990's and is still receiving regular updates. It is the successor of the MM5 model and has been replacing it since around 2005. A comprehensive overview of the model structure and components is available in Skamarock et al. (2008). It is distributed as source code and therefore can be used on many different computing systems and environments. Additionally, it allows for user-based modifications and implementation of user-based additional modules. WRF is a framework that allows experiments, forecasts and case studies for meteorological and climatological cases from global scales, over regional applications for continents or single countries, down to the LES scale of meters. An idealized mode is available for sensitivity and similar studies. The code can be run in parallel on many systems with distributed or shared memory.

The model code is non-hydrostatic, meaning that vertical motions are computed by using the equation for momentum. A hydrostatic mode is also available. Time integration is accounted for by a third-order Runge-Kutta scheme (Wicker and Skamarock, 1998; Wicker and Skamarock, 2002), for horizontal and vertical advection, finite difference schemes of 2nd to 6th order are available. WRF does not apply the Boussinesq-Approximation (see Section 3.1.6) and calculates pressure changes. This can lead to acoustic and other waves (Moeng et al., 2007; Gibbs and Fedorovich, 2014) that can lead to problems when they are reflected of the domain's or nest's boundaries. To cope with the waves, the model applies three-dimensional divergence damping, vertically integrated horizontal divergence damping, and semi-implicit acoustic step off-centering (Skamarock et al., 2008).

The included pre-processing system WPS can be used to produce boundary conditions, representing an ideal or a realistic setting.

3.3.1 Grid structure of WRF-LES

WRF and WRF-LES both use the same Arakawa-C grid structure (Arakawa and Lamb, 1977, shown in Figure 3.1). This is a grid that is staggered in the horizontal and vertical direction. Staggered means that not all variables are defined on the same point in the grid. In Figure 3.1, E is the center point of the grid and x, y and z are the Cartesian coordinates. Defined at the grid center are quantities like pressure, moisture, temperature and TKE. The horizontal wind components are defined at their respective surfaces, marked with U and V in the figure, or $\Delta x/2$ and $\Delta y/2$ away from the center, where Δx and Δy are the resolutions in those two directions. The vertical wind W and the geopotential are defined at the top and bottom surfaces of the grid box. According to Pielke Sr (2013), this staggering simplifies the solving of the governing equations in a finite difference scheme and it increases the effective resolution of the model by a factor of two. Collins et al. (2013) note that vertical staggering allows for an easy implementation of two important boundary conditions at the model top: No vertical wind speed and no vertical flux.

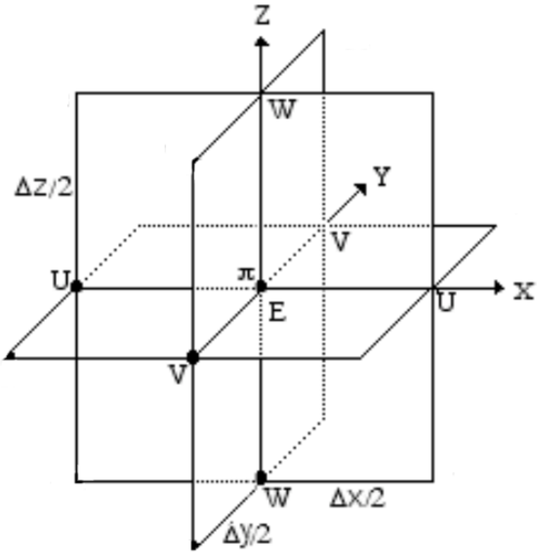

FIGURE 3.1: Schematic of the Arakawa-C grid used in WRF (modified after Sorbjan, 2004)

The Arakawa-C grid is defined in a terrain-following way: The lowest grid point is always on the surface. This allows for an easy implementation of height gradients in the surface (Lundquist, Chow, and Lundquist, 2010a). In WRF, the height levels are additionally defined by pressure, with the lowest level of any x, y location having the pressure at the ground as value. This approach was first described by Phillips (1957) who introduced the σ-level-coordinate, where $\sigma = p/p_0$. p is the pressure in the selected height and p_0 the pressure at the ground. The resulting height levels lie between 1 at the surface and 0 at the top of the atmosphere. Since it is not always necessary to model the whole atmosphere up to 0 hPa, the formulation used in WRF is

$$\sigma = \frac{p - p_{top}}{p_0 - p_{top}} \tag{3.19}$$

where p_{top} is the pressure at the model top.

Figure 3.2 shows an example for the terrain-following coordinates and also shows another property of the grid used in WRF, which is vertical stretching. With increasing height, the vertical extent of a grid box increases. In a LES application, this permits having a very high resolution in the boundary layer to resolve turbulence and having a coarser resolution above in order to keep the total amount of vertical levels small. The figure also shows where the weakness of the grid lies: over steep slopes the orthogonality of grid surfaces is no longer given (Lundquist, Chow, and Lundquist, 2010b), resulting in problems when computing horizontal pressure gradients (Janjić, 1989) or horizontal advection (Schär et al., 2002). If slopes are too steep, the model will either be inaccurate or even unstable.

3.3.2 Monin-Obukhov Similarity Theory for the first model level

The finite difference scheme used in WRF to solve the differential equations expresses the δx as the difference in the value between two or more adjacent grid points. Hence, it requires boundary conditions that are set by different mechanisms than the Navier-Stokes equations. Lateral boundary conditions in typical weather models are either periodic (conditions at the outflow side are copied to the inflow side), open (outflow and inflow can happen on all sides), closed (air can only be moved within the domain) or specified (input at the inflow side is specified by data). Conditions for the upper boundary are mentioned in Section 3.3.1. To specify the lower boundary conditions, representing the surface layer, WRF uses Monin-Obukhov (MO) similarity theory (Monin and Obukhov, 1954). It is used to calculate the quantities in the lowest model level.

Through empirical evidence (Kaimal and Finnigan, 1994) it was shown that turbulence in the surface layer can be described with only four variables:

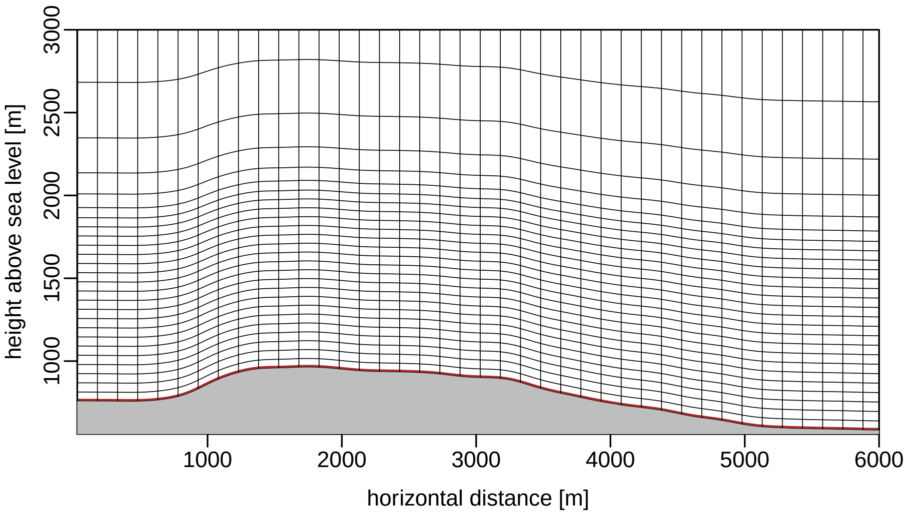

FIGURE 3.2: Terrain following coordinates used in WRF

These are z as the height over ground, u_*, the friction velocity as defined in Equation 2.8, the buoyancy parameter g/Θ_0 and the surface heat flux Q_H (Khanna and Brasseur, 1997). Analogous to the friction velocity, a temperature scale and a moisture scale can be created: $T_* = Q_H/u_*$ and $q_* = Q_M/u_*$. Together, these scaling variables can be used to construct the Obukhov length as shown in Equation 2.9. With T_* and L there are two parameters present that make a statement of stability, both depending on the sign of the surface heat flux (Stull, 1988).

Monin-Obukhov similarity theory now states that many atmospheric parameters (gradients, variances and covariances) in the surface layer become only dependent on z/L when they are made dimensionless and normalized by the required powers of u_* and T_* (Sorbjan, 1986). The coefficients necessary to calculate the non-dimensional forms are taken from experiments and are shown for example in Businger et al. (1971), Dyer (1974) and Caughey, Wyngaard, and Kaimal (1979). With these relationships, many parameters in the surface layer in their respective height can be described by only knowing the Obukhov length.

Originally, MO was constructed and used to derive quantities that are hard to measure like fluxes or covariances. Through taking measurements of e.g. temperature and wind speed at a convenient height, the whole surface layer could be described. Yet, the relationships work in both ways, so MO can also be used to derive temperatures and wind speeds if other necessary variables are known. This is often the case in modeling: By applying

MO to known surface properties coming for example from a land-surface model (LSM), temperatures and wind speeds in the surface layer can be constructed which then serve as lower boundary conditions for the atmospheric model.

In most LES, MO is at least used to calculate the vertical flux of horizontal momentum, $\overline{u_i'w'}$ in the surface layer by using the resolved wind speed in the lowest model level (e.g. Schmidt and Schumann, 1989). This implies the calculation of u_* as well. Idealized setups try to recreate a certain stability of the PBL. This can be done by specifying a surface heat flux (e.g. Stoll and Porté-Agel, 2006; Mirocha, Kosović, and Kirkil, 2014) or by having MO calculate the heat flux from a given soil temperature (e.g. Catalano and Moeng, 2010; Muñoz-Esparza et al., 2014b; Udina et al., 2016). In more realistic setups, where fluxes from the surface are calculated by a LSM, MO is providing momentum flux and u_* and couples the LSM to the atmospheric part (Talbot, Bou-Zeid, and Smith, 2012).

MO was invented using bulk relationships of atmospheric properties that are only valid over very homogeneous, flat surfaces. This theoretically limits its application when modeling inhomogeneous, hilly terrain, because the ensemble means for the flow variables from MO are applied to an instantaneous realization of the turbulent flow (Arthur et al., 2019). The surface momentum flux, for example, does not represent the observed level of fluctuations (Marusic, Kunkel, and Porté-Agel, 2001). Bou-Zeid, Meneveau, and Parlange (2004) note that MO should only be used above a blending height, where features of the ground no longer are represented in the flow. According to Raupach (1979) it should also not be used over forest canopies because their structure enhances turbulence compared to a flat surface. Sullivan, McWilliams, and Moeng (1994) find better agreements in their simulated wind profiles with MO under strongly convective conditions than during strong shear. Accordingly, Brutsaert (1998) argues that MO can be used over heterogeneous surfaces as well, because the mixing effects of turbulence are so strong that the bulk relations hold true. Despite of its age, MO is still the preferred technique in LES to couple the surface and the atmosphere. No alternatives have been found so far.

WRF offers several implementations of MO, yet they are generally based on the formulation in the MM5 model (Grell, Dudhia, Stauffer, et al., 1994). WRF describes the fluxes in the surface layer as follows:

$$\overline{u'w'}_s = u_*^2 = C_d M^2 \tag{3.20}$$

$$Q_H = u_* \Theta_* = C_h M (\Theta_a - \Theta_g) \tag{3.21}$$

$$Q_M = u_* q_* = C_q M (q_g - q_a) \tag{3.22}$$

Here, M is the horizontal wind speed in the lowest model level ($\sqrt{u^2+v^2}$), Θ_a and q_a are potential temperature and specific humidity in the lowest model level and Θ_g and q_g on the surface. C_d, C_h, C_q are dimensionless bulk transfer coefficients (Stull, 1988). It is these transfer coefficients that are determined by MO. To do this, two relationships are used: The dimensionless wind shear Φ_m and the dimensionless temperature gradient Φ_h (e.g. Kaimal and Finnigan, 1994):

$$\Phi_m(\frac{z}{L}) = \frac{kz}{u_*}\frac{\delta M}{\delta z};\ \Phi_h(\frac{z}{L}) = \frac{kz}{\Theta_*}\frac{\delta\Theta}{\delta z} \tag{3.23}$$

If these are integrated with respect to z, the dimensionless groups are separated in two parts (Jiménez et al., 2012):

$$M = \frac{u_*}{k}[ln(\frac{z}{z_0}) - \psi_m(\frac{z}{L}) + \psi_m(\frac{z_0}{L})] \tag{3.24}$$

$$(\Theta_a - \Theta_g) = \frac{\Theta_*}{k}[ln(\frac{z}{z_0}) - \psi_h(\frac{z}{L}) + \psi_h(\frac{z_0}{L})] \tag{3.25}$$

where $\psi_{m,h}$ are the integrated similarity functions and z_0 is the roughness length that is determined by the average height of rough elements on the surface.

If the contribution of $\psi_{m,h}(z_0/L)$ is neglected, the bulk transfer coefficients can be determined:

$$C_d = \frac{k^2}{[ln(\frac{z}{z_0}) - \psi_m(\frac{z}{L})]^2} \tag{3.26}$$

$$C_h = \frac{k^2}{[ln(\frac{z}{z_0}) - \psi_m(\frac{z}{L})][ln(\frac{z}{z_0}) - \psi_h(\frac{z}{L})]} \tag{3.27}$$

The integrated similarity functions are calculated depending on the stability that is determined by the bulk Richardson number Ri_b, which describes the ratio between temperature gradient and wind speed gradient:

$$Ri_b = \frac{g}{\Theta_a} z \frac{\Theta_{v,a} - \Theta_{v,g}}{M^2} \tag{3.28}$$

Four stability regimes have been identified by Zhang and Anthes (1982): $Ri_b \geq 0.2$ represents stable nighttime conditions, $0 < Ri_b < 0.2$ is damped mechanical turbulence, $Ri_b = 0$ is forced convection and $Ri_b < 0$ represents free convection.

This formulation of MO has been developed further by Jiménez et al. (2012) who included similarity functions for strongly stable (Cheng and Brutsaert, 2005) and unstable (Fairall et al., 1996) conditions and determined L iteratively (Muñoz-Esparza et al., 2014b). Another approach is shown in Janjić (1996), where an additional viscous sublayer is assumed in order to use the surface skin temperature instead of the air temperature for determining the gradient.

3.3.3 The Nonlinear Backscatter and Anisotropy model as SGS model

Additionally to the SGS formulations by Smagorinsky (1963) and Deardorff (1980) described in Section 3.1.7, WRF-LES contains the nonlinear backscatter and anisotropy (NBA) model by Kosović (1997). The motivation for the development comes from the finding that turbulence near bounding surfaces is inhomogeneous, which results in anisotropy and backscatter of TKE. Both could not be represented in the old SGS-models. The problem of anisotropy arises mainly in shear driven boundary layers and leads to unrealistic wind profiles.

Implemented (Mirocha, Lundquist, and Kosović, 2010) were two formulations that are based on either the strain rate or on the TKE, as are the two presented Smagorinsky type models:

$$\begin{aligned}\overline{u_i'u_j'} = &-(C_s\Delta)^2[2(2\overline{S}_{mn}\overline{S}_{mn})^{1/2}\overline{S}_{ij}\\ &+ C_1(\overline{S}_{ik}\overline{S}_{kj} - \frac{1}{3}\overline{S}_{mn}\overline{S}_{mn}\delta_{ij}) + C_2(\overline{S}_{ik}\overline{R}_{kj} - \overline{R}_{ik}\overline{S}_{kj})]\end{aligned} \tag{3.29}$$

$$\begin{aligned}\overline{u_i'u_j'} = &-C_e\Delta\{2(e)^{1/2}\overline{S}_{ij} + (\frac{27}{8\pi})^{1/3}C_s^{2/3}\Delta\\ &[C_1(\overline{S}_{ik}\overline{S}_{kj} - \frac{1}{3}\overline{S}_{mn}\overline{S}_{mn}\delta_{ij}) + C_2(\overline{S}_{ik}\overline{R}_{kj} - \overline{R}_{ik}\overline{S}_{kj})]\}\end{aligned} \tag{3.30}$$

In these equations, $\overline{R}_{ij}$ is a resolved rotation rate tensor, defined as $\frac{1}{2}(\delta\overline{u_i}/\delta x_j - \delta\overline{u_j}/\delta x_i)$. C are various constants, all dependent on C_b:

$$\begin{aligned}C_s &= [8(1+C_b)/27\pi^2]^{1/2}\\ C_e &= (8\pi/27)^{1/3}C_s^{4/3}\\ C_1 = C_2 &= 960^{1/2}C_b/7(1+C_b)0.5\\ C_b &= 0.35\end{aligned} \tag{3.31}$$

The value for C_b, the backscatter coefficient, was determined by Kosović (1997). If it is set to a value of 0, the two SGS models revert back to the Smagorinsky types.

Comparisons to the other models implemented in WRF (Kosović and Curry, 2000; Chen and Tong, 2006) showed considerable improvements under all stabilities.

The NBA model is only used for the parameterization of SGS momentum fluxes. Unresolved fluxes of heat, moisture or other scalars are calculated by the Smagorinsky type models.

3.4 Application of the Eddy-Covariance method for flux estimation in WRF-LES

Eddy-Covariance (EC)-stations are an established micrometeorological measurement system. It allows for the calculation of fluxes of heat, moisture and trace gases. The main component is a sonic anemometer that measures the wind speed by sending an ultrasonic pulse on a short path between a sender and a receiver. The time it takes for the signal to travel depends on the speed of sound in air, but also on the movement of the air between the sensors. By using three of the sender-receiver pairs, the wind speed in all three Cartesian directions can be derived. The mode of operation allows for a sampling of the wind speed of well over 1 Hz, with typical resolutions being 10 – 20 Hz. Subsequent time averaging allows for robust measurements of wind speed and direction.

As the speed of sound in air is dependent, among others, on temperature, the sonic anemometer can also be used for high frequency temperature measurements, where the measured value is the sonic temperature. The derivation of the actual temperature from the sonic temperature is described in Lanzinger and Langmack (2005).

The high resolution of the measurements means that they can be decomposed into an advective and a turbulent part (see Equation 2.5). By multiplying the deviations of wind and temperature, the turbulent kinematic fluxes can be calculated as presented in Table 2.2. These can be transferred into dynamic fluxes, in the case of the heat flux by multiplying with the density and the specific heat of moist air:

$$\overline{Q_H} = \overline{\rho_{air}}\, C_p\, (\overline{w'T'}) \tag{3.32}$$

and in the case of the moisture flux with the density of dry air and the latent heat of vaporization (L_V):

$$\overline{Q_E} = \overline{\rho_d}\, L_v\, (\overline{w'q'}) \tag{3.33}$$

For the derivation of trace gas fluxes, additional open- or closed-path gas analyzers are used. When calculating these fluxes, the q' or T' is substituted with the turbulent fluctuation of the gas concentration. Comprehensive information about the EC-method can be found in Aubinet, Vesala, and Papale (2012).

3.4.1 Energy balance closure

Flux measurements at EC-stations worldwide show that the total amount of outgoing energy within the measured turbulent fluxes, i.e. the sum of latent and sensible heat fluxes, is in most cases lower than the measured incoming radiation, expressed as the sum of incoming longwave and shortwave radiation minus the ground heat flux (e.g. Lamaud et al., 2001; Turnipseed et al., 2002; Imukova et al., 2016). Foken (2008) gives a closure of 80% as a typical value that can be found word wide. The residuals in all measured compartments is between 5 and 20% and is equal for all parts, meaning that the errors in both latent and sensible heat flux are about the same.

The reason for the unclosed energy balance, lies, according to the literature, not in any shortcomings of the method, but in the fact that not all scales on which fluxes happen, are considered. LES has been an important factor for the determination of the reasons; very important first steps were shown by Kanda et al. (2004): The authors use a very idealized LES domain with a resolution of 50 m and without the consideration of moisture, meaning that only the sensible heat flux is present. They compare the turbulent flux taken from single grid points, with a total flux, defined as a horizontal average of the heat flux at the surface over several grid points. In their simulated period, the boundary layer is mostly driven by buoyancy, causing cell-like structures (or turbulent organized structures, TOS). These cells with patches of downdraft, surrounded by streaks of updrafts, can be considered as a circulation with a lower frequency than usual eddys. When using typical averaging periods of 30 to 60 minutes, these circulations will not be captured by the device, because they take too long to pass the sensor. These findings were confirmed by a follow-up study by Inagaki et al. (2006), where additional mesoscale circulations were invoked by varying the surface heat flux in a sinusoidal pattern.

Further work was done by Steinfeld et al. (2007) who employed a much higher resolution of 10 m. This allowed them to evaluate the LES fluxes in several heights and to show that the TOS play a major role for the imbalance in greater heights while their influence is lower near the ground. They also evaluated different stability regimes: under extreme instability with no horizontal wind speed (a case that does not happen in reality), the virtual flux measurements become meaningless, because the measurement point will always be at the same position of a non-moving cell. The closure improves with increasing wind speeds that lead to the cell moving along the point of measurement. Further increasing wind speeds lead to the formation of roll-like structures and a decrease in the energy balance closure. These findings were confirmed by, e.g., Huang, Lee, and Patton (2008), Eder et al. (2015), and Zhou et al. (2018). Schalkwijk, Jonker, and Siebesma (2016) find in their statistical evaluation of LES fluxes for a whole year a dependence not only on measurement height, but also on the averaging time. The longer the time over which to average, the better the energy balance closure (EBC) becomes. This relationship is known from measurement studys. Mauder and Foken (2006) tested averaging times between 5 minutes and 5 days, with improving closures at longer intervals. However, the authors note that such long averaging times are not meaningful, because the general atmospheric conditions change too much during that time.

One reason for the development of TOS is the inhomogeneity of the surface, hotter or colder surfaces favor up- or downdrafts, respectively. This effect was studied with LES by De Roo and Mauder (2018), who show that the lowest EBC can be found at places where the surface below is most heterogeneous. Therefore, some authors (e.g. Brutsaert, 1998) find it beneficial to only measure above a certain height where the different land-surface characteristics are no longer visible in the flux pattern. This height is called the blending height (Pasquill, 1972; Wieringa, 1976). Its height depends on the height of roughness elements and general heights are reported to be on the order of 40 to 60 m above ground.

3.4.2 Derivation of fluxes from WRF-LES data

The easiest way to calculate the fluxes in the LES is to use the *tslist*-module that writes selected variables for a certain grid point into text files in model time resolution (further information in Section 4.1). These files have the required high temporal resolution. To reach the covariances shown in Table 2.2, only the vertical wind speed (w), the water vapor (q_v) and the potential temperature (Θ) is required. To transfer those into dynamic form (Section 2.4.2), some additional variables are required: Pressure p, temperature T and geopotential Φ. All three are saved as a "base-state" and "perturbation" compartment.

For simplicity, the equations for the dynamic fluxes are reprinted here to show the required steps and quantities from the WRF output (where T' is substituted by the deviations of the potential temperature, Θ'):

$$\overline{Q_H} = \overline{\rho_{air}} C_p (\overline{w'\Theta'}) \tag{3.34}$$

$$\overline{Q_E} = \overline{\rho_d} L_v (\overline{w'q'}) \tag{3.35}$$

The density of dry air, ρ_d, can be calculated by using the specific gas constant for dry air, R, pressure p and temperature T:

$$\rho_d = \frac{p}{R\,T} \tag{3.36}$$

To reach the temperature from WRF's potential temperature:

$$T = \frac{\Theta}{(100000Pa/p)^{0.286}} \tag{3.37}$$

The density of moist air is the density of dry air plus the specific moisture, q_v. Keep in mind that q_v in WRF is given with the units [kg kg^{-1}], but here it is required as [kg m^{-3}]. To convert, one first needs the partial pressure of the water in the air, p_{qv}:

$$p_{qv} = \frac{q_v * \frac{p}{100}}{0.622} \tag{3.38}$$

The pressure is here divided by 100 because the equation needs the pressure in hPa while the output of WRF is in Pa. The moisture in the correct units can then be calculated by:

$$q_v[kg\;m^{-3}] = \frac{0.21667 * p_{qv}}{T} \tag{3.39}$$

Finally, the density of moist air is then:

$$\rho_{air} = \rho_d + q_v[kg\;m^{-3}] \tag{3.40}$$

The specific heat capacity of moist air, C_p, depends on the heat capacities of dry air and water vapor, and on the amount of vapor in the air:

$$C_p = \frac{(C_{p,d}\,\rho_d) + (C_{p,vap}\,q_v)}{\rho_{air}} \tag{3.41}$$

This equation yields the heat capacity in [J kg^{-1} K^{-1}], therefore C_p, d and C_p, vap have to be multiplied by 1000 before.
The latent heat of water has to be approximated by the use of the temperature from an empirical relationship:

$$L_v = 2500.8 - (2.36 \cdot T) + (0.0016 \cdot T^2) - (0.00006 \cdot T^3) \tag{3.42}$$

This concludes the derivation of all quantities that are necessary for the calculation of the resolved fluxes with the EC-method. As described in Section 3.1.7, one important part in LES is the subgrid-scale paramterization. It expresses the influence of unresolved eddys, which obviously play a part in the fluxes as well. To derive them, Equation 3.13, repeated here, is a good starting point:

$$\overline{u_j'\phi'} = -K\frac{\delta\overline{\phi}}{\delta x_j} \tag{3.43}$$

The covariance of the fluctuating part, or the kinematic flux, is here described by the means of the eddy coefficient and a height gradient. Rewritten for the covariances for the sensible and latent heat flux, the equation becomes:

$$\overline{w'\Theta'}_{sgs} = -K_h\frac{\delta\overline{\Theta}}{\delta z} \tag{3.44}$$

$$\overline{w'q'}_{sgs} = -K_h\frac{\delta\overline{q}}{\delta z} \tag{3.45}$$

The eddy coefficient K_h is available as output of WRF after some changes to the source code described in Chapter 4.1 and is valid for both the kinematic moisture and heat flux. The height gradient δz is the difference in height above ground between two WRF model levels and is calculated by dividing the sum of base state and perturbation geopotential by the gravitational constant. Geopotential values have to be present in staggered (vertical direction) form. Accordingly, $\delta\Theta$ is the temperature gradient with height; the values have to be staggered here before, as WRF calculates the temperature at mass levels. δq uses the same approach. The resulting kinematic fluxes can be put in 3.34 and 3.35 to convert to the dynamic form. The total flux for a grid cell is then the sum of resolved and SGS flux.

The importance of the inclusion of SGS fluxes becomes apparent in Figure 3.3, where height profiles of the latent and sensible heat flux are shown for a 30 minute period during the experiment described in Section 4.7. It is shown that the SGS fluxes are even larger than the resolved ones near the ground, with their magnitude decreasing with height. Resolved fluxes are small near the ground and increase with height. This behavior is due to the size of eddys: small eddys predominate near the surface, and those are parameterized. In greater heights, eddys can become larger and are therefore resolved by the LES. SGS fluxes drop to 0 in a height of about 100 m above ground; the exact height depends on stability and the size of eddys. Due to their parameterized nature, SGS fluxes are sometimes excluded from evaluations of LES (Steinfeld et al., 2007; De Roo and Mauder, 2018) and only heights above a point where the fraction of the SGS flux drops below a certain percentage of the total flux are taken into consideration.

To compare the fluxes from the EC-method, a reference is required. In measurements, the fluxes are usually compared to the available energy. In idealized LES, this is not possible, as there is no radiation modeled. Different approaches have been invented: Kanda et al. (2004) and Inagaki et al. (2006) use the spatial and temporal average as the true flux and compare it with data from a single grid point. Eder et al. (2015) and De Roo and Mauder

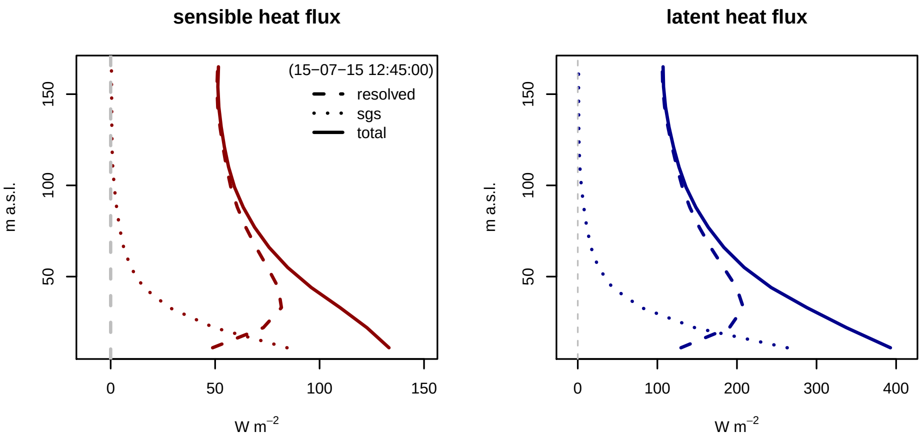

FIGURE 3.3: Height profiles for resolved and SGS fluxes. Data is averaged over 30 horizontal grid points and 30 minutes.

(2018) use the control volume approach by Finnigan et al. (2003), where the true flux is constructed for a control volume with fluxes at all sides of the volume considered. In this work, a different method is suggested: Incoming radiation is modeled and is taken by the *Noah* LSM (the used land-surface model, see also Section 4.6) as an input for the calculation of the fluxes in the ground. *Noah* separates the incoming energy into ground heat flux, and the outgoing sensible and latent heat flux at the surface. Because of the energy conserving formulation of the *Noah* LSM, the energy balance between incoming and outgoing energy is perfectly closed at the surface. The outgoing latent and sensible heat flux can therefore be considered as the true value and can be compared to grid point data. Temporal and spatial averaging can be applied additionally.

Chapter 4

Setup of the WRF-LES and evaluation data

This chapter describes the steps that are necessary to run the WRF model in LES mode on a computing cluster. It contains the changes in the model code that are needed or useful for LES applications and describes how additional input, in this case a high resolution digital elevation model (DEM), can be included.

The chapter further describes the area for which simulations are run, the model settings available and required to run WRF in LES mode and strategies on how to overcome errors during model runtime. The chapter ends with the description of the settings used for this work.

4.1 Changes to the source code and compilation

WRF is downloaded as source code and has to be compiled by the user on the preferred computing environment. In this document, version 3.7.1 of the model code, released in August 2015, was used. Before compilation, some LES specific modifications to the source code are necessary.

4.1.1 Changes to the source code

Generally, there are no substantial changes to the source code required in order to run WRF in LES mode. Yet, due to the high spatial and temporal resolution of LES, it is useful to modify the *tslist*-module in order to limit the high resolution output to certain areas of interest instead of writing data for the whole domain. The *tslist*-module defines certain locations of interest by their geographical location, then searches for the nearest grid point to that location and writes a simple text file with the variable in model time resolution. One file either contains a single three-dimensional variable with rows as time steps and columns as vertical levels or several diagnostic surface variables.

For the LES evaluation, some variables were added to the module, such that for these one additional file is written that contains the variable in all heights. These added variables are staggered and unstaggered vertical wind, unstaggered horizontal wind components, the subgrid stress tensor elements from the NBA model, the pressure in Pa and the horizontal and vertical eddy coefficients for heat and momentum. These additions have to be made in the file `share/wrf_timeseries.F`.

Originally, the *tslist*-module reads the coordinates for the selected locations from a formatted file, `run/tslist`. In this file, the latitudinal and longitudinal coordinates are defined as a float-variable with 7 and 8 digits, respectively, three of them being decimals. This is sufficient in mesoscale models, where every grid points covers several km^2. In LES, the coordinates of adjacent grid points vary on the fifth decimal. To unambiguously specify grid points, the format of the *tslist* file to read is changed to
`FMT='(A25,1X,A5,1X,F8.5,1X,F8.5)'`
in the file `share/wrf_tsin.F`. With this, locations for time series are specified with 5 decimals.

4.1.2 Changes to the registry

The registry in WRF is a list of all variables that are used in WRF. They are specified with their name, their spatial dimensions, including staggering if applicable, a description and the units. Additionally, the registry files define if a variable is just kept during runtime or if it is also written to a restart or history file. For LES applications, it is beneficial to put some additional variables in the history files. These are, in the file `Registry.EM_COMMON` the variables `xkmh, xkmv`, the horizontal and vertical eddy coefficients for momentum, `xkhh, xkhv`, the horizontal and vertical eddy coefficients for heat and other scalars and the turbulent kinetic energy `tke`. Additionally, in the file `registry.les`, the quantities of the subgrid stress tensor $\overline{u_i u_j}$ (described as `m11, m12`, etc.) and the rotation tensor R_{ij} are added to the history files. The history files are NetCDF-files that are written at specified time steps and contain a three-dimensional image of all selected variables at the time.

For the changes of the *tslist*-module to take effect, the added variables have to be declared in the registry: The new profiles as state variables and their names as state variables that belong to the `tseries` package.

4.1.3 Compilation

After modifying the registry and the source code, WRF can be compiled. In this case, this was done using Intel-compilers for Fortran90 and C. Parallel computing using shared memory is provided by the MVAPICH libraries. For input and output, the NetCDF file format in version 4, based on HDF5 is used. PnetCDF allows for parallel reading and writing of NetCDF. Before WRF is compiled, the pre-processing system WPS has to be installed. Due to its lower resource requirements, WPS can be installed for the use of only one processor.

4.2 Required input data

LES for realistic conditions require input data that represent those conditions. Essential are realistic initial conditions that map the properties of the earth's surface and meteorological boundary conditions that govern the large scale circulation in the area. The former has to be available in a resolution that is not much coarser than the horizontal resolution of the model.

WRF offers a set of global input data in different resolutions. Available are albedo, green fraction, leaf area index, land use and land cover, soil parameters (type and temperature), topography and sea surface temperatures, in resolutions between 2° and 30″.

For the model runs presented in this work, some of the standard data sets were used: Land use is taken from a Corine classification with 28 classes and a 3″ resolution (CLC, 2000), soil temperatures are from a 1° data set, soil types are present in 30′ resolution and monthly leaf area indices are taken from a MODIS product with the same resolution. Elevation or topography data is only available with 30″ resolution, which corresponds to an edge length of $\approx$900 m per pixel at the equator. This is insufficient for LES applications where the horizontal resolutions are on the order of meters. Hence, digital elevation data from ASTER (NASA/METI/AIST/Japan Spacesystems and U.S./Japan ASTER Science Team, 2009) with 1″ resolution (30 m at the equator) was prepared for the use in WRF. The original downloaded 1° tiles were combined to one big tile to reduce possible errors due to overlap. The resulting tile was exported in the *band interleaved by line file format* (.bil) and renamed according to the standards used in WRF. The additional required index file can be found in Appendix A. With this data set, the orography of the model domain can be represented in great detail and allows for the investigation of the effects of slopes on the LES solutions.

As meteorological boundary conditions, reanalysis data from the ERA-interim project (ECMWF, 2009, updated monthly) was used. This dataset is available in T255 horizontal resolution (about 0.7°) with a new dataset every six hours. Meteorological variables come in 37 vertical levels and soil information in four layers.

4.3 LES-specific model settings

To run WRF in LES mode, a few settings have to be chosen in the namelist files that are used to control the simulations. In `namelist.wps`, the file that controls the pre-processing system WPS, the resolution of the model has to be given as `dx` and `dy`: It should be below 100 m in order to show LES characteristics. `geog_data_res` then needs entries for the relative paths to the input data with a sufficiently high resolutions. With these settings, input files for WRF can be created.

In `namelist.input`, the file that controls the simulation, the following settings are necessary: In the `&domains` block, the resolution specified in the WPS namelist has to be adopted. This then specifies the time step of the model: it should be on the order of six times the horizontal resolution in kilometers (Skamarock et al., 2008), meaning that a typical LES time step is always below one second. This file also controls the vertical resolution of the model. Limits are set by `e_vert`, the total amount of staggered vertical levels, and `p_top_requested`, the top of the model, specified in Pa. With these settings alone, WRF will produce a distribution of sigma-levels, but it can be useful to specify the levels by hand using the entry `eta_levels`. This way it is possible to have a high resolution within the PBL and to comply with specific ratios between horizontal and vertical resolution that are required by SGS models (e.g. Mirocha, Lundquist, and Kosović, 2010).

In the `&physics` section, the entry `bl_pbl_physics` has to be set to 0, effectively turning off any boundary layer parameterization schemes.
`cu_physics` also has to be turned off, because all available cloud parameterization schemes are constructed for lower resolutions. If clouds and precipitation are of interest, a microphysics scheme has to be chosen with the entry `mp_physics`. Setting `isfflx` to 1 will allow the model to use heat and moisture fluxes and u_* as calculated by the model instead of using specified values. This effects the surface layer parameterization, which is chosen in `sf_surface_physics`: a value of 1 will select the MO scheme by Jiménez et al. (2012), 2 will use MO with modifications by Janjić (1996). Both settings can be chosen.

The `&dynamics` section of the namelist further specifies the mode of operation of the LES. `km_opt` chooses the SGS model, where a value of 2 uses the 1.5 order TKE closure and 3 the first order Smagorinsky type closure (see Section 3.1.7). `diff_opt` determines if the mixing is evaluated only on vertical coordinate surfaces (value 1) or in three-dimensional space (value 2). `mix_full_fields=.true.` will allow the SGS model to work on the absolute simulated values, instead of using only deviations after subtracting a 1D-profile. Setting `sfs_opt` to 1 or 2 will tell the model to use the

NBA SGS model (Section 3.3.3) with the Smagorinsky or the TKE based stress terms, respectively. The time stepping and advection schemes can be left at their default settings, using the third-order Runge-Kutta scheme for time integration, a fifth-order scheme for horizontal and a third-order scheme for vertical advection. These settings have been shown to be a good combination (Wicker and Skamarock, 2002) and are recommended for the simulation of realistic conditions (Gibbs and Fedorovich, 2014).

Using these settings, a model setup for a real conditions case will be a LES. Additional settings are possible but not necessary. The setup used for the simulations presented in this document is shown in Section 4.6.

4.4 Description of the area under investigation

The area of investigation lies in southern Germany, 50 km southwest of Munich and 65 km south of Augsburg (Figure 4.1). It is named *Fendt* after a small aggregation of agricultural buildings. The general area is part of the foothill of the alps. It is influenced by the temperate climate of the mid-latitudes and alternating oceanic and continental flows. The whole year is humid, with peak values of precipitation in summer. Mean temperatures range between 18 °C (July) and -0.5 °C (January). Comprehensive descriptions of the climatic and landscape characteristics can be found in Kunstmann et al. (2004) and Kunstmann, Krause, and Mayr (2006).

Fendt is one part of the TERENO infrastructure, a network of terrestrial environmental observatories in Germany (Zacharias et al., 2011; Bogena, 2016). TERENO pre-Alpine consists mainly of the Ammer catchment (Kunstmann et al., 2004). Within this catchment, study sites equipped with a multitude of various instruments are located along a height gradient from south to north, with *Fendt* being the northernmost location, representing the lowlands of the foothills of the alps. The site is permanently equipped, among others, with an Eddy-Covariance station (part of FLUXNET), an array of automatic lysimeters, a sensor network measuring soil moisture and temperature (www.soilnet.de, see also Section 4.8.3), test installations of commercial microwave links for the derivation of precipitation, a ceilometer and cosmic-ray neutron sensors. A summary of recently conducted investigations in TERENO pre-Alpine can be found in Kiese et al. (2018). The *Fendt* site additionally was the location for two large, orchestrated measurement campaigns called ScaleX which were held during summer in the years 2015 and 2016. In addition to the permanent infrastructure, the following instruments were employed: RASS (radio acoustic sounding system), a Doppler Lidar, humidity and temperature profilers, fixed wing UAV's and

FIGURE 4.1: Location of the LES domain in Central Europe (red square)

multicopter drones (Brosy et al., 2017) and gas analyzers. The goals and the infrastructure of the ScaleX campaigns are detailed in Wolf et al. (2017).

The site is very suitable for an investigation using LES due to several reasons: As it its part of the TERENO infrastructure, the data availability spanning atmospheric and soil parameters is very good. Due to its location in the alpine foreland it shows a rather complex topography that is quite different to the mostly ideal areas usually considered in LES, while still being homogeneous enough to avoid many possible instabilities due to extremely steep slopes. The ScaleX campaigns constrain the selection of the periods that are to be simulated. Due to the additional data gathered during the campaigns, the amount of possible validation data is large and since the campaigns took place in summer, it is straightforward to find a time with high solar insolation, few clouds and no precipitation. These are circumstances where turbulent structures during the day are large and more easily resolved by LES. Two periods of 48 hours each in July 2015 and 2016 were finally selected for the simulations.

During summer, *Fendt* is within the reach of mesoscale mountain circulations. During day and strong insolation, the Alps tend to heat up faster due to the slopes than the surrounding, flatter areas. The resulting updrafts over the mountains lead to compensating flows towards the Alps in the surroundings, manifesting as northerly winds during most days in summer in *Fendt*. At night, air over the mountains cools down faster than in the surroundings and flows down the slopes, driven by gravity. This can be measured as southerly wind directions during many nights at *Fendt*. The process is called alpine pumping (Lugauer and Winkler, 2005; Graf et al., 2016) and determines the conditions at *Fendt* during summer when no other large scale atmospheric drivers are present. Kučerová et al. (2017) showed that this autochtonous weather situation is prevalent in the alpine area in summer due to a temporally only short influence of large scale circulation patterns. The same effect is described differently in Beck, Jacobeit, and Jones (2007): in July, the weather in central Europe is, in over 80% of the days, governed by a northwesterly large scale circulation, but this type shows a large internal variability.

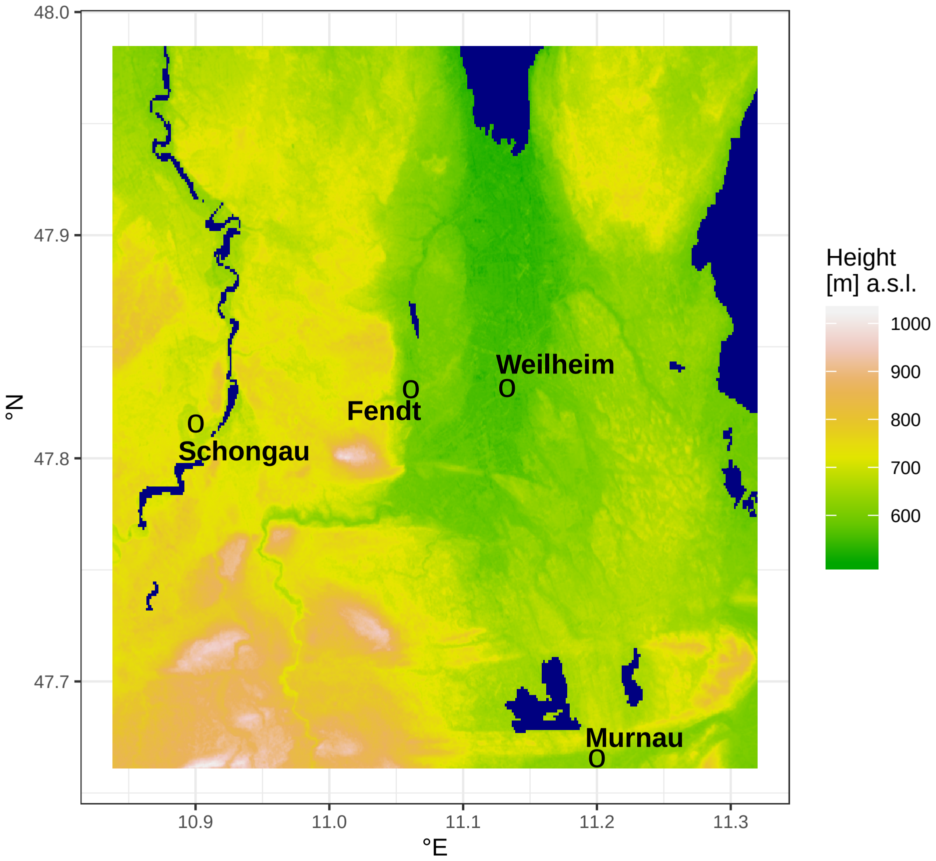

FIGURE 4.2: Orography of the *Fendt* area. Map constructed using the ASTER DEM.

Figure 4.2 shows the orography of the *Fendt* area. It is a result of glaciogenic molding during the last ice age. The lakes at the northern and eastern edges of the maps are remnants of the glaciers. In the southwest lie the northern foothills of the Ammergau Mountains, cut in half by the river Ammer that forms the catchment for the TERENO pre-Alpine region. *Fendt* itself lies on a plain, the Ammer valley, of 600 m height that extents far east. It is bordered by a high terrace in the west that is rising the terrain to 750 m. On its southern edge is the mount Hohenpeissenberg, the location of one of the oldest meteorological observatories in Germany. The ridge is also limited to the west by the river Lech that flows through a very steep valley. The last two features in the vicinity of *Fendt* have implications for the selection of a final simulation domain, as they introduce steep slopes.

4.5 Challenges in the model setup

The general properties of the planned model runs have been outlined in the sections above. The model should cover a certain area around the *Fendt* observatory and represent two 48-hour periods during the ScaleX campaigns of 2015 and 2016. WRF-LES requires the horizontal domain to have at least the size of five times the height of the boundary layer, which reaches up to about 2000 m above ground during summer in mid latitudes (Seidel, Ao, and Li, 2010), resulting in a minimum horizontal size of 10 km. As the model is supposed to represent real conditions, a higher upper limit is desirable to consider possible exchange effects between PBL and free atmosphere.

The second important choice concerns the horizontal resolution. A model is considered a LES when it is below 100 m. At 100 m, only the largest eddys during highly turbulent periods will be resolved, while the required computing power will be low. At much higher resolution (1 m), almost all relevant turbulent motions would be resolved, but the required computing resources are significantly higher.

Tests were done using $\Delta x = \Delta y =$ 50 m, 60 m, showing that this resolution is too coarse, especially for the nocturnal periods where turbulence is strongly dampened by stable layering. As a compromise between the required computing power and smallest resolved scales, the final horizontal resolution was set to $\Delta x = \Delta y =$ 30 m. This determines the vertical resolution, as the ratio $\Delta x/\Delta z$ needs to be between 2 and 4 (Mirocha, Lundquist, and Kosović, 2010) in order for the NBA-SGS model to function properly. The selected resolution in the vertical is at $\approx$11 m, where the uncertainty is given by the definition of sigma levels through pressure (c.f. Equation 3.19).

WRF offers the possibility of nesting, which allows for a run-time downscaling of large scale circulation down to the LES scale. Examples for this approach are given in Muñoz-Esparza et al. (2017) and Rai et al. (2017). It was tested for the *Fendt* domain as well, but was dismissed due to two reasons: The first challenge is posed by the surrounding terrain: The Alps are within a few dozen kilometers south of *Fendt* and would have to be represented in the outer domains. The used WRF version 3.7.1 has implemented the feature of vertical nesting (Daniels et al., 2016), yet does not document it. Limitations in the parameterizations that can be used while nesting vertically prevent its use in this case. It follows that a grid box in an outer domain of a nested model would show horizontal extents of kilometers, while being only 11 m high. Having such boxes over the complex topography of the alps results in numerical instabilities that make the setup of such a model impossible. The second reason is the required computing power: nesting increases the number of grid points substantially and therefore the amount of required calculations and storage.

The decision of abstaining from nesting implies an implicit research question of this thesis: No nesting means that the domain will be directly driven by reanalysis data as the meteorological input. Can such a model (1) create turbulent structures in a way that is shown in other LES and (2) will the domain exhibit the meteorological small scale features that are caused by the local circumstances and measured by the TERENO and ScaleX infrastructure?

The process of finding a suitable domain within the framework outlined above has to be described as a process of trial and error. Most problems do not arise while defining the model properties, but only during runtime; a new configuration has to be tested by running the simulation. The time required to find a working setup is therefore high.

4.5.1 Challenges caused by orography

The area around *Fendt* is within complex terrain, including steep slopes. These, in combination with the terrain following coordinates in WRF, can cause numerical instabilities, namely violations of the Courant-Friedrichs-Lewy (CFL) condition (Courant, Friedrichs, and Lewy, 1967). This condition relates the resolution of a grid point with the wind speed in it and the time step of calculation. It indicates that an air parcel can not move farther than the size of a grid box within one time step. If it does, the model will stop. In the presented case, this occurs mostly in the vertical direction at slopes, where the vertical extent of a grid box is smaller than the height difference to the adjacent grid box. The range of problematic grid box sizes depending on the slope angle is shown in Lundquist, Chow, and Lundquist (2010b). The authors show that with the given aspect ratio of 3 in this model, maximum slope angles should not exceed 20°.

To address this limitation, two possibilities exist: The first is to set the domain at such a location that steep slopes are excluded. This is not completely possible for the *Fendt* domain (c.f. Figure 4.2): The Lech valley west of the high terrace and the northern foothills of the Ammergau Mountains proved especially problematic but can be excluded; the Hohenpeissenberg can not as it is very close to the area of interest. Here, the second approach has to be applied, which is the smoothing of the elevation model data. The possibility to do this is present in WPS. Its settings can be found in `geogrid/GEGRID.TBL.ARW`. Here, in the section for the height model (`HGT_M`), a smoothing option can be specified, as well as the amount of iterations of the algorithm. Finding the correct amount of iterations that smooth the input data sufficiently while not changing the data too much is again part of trial and error. For the simulations presented here, the following settings produced satisfactory results:

```
smooth_option = 1-2-1; smooth_passes=24
```

The effects of the smoothing are shown in Figure 4.3. It shows the slope angles of adjacent grid points over 15 km in east-west direction at 47.795° latitude (cut through the southern part of the Hohenpeissenberg). All slopes are less steep after the smoothing process, meaning loss of information, but the benefit can be seen at those locations where angles exceeded 20°: These are now within the range given by Lundquist, Chow, and Lundquist (2010b). This treatment of the DEM data at preprocessing level removed a substantial reason for numerical instabilities.

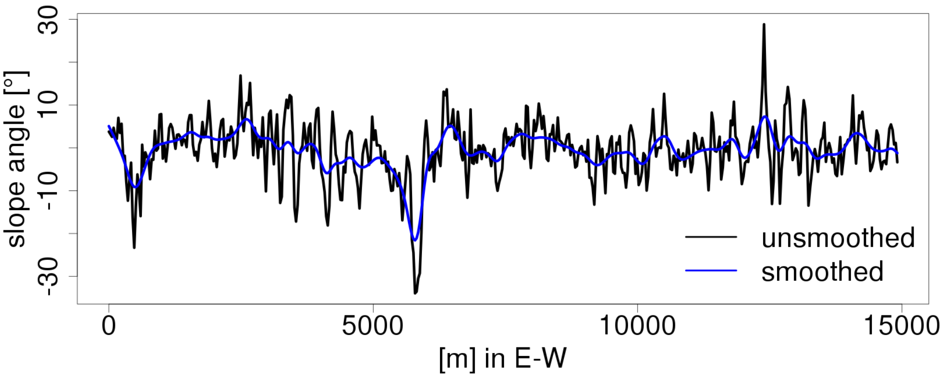

FIGURE 4.3: Comparison of smoothed and unsmoothed DEM data.

4.5.2 Selection of time spans

The following criteria were considered during the selection of the two 48 hour periods: No rain observed during the time; few clouds to have high solar insolation, high soil temperatures and therefore strong convection;

no significant weather changes during the time, indicating for example the passage of frontal systems; wind speeds in the boundary layer below 10 m s^{-1}.

These criteria were selected so that the periods represent times where turbulence can develop freely within the domain without being influenced too strongly by external factors. The relatively low wind speeds are a requirement of the modeling approach using only one nest: As no information about turbulence or vertical wind speeds is included in the meteorological boundary conditions, vertical motions have to develop within the model domain. This takes space proportional to the wind speed. Higher speeds result in larger areas at the inflow side of the model where turbulence is not developed, while lower speeds result in smaller such areas. This has also be considered when setting the total horizontal size of the domain.

An additional requirement for the selected period was the presence of high quality measurement data from the ScaleX infrastructure.

The times were selected using data from the Eddy-Covariance tower and the wind Lidar.

4.5.3 Time stepping

The time step of the model is given in the WRF documentation as being on the order of six times the horizontal resolution in km (Skamarock et al., 2008), resulting in a recommended time step of 0.18 s. At such temporal resolution, it is useful to test a range in order to find the maximum possible time step, as this can decrease the required computing time substantially.

Additionally, WRF offers a module for an adaptive time step (Hutchinson, 2007), where the CFL condition is evaluated at runtime and the time step adapted, if necessary. It can be limited by a minimum and maximum time step and the maximum change is given by a user defined value.

The usage of the adaptive time step proved useful for the WRF-LES: Initialization time steps, or the first few steps, required a much smaller δt than the rest of the simulation. Using the adaptive time step, this can be solved by setting the minimum to what is needed during the model start and the maximum to the maximum possible time step the model will run on without instabilities.

Problems occurred at times when meteorological boundary conditions are updated. These time steps are pre-determined by the reanalysis data as those times for which data exists. During some runs of the model, the adaptive time step of well below a second lead to the fact that the exact time for the new boundary conditions was skipped by the fraction of a second. The code then can not find the required input and the simulation stops. This was amended by regularly writing restart files and then restarting short before the crash time. In most cases, the required time step was then met and the boundary conditions read.

4.6 Final setup for the general model

The final selected model domain covers 15 by 15 km around *Fendt* with a horizontal resolution of 30 m, resulting in 500 by 500 grid points. The TERENO infrastructure is not centered but shifted by about 50 grid points to the west and 30 to the north in order to not include the orographically difficult Lech valley to the west and the foothills of the Ammergau Mountains in the south. To achieve this, the domain was centered on 47.823° north and 11.079° east. The projection was also centered on this latitude. The DEM for the area is smoothed to avoid steep slopes. The final height model can be found in Figure 4.4. The difference in details to the unsmoothed elevation model shown in Figure 4.2 is distinct. The height covers a range from 530 m in the north east to 960 m above sea level on the summit of mount Hohenpeissenberg. The only water surface is the Zellsee straight north of *Fendt*, river and stream surfaces are present in reality but too small to be represented by a 30 m resolution.

Further information about the domain can be derived from the land use map shown in Figure 4.5. The area is dominated by pastures that cover most flat and drained surfaces. The second most abundant class is evergreen needle leaf forests, consisting mostly of agriculturally used spruce plantations. Areas not or less agriculturally used (low areas near drainage channels and the flank of the high terrace) are covered in mixed forests and wetlands.

The vertical dimension of the domain reaches up to 500 hPa, which corresponds to roughly 5500 m above sea level and therefore easily encompasses the PBL. It is split into 150 vertical levels with variable heights. Within the PBL up to a height of about 2000 m above sea level the resolution is at $\approx$11 m. Above, the vertical levels are stretched up to 150 m in the topmost. The distribution of height levels is shown in Figure 4.6. With this approach a high number of levels can be achieved within the PBL where the ratio between Δx and Δz is important, while keeping the total amount of levels sufficiently low.

The data sets used for the generation of initial and boundary conditions are described in Section 4.2. Meteorological boundary conditions are updated every six hours.

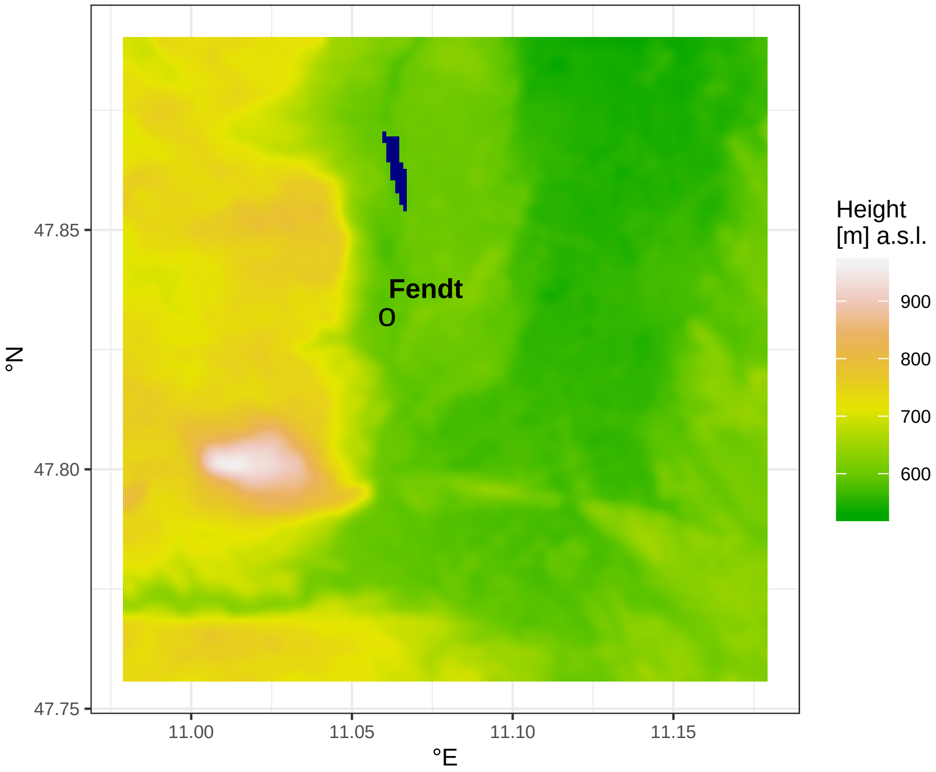

FIGURE 4.4: Area of the final model domain, with smoothing applied.

The physics parameterizations of the model runs used the WSM 5-class microphysics scheme (Hong, Dudhia, and Chen, 2004) for the treatment of moisture. Radiation processes in the shortwave and longwave range were computed by the rapid radiative transfer model (RRTMG) scheme (Iacono et al., 2008), which was updated every four model time steps. It models the radiation through the whole atmosphere, adding levels when the WRF domain does not reach up to 50 hPa. The *Noah* LSM was used as the soil model and the MO-similarity with the modifications by Janjić (1996). No parameterizations for clouds, boundary layer physics or urban areas were used.

In the dynamics section of the namelist, the following settings were used: The eddy coefficients were calculated by the 1.5 order TKE closure (see Section 3.1.7), evaluated in physical space. 6th order diffusion was allowed down-gradient. At the top 500 m of the model, a Rayleigh damping layer was introduced to prevent the reflection of secondary waves. The model was run in non-hydrostatic mode. The NBA-SGS model was chosen for the calculation of the eddy coefficients for momentum.

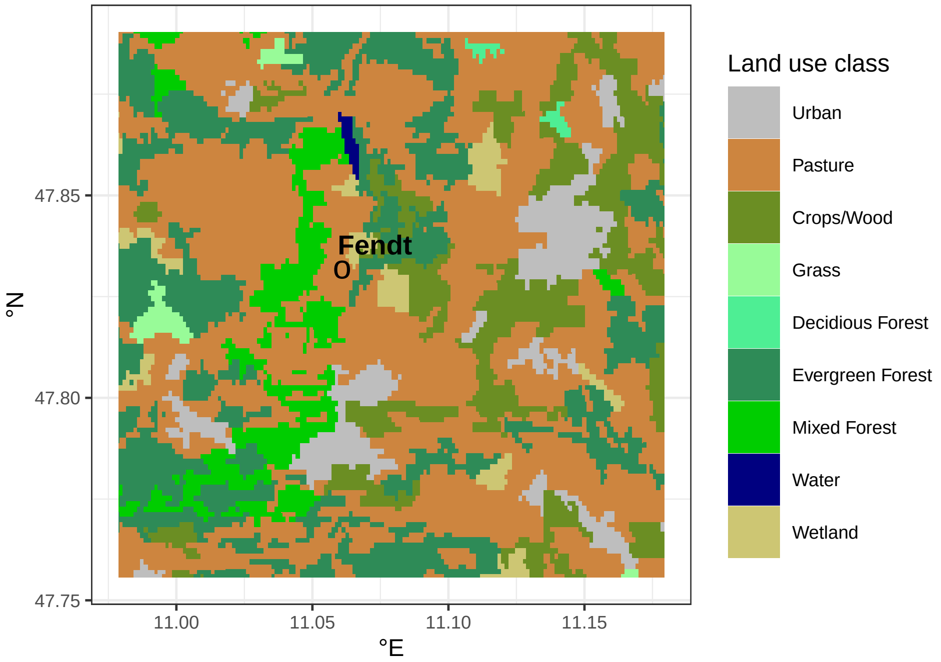

FIGURE 4.5: Land use in the final model domain.

At the domain edges, 15 rows of grid points were assigned for specified boundary value nudging, with one specified row and 14 rows for relaxation. This prevented instabilities during the reading of new boundary conditions, as it lowers the gradients between boundary conditions and values within the model domain.

The following two periods were selected for the simulations: 15-17 July 2015 and 6-8 July 2016. Both were times of high solar radiation, few clouds and no rain. During both times, data from a multitude of the ScaleX instrumentation is available. The time span of 48 hours per model covers two sunrises and two sunsets and therefore stable nocturnal as well as daytime turbulent boundary layers. Both models were initialized at 00:00 UTC (02:00 local time). Geostrophic wind speeds differ between the two periods, with those in the 2016 model being slightly higher (up to 5 m s^{-1} in the boundary layer). As the wind speed is one factor of the CFL condition, the 2016 model had to run on a smaller time step than the 2015 model to guarantee stability. Accordingly, the 2015 model was run with a maximum time step of 0.25 s, the 2016 model with 0.2 s. Both models had a minimum time step of 0.0625 s that was only used during the model initialization.

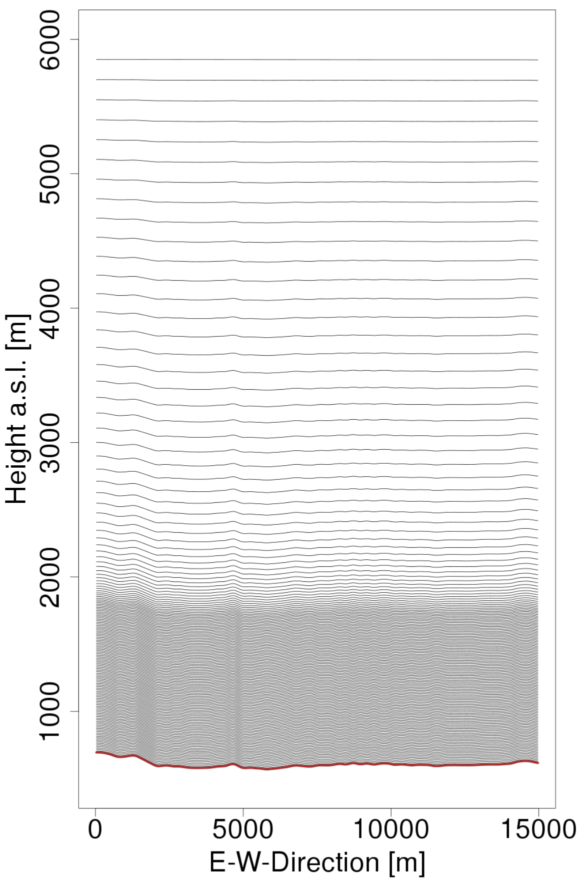

FIGURE 4.6: Distribution of vertical levels in the WRF-LES domain. The red line marks the surface.

As the model needs time to go from a stationary initialization state to a resolved flow field, 6 hours after initialization were considered spin up time and only data after that time was evaluated. The spin up is accelerated by the sunrise that induces turbulence.

For a comprehensive overview of the settings used to drive these models, the namelist files for WPS and WRF are given in the Appendix (B and C).

4.7 Final setup for the *soilnet* model

An additional model run was conducted for the same domain with the intent of quantifying fluxes of heat and moisture. These fluxes are a standard output of the used *Noah* land surface model, but the high temporal and spatial resolution of the LES method also allows for a quantification in any desired height by using the Eddy-Covariance method (e.g. Aubinet, Vesala, and Papale, 2012) also described in Section 3.4. The additional run was

24 hours long and covers 15 July 2015 0000-2400. It uses the setup described above with a substantial change:

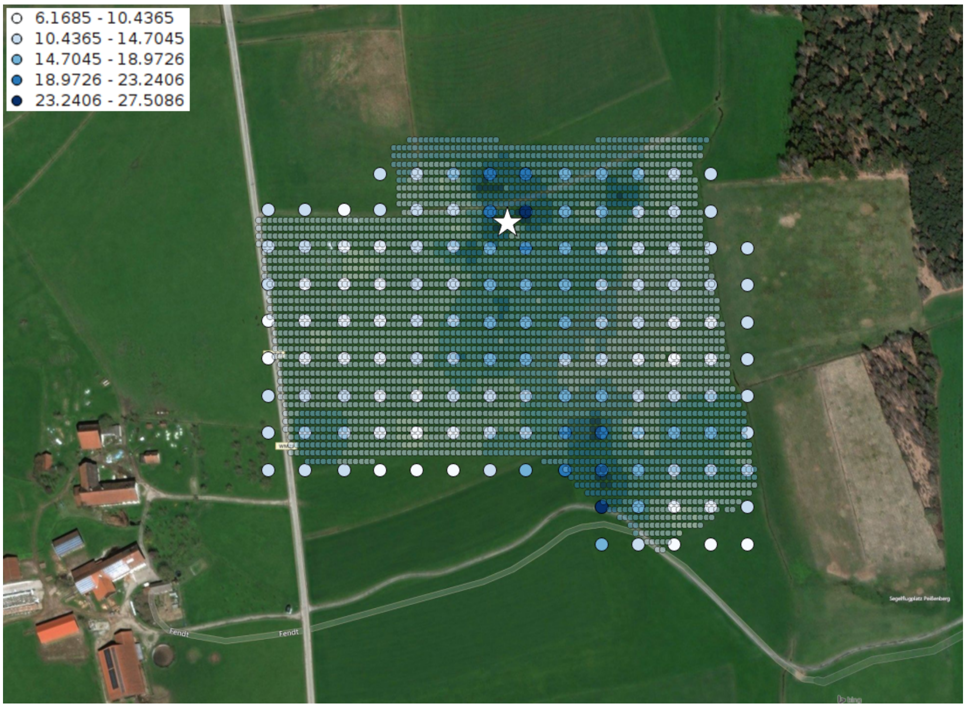

FIGURE 4.7: Soil moisture [%] at *Fendt* at 0000 UTC 15 July 2015. The points in the background show the *soilnet* data, the large points show the interpolated values on the WRF grid. The white star is the EC-station.

The initial conditions for soil temperature and soil moisture were changed to represent the conditions measured with the *soilnet* sensor network (see Section 4.8.3). The data measured at 0000 UTC 15 July 2015 in the topmost level was taken and transferred on the WRF grid. The *soilnet* data is available in a interpolated grid with a resolution of $\approx$0.00005° ($\approx$ 5 m) and has therefore to be interpolated onto the WRF grid. The following approach was chosen: For the coordinates of one WRF grid point, all *soilnet* measurements within 45 m ($=1.5\Delta x$) of the WRF grid center are taken and averaged. Alternative approaches would have been interpolation via inverse distance weighting or kriging. The described simple approach was chosen because it gives a distribution that closely resembles the pattern found in the measurements and also dampens extreme values that might lead to large gradients and subsequently model instabilities.

Figures 4.7 and 4.8 show the measured soil moisture and temperature, respectively, as well as the values interpolated onto the WRF grid. The white star marks the EC-station (see Section 4.8.2) that provides the measurements for model evaluation. These interpolated points can easily be used as substitution for the according points in the wrfinput file that contains the

FIGURE 4.8: Soil temperature [°C] at *Fendt* at 0000 UTC 15 July 2015. The points in the background show the *soilnet* data, the large points show the interpolated values on the WRF grid. The white star is the EC-station.

initial conditions for the model runs. It is clear that the area of the *soilnet* is smaller than the total model domain by orders of magnitude. Yet, also soil properties from the area around the *soilnet* influence the conditions at the *Fendt* measurement site. Therefore, the conditions of the *soilnet* have to be transferred to the rest of the domain, as they are considered to be a better representation of the soil properties than that given in the standard WRF input. To extrapolate the measured moisture to the whole domain, a random distribution of values was created, using the mean of the measurements and half of its standard deviation (using 1 standard deviation led to negative soil moisture values). At every grid point not covered by the *soilnet*, a random sample from this distribution is drawn and set as the value. Additionally to adapting the whole area to the measurements, this also creates small scale gradients in moisture. It is known that differences in soil properties and random perturbations in the atmosphere are both encouraging the development of turbulence in a LES (Mirocha, Kosović, and Kirkil, 2014). This is expected to behave comparably.

WRF uses (when using the *Noah* LSM as land surface model) soil information in four layers. To determine the moisture for the lower layers, the difference between the layers found in the standard data set was applied to the new data to create a natural gradient in the soil. This is done for consistency only, as it is not to be expected that the soil properties of any but the topmost layer change within the 24 hours of the model run. This was confirmed by the evaluation of the earlier conducted model runs described above.

The approach for changing the soil temperature is similar, but additional respect has to be paid to the dependency on height: Soil temperatures in lower heights are higher than above. All grid points covered by the *soilnet* again use averaged measurements from the surrounding 45 m. All other grid points are then in a first step corrected by the mean difference between the *soilnet* data and the original data found in this location. Additionally, a random deviation constructed from the range of the *soilnet* measurements is added. The random sample is using the mean and half of the standard deviation of the measurements. This approach retains the height gradients and adds random perturbations, also enhancing the development of turbulence. The lower levels are treated the same way as was done for the moisture.

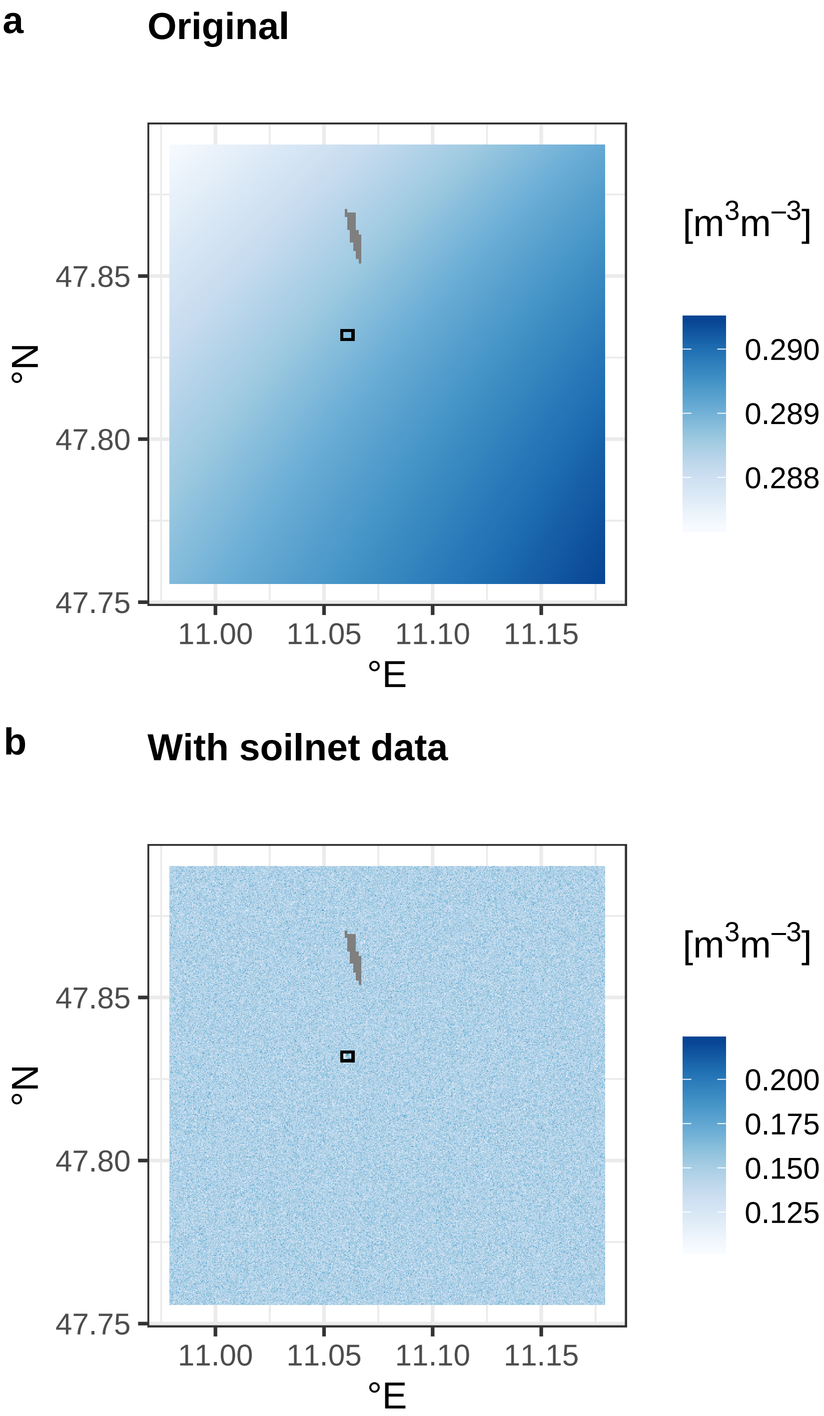

FIGURE 4.9: Original (a) and adapted (b) soil moisture for the LES domain. The area of the *soilnet* is surrounded by the black box. The lake Zellsee is grey.

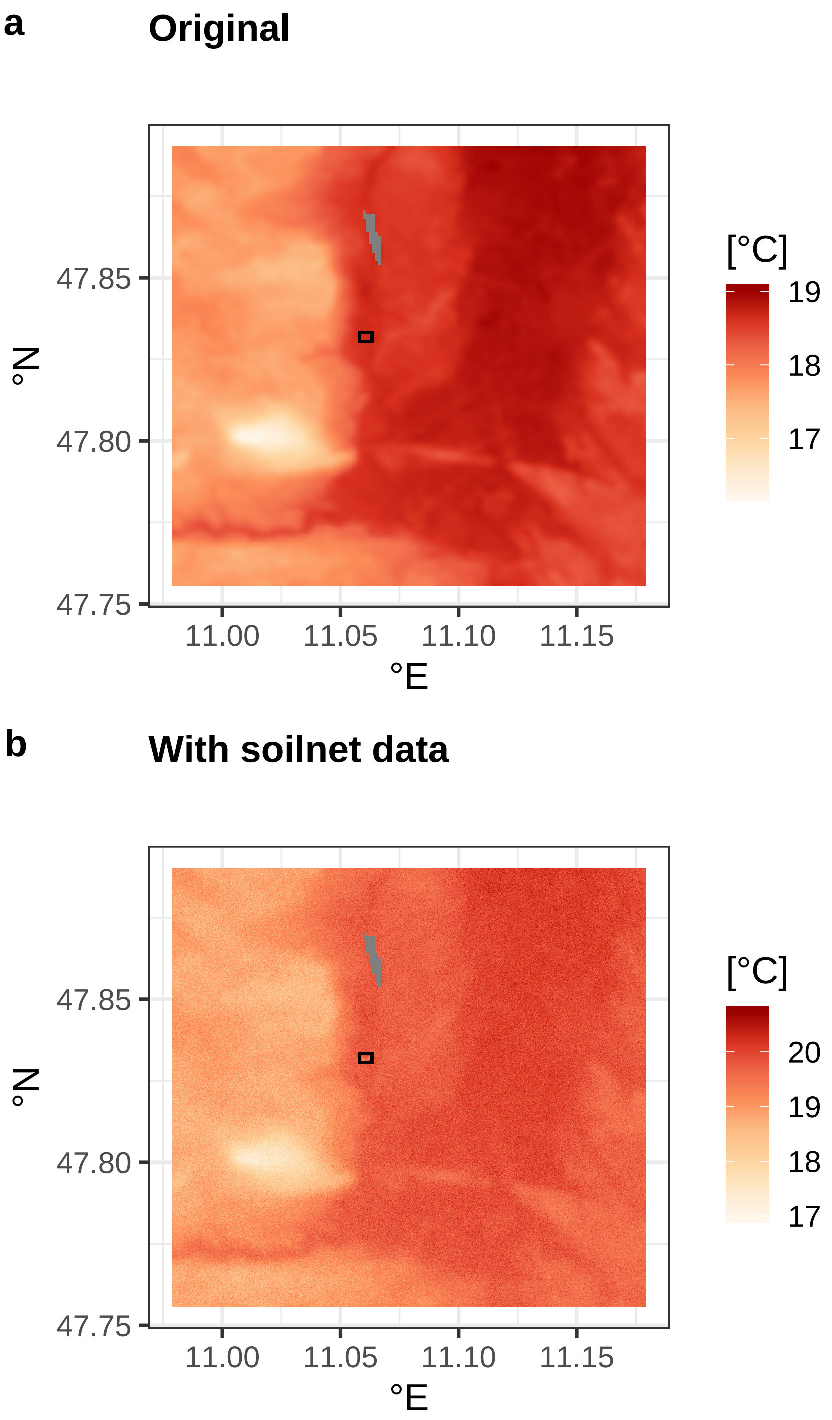

FIGURE 4.10: Original (a) and adapted (b) soil temperature for the LES domain. The area of the *soilnet* is surrounded by the black box. The lake Zellsee is grey.

FIGURE 4.11: Locations of the grid points used for data generation (shown in blue). The white star marks the location of the EC-station.

Figure 4.9 shows the differences between the soil moisture of the top soil level in the original data and the changed data. The original data shows almost no variability between grid points and the whole area has the same moisture of $\approx 0.29\ \mathrm{m^3m^{-3}}$. In the adapted domain, the moisture is, on average, only half as high and it varies by a larger margin.

Obviously, the generated moisture data in grid points surrounding the *soilnet* area does not represent a natural moisture field. Evaluation of the resulting data is only done over grid points with measured data. The motivation to include the randomized field around is twofold: To incite an enhanced development of turbulence and to make sure that possible advected flux parts do not deviate too strongly from the measured conditions.

The soil temperature, shown in Figure 4.10, is on average 2 K warmer than in the original data. The height gradients are retained, while the variability is increased. The span between minimum and maximum is comparable between both data sets.

The images show that the period around the 15 July 2015 was comparatively dry and the temperatures were high.

For the evaluation of the fluxes originating from the surface over the *soilnet*, 30 grid points in a 6 by 5 raster were chosen as locations where time series in model resolution were written. This data can be used to calculate turbulent fluxes. Their locations are shown in Figure 4.11.

Additionally to the changes in the initial soil conditions, this model run uses the surface layer formulation by Jiménez et al. (2012) instead of Janjić (1996) (see Section 3.3.2), as this was shown in preliminary experiments to produce realistic flux profiles.

4.8 Description of the data used for model evaluation

This section contains short descriptions of the measurement devices used in this study: the *VirtualTower*, the EC-station and the soilnet-installation. Along with a short explanation of the mode of operation, the preprocessing of the data, if applicable, is discussed. In parts, this closely follows Hald et al. (2019).

4.8.1 *VirtualTower*

Three Doppler Lidars (model StreamLine XP, Halo Photonics Ltd, Worcester, England) were placed approximately 500 m apart in a triangular arrangement. Each Doppler Lidar (DL) retrieves the speed of the air along a beam by measuring the Doppler shift in light as it is backscattered by aerosols. All three Lidars simultaneously performed a scan along a vertical profile, producing a virtual measurement tower. While a single Lidar can only measure speeds towards or away from its location, the combination of three is able to measure all three wind components (u, v, w), where u is the zonal, v the meridional and w the vertical wind component (Newman et al., 2016). The wind vectors follow from rotation of the along-the-beam wind vectors observed nearest to an intersection along the virtual profile (Stawiarski et al., 2013; Vasiljević et al., 2017). The points along the vertical profile were chosen 3 m apart up to 20 m above ground and 18 m apart up to a height of 1000 m above ground. The range above a depth of 1000 m was excluded here because of discontinuous observations further away from the Doppler Lidars, following detection limitations thought to be related to a decrease in particle density away from the surface that leads to decrease in backscattered laser light signal. The measured values of w in the lowest levels were considered unreliable and are therefore excluded from the evaluation.

Aggregations in 10, 20, 30 minutes were computed from one minute DL scans of 1 Hz integration per beam. The Lidar measurement period overlapping with the simulated period was from 0600 UTC 15 July to 0000 UTC 17 July (42 hours) for the 2015 measurement campaign, which included two sunsets and one whole night. The overlapping period for the 2016 campaign spans 32 hours, from 1600 UTC 6 July to 0000 UTC 8 July, covering two sunsets, one sunrise and one whole night and day. To perform a meaningful comparison, the measured wind speeds were linearly interpolated to the heights of the model levels.

Figure 4.12 shows the positioning and mode of operation of the *VirtualTower*.

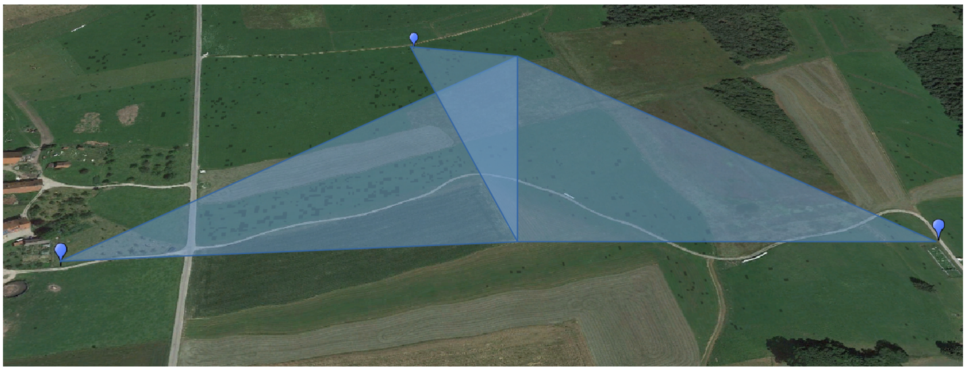

FIGURE 4.12: Structure of the *VirtualTower* installation. Three Lidar beams form a virtual tower at the common center of three intercepting beams.

4.8.2 EC-station

The mode of operation of an EC-station is based on high-frequency measurements of wind speed, other meteorological parameters and trace gases and is described in detail in Section 3.4.

The EC-station located in *Fendt* (see Figure 4.11) measures in a height of 3.5 m with a frequency of 20 Hz. Evaluated results of the measured fluxes are averaged over 30 minutes. Main components are a CSAT3 sonic anemomenter by Campbell Scientific (UT, USA) and an open-path infrared gas analyzer (LI-7500, Li-Cor, NE, USA). Data logging and storage are handeled by a CR3000 data logger (Campbell Scientific, UT, USA). A CNR4 four component net radiometer (Kipp & Zonen) measures the radiation balance at the station. A more detailed description of the used instrumentation can be found in Zeeman et al. (2017). Flux calculation within the device and quality control of the measurements is done by the TK3-software package (Mauder and Foken, 2011). A detailed evaluation of the measurements over longer time periods, the footprint (i.e. the area where the measured fluxes come from) and the climatic conditions at the site is presented in Soltani et al. (2017). The station is located in a valley with N-S-extension, with grass as the dominant soil cover. Forests are within a few hundred meters. The conditions are not ideal for the application of the EC-method, but during northerly and southerly flows, the footprint of the EC-station is nearly homogeneous. Soltani et al. (2017) also treat the problem of the energy balance closure in *Fendt*. Here, the long-term energy balance closure is determined as 0.65, meaning that only 65 % of the measured incoming energy can be measured again as turbulent fluxes. The authors show a clear dependency on the diurnal cycle (with a much better closure during day) and on the seasons, with better values during spring, summer and autumn. Both effects can be attributed to the probability for unstable boundary layer conditions that invoke turbulent motions. The EC-station in Fendt is part of ICOS (Integrated Carbon Observation System, `https://www.icos-cp.eu/`), a European measurement network for determining carbon fluxes and budgets of greenhouse gases.

Due to the use of the TK3-software, the resulting data sets already contain flux and radiation aggregations over 30 minutes and can directly be compared to the LES fluxes.

4.8.3 Soilnet

The *soilnet* is used to gather information about soil moisture content and soil temperature that is used in this work as driver for the LES experiments on the latent and sensible heat flux. The *soilnet* at the *Fendt* site consists of 55 sensors: 20 are regularly placed on a grid on a 70 by 70 m area and the other 35 are randomly scattered over a 300 by 300 m surface. The sensors measure moisture and temperature in three depths (5, 20, 50 cm) and with a 15 minute time resolution and transmit the data wirelessly to a storage system. At every location in the mesh and at every depth, three sensors are installed: one dielectric soil water potential sensor (MPS-6, Decagon Devices) and two electromagnetic soil water content sensors (SMT100, Truebner GmbH). All three are also able to measure temperature. The redundant structure was chosen so that inconsistencies can be detected and small-scale gradients measured. Further information on the mode of operation of the sensors can be found in Bogena et al. (2010) and a more detailed description on the structure of the *soilnet* in *Fendt* in Kiese et al. (2018). Fersch et al. (2018) show results of the *soilnet* in comparison with other soil moisture related measurements.

The raw *soilnet* data from the irregular grid is transferred to a regular grid with 5 m spacing via kriging. The parameters are given in (Fersch et al., 2018). This data is then interpolated to the WRF grid points as described in Section 4.7.

Chapter 5

Results and discussion

In this chapter the results from the conducted simulations are presented. The following three research questions are addressed:

1. can a LES for realistic conditions with only one domain and driven directly by reanalysis data develop turbulent structures that are similar to those seen in idealized or nested models?
2. do the meteorological conditions in the model match those measured in the field and where are the differences?
3. what is the benefit of using LES instead of a much simpler and computationally less expensive mesoscale simulation?

The first question is there to ensure the functionality of the model, the second addresses the quality of the solutions. They have to be answered with yes in order to find an answer to the third question, attempting to transfer the findings from a single point in the domain over the whole modeled area. If the answer for the third question is also yes, then the presented approach for modeling can be used to produce a four-dimensional flow field, with information for every point in space and time. This is not possible with measurements. The discussion of these three questions closely follows Hald et al. (2019).

With the four dimensional data, further studies can be connected: Using the high-resolution *soilnet* data, an additional model run can be constructed, in which the known soil information is connected with the evaluated turbulence and flow information to calculate the fluxes of sensible and latent heat in the area of interest. Due to the high spatial resolution, the dependence of flux patterns on the ground can be investigated and the data can help to find indications of why the energy balance is not closed in the measurements of these fluxes. Three more questions are addressed here:

1. how do the simulated fluxes from the LSM compare to measured fluxes?

2. how do fluxes calculated using the EC-method compare to the measurements and those from the LSM?
3. can patterns in the soil temperature or moisture be detected in the turbulent fluxes above?

5.1 General turbulence development

As noted in the very first question above, the first condition is that the simulation produces turbulent structures in a way that is known from other LES experiments found in the literature. This general development of turbulence in the model domain is shown through the analysis of two distinct cases occurring during the model period, one with low and one with higher geostrophic wind speeds.

Figure 5.1 shows the instantaneous values for horizontal and vertical wind speed during a time period with low horizontal wind speeds, 1000 UTC 16 July 2015. The top panel of Figure 5.1 (a and d) show the values taken from the 9th model level ($\approx$ 100 m above ground). The plot for the vertical wind speed (Figure 5.1d) shows the typical situation for a boundary layer that is driven by buoyancy: spatially small areas with rising air are surrounded by larger patches of downdrafts. These cells of alternating up and downdrafts develop when the ratio between boundary layer height and Obukhov length, z_i/L, is strongly negative. The Obukhov length, L (see Section 2.4.4), is strongly negative. The boundary layer height z_i was determined using the gradient method by Sullivan et al. (1998, Section 2.3).

Deardorff (1972) finds cells at $z_i/L <$ –4.5 and LeMone (1973) at $z_i/L <$ –10. In the shown case, the bulk of the grid points exhibit values between –10 and –25. The total range of is from –60 to 0. Due to the inhomogeneities in terrain and land cover and the changing meteorological drivers, values of z_i/L can vary strongly between adjacent grid points. This is in contrast to idealized simulations, where all grid points are expected to behave equally.

The boundary layer height and the resulting z_i/L is shown in Figure 5.2 for the time shown in Figure 5.1. For both values, a spatial average of 60 by 60 grid points is taken, i.e. for every grid point an average vertical profile of 3600 grid points is calculated. To find the height of the PBL, the largest gradient in the potential temperature is determined in this averaged profile. The Obukhov-length is calculated in the same manner. This approach lowers the variability that is present in smaller averaging spaces or by taking every grid point by itself. The height of the PBL is varying between 0 and 1100 m, with the lowest values being close to the domain edge that is not considered in this evaluation due to edge effects. The average height is

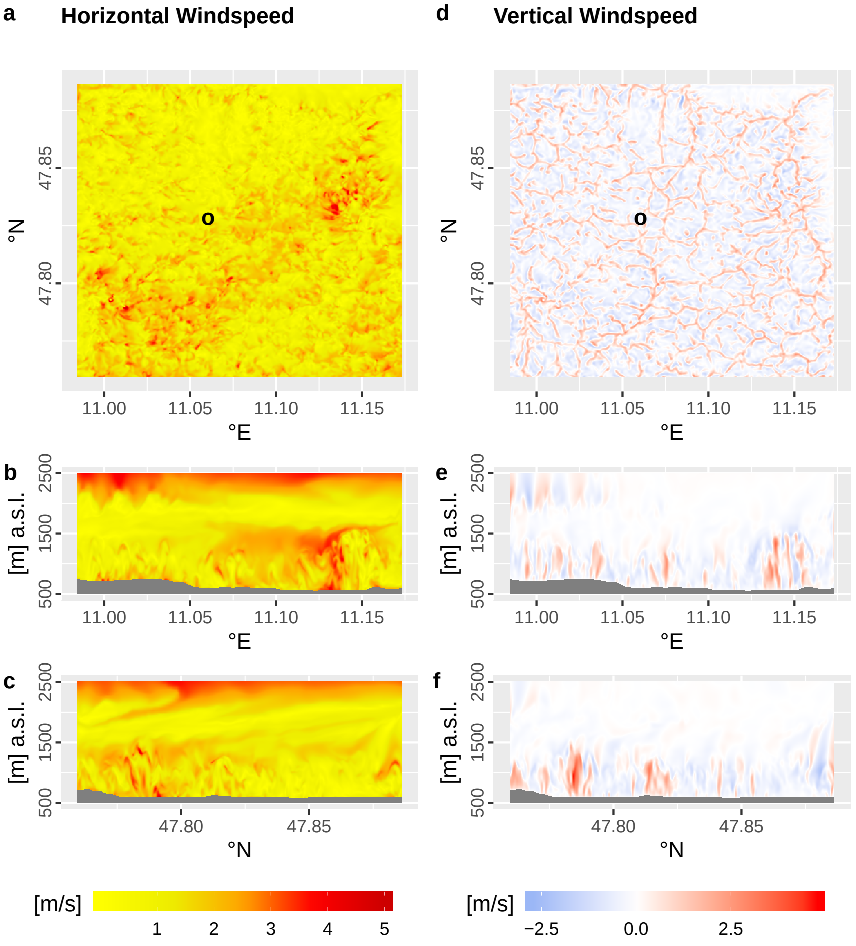

FIGURE 5.1: Instantaneous values of wind components (a-c: horizontal wind speed, d-f: vertical wind speed) for a time step of low horizontal wind speeds (1000 UTC 16 July 2015). a and d: values from the 9th vertical model level (≈ 100 m above ground). The circle shows the position of the *VirtualTower*. b and e: cut from west to east through the *VirtualTower* position. c and f: cut from south to north through the *VirtualTower* position.

between 400 and 600 m over the domain. The highest values are reached at locations with strong thermals, high TKE values and a strong heat flux. z_i/L follows this pattern and shows moderately convective conditions where the PBL height is at an average value, while it indicates strongly unstable conditions where the PBL height is large.

The patterns in Figure 5.1 diverge from their ideal cell-like counterparts taken from idealized LES-Models (see e.g. Moeng et al., 2007) because of a horizontal wind speed larger than zero and inhomogeneities in surface properties and elevation. Modifications due to the underlying height gradients can be seen in the southwestern part of the domain where the mountain is located. On the southeastern slope is an accumulation of grid points

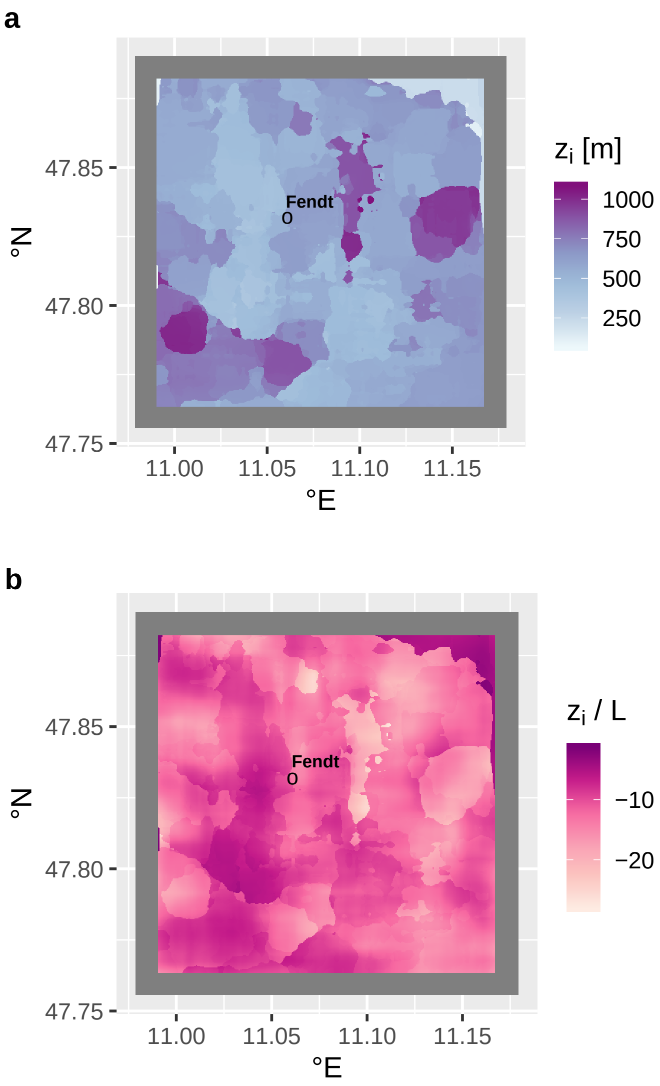

FIGURE 5.2: Boundary layer height (a) and z_i/L (b) for 1000 UTC 16 July 2015. NA values are grey and result from the spatial averaging over 60 x 60 grid points

with rising air (Figure 5.1d), possibly resulting from solar radiation coming in at an angle and heating the slope more than the surroundings. The thermals show rising speeds of up to 5 m s^{-1} while the sinking air never exceeds 3 m s^{-1}.

The lower two rows of Figure 5.1 show vertical cross-sections through the position of the *VirtualTower* from west to east (b and e) and from south to north (c and f). Both cuts reveal an area of distinct shear at about 2000 m a.s.l. This originates from the reanalysis data used to drive the model, as the simulation can not produce shear on its own within this domain. It does not coincide with the boundary layer height, which is at ≈500 m to 700 m above ground during this time (evaluated by the gradient method applied to a spatial mean of 60 by 60 grid points at every grid point). The upper limit of the boundary layer is at the upper maximum extent of the thermal structures, especially visible in Figures 5.1e and f.

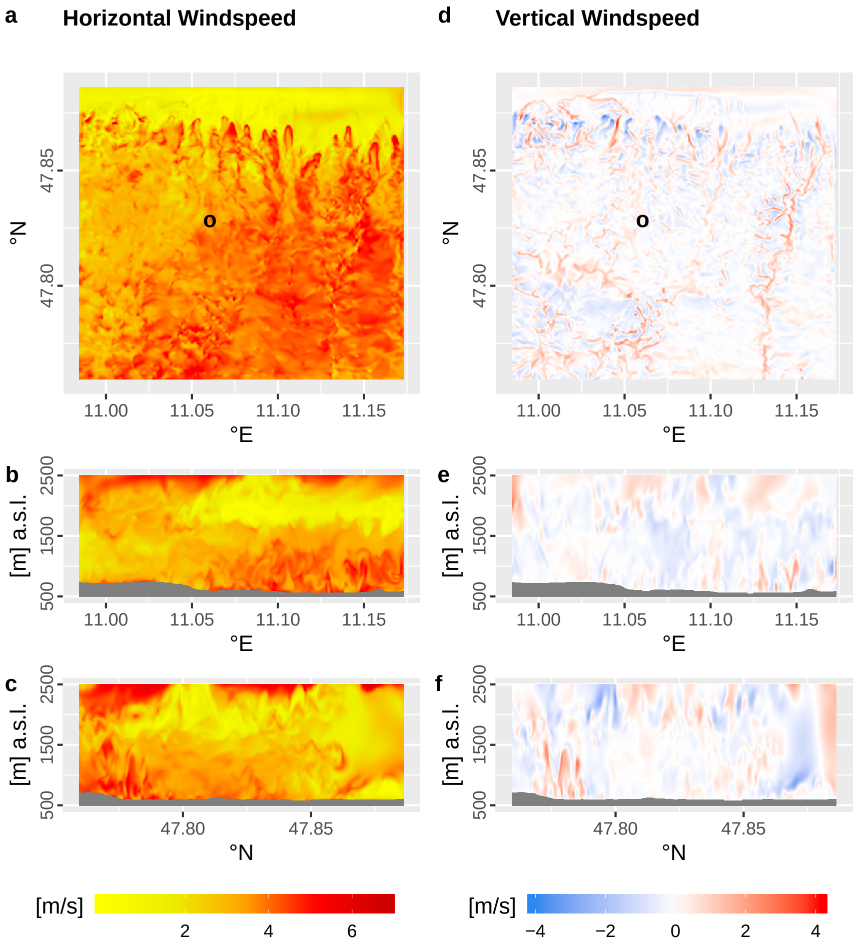

FIGURE 5.3: Instantaneous values of wind components (a-c: horizontal wind speed, d-f: vertical wind speed) for a time step of high horizontal wind speeds (1600 UTC 7 July 2016). Same structure as in Figure 5.1

Figure 5.3 shows a time of high horizontal wind speeds (1600 UTC 7 July 2016) from a northerly direction. Due to the fact that WRF does not use any information about turbulence (e.g. vertical wind speeds or TKE) in the meteorological boundary conditions derived for real cases, turbulence has to develop within the domain. If horizontal wind speeds are larger than 0, this limitation of WRF manifests in areas of underdeveloped turbulence at the inflow edge of the domain, in the case of Figures 5.3a and d at the northern edge. When using WRF in an idealized mode and applying periodic boundary conditions, this problem does not arise, but when nesting another domain within the periodic domain, it can be noted. Several studies have described this behavior: Mirocha et al. (2013) used one way nesting in a neutral boundary layer, finding large streaks of underdeveloped turbulence at the inflow boundary with their extent depending on the used subgrid scale model, the geostrophic wind speed and the horizontal resolution of the model. They find that the NBA subgrid scale model used here shows the best results of the ones that are implemented in WRF and that a higher resolution allows for a quicker development of turbulence. The size of the undeveloped turbulence is dependent on the wind speed: The higher it is, the larger the area. Muñoz-Esparza et al. (2014a) find similar characteristics and propose the application of perturbing the temperature fields at the domain edges. This is applied to a realistic case in Muñoz-Esparza et al. (2014b) and to idealized neutral, stable and convective boundary layers in Muñoz-Esparza and Kosović (2018). It has to be noted that the authors listed here use geostrophic wind speeds of 5 and 10 m s^{-1} (Mirocha et al., 2013), 10 m s^{-1} (Muñoz-Esparza et al., 2014a) and 5, 10, and 15 m s^{-1} (Muñoz-Esparza and Kosović, 2018) as boundary condition. These wind speeds are rather high and responsible for the size of the area of unresolved turbulence. In the case presented here, wind speeds rarely exceed 5 m s^{-1} in the boundary layer (cf. Figures 5.8 and 5.12, ignoring the nocturnal low-level jets that are above the boundary layer). This limits the size of the area of underdeveloped turbulence to what can be seen in Figure 5.3. Additionally, Mirocha, Kosović, and Kirkil (2014) note that the development of turbulence is favored by the presence of slopes in the domain and a positive heat flux at the surface, both of which exists in the modeling approach presented here.

The extent of the space in which no turbulence is developed can be seen on the right side of Figure 5.3c. In this case, with a mean wind speed of 3.4 m s^{-1}, it takes about 50 grid points distance from the inflow edge until turbulence develops near the ground and 150 grid points until turbulence is visible over the whole column. In cases with higher wind speeds the amount of grid points it takes until turbulence is developed fully is significantly larger. This has to be considered when setting the size of the model domain.

More information about the validity of the simulations and a sign that turbulence is indeed developed in the domain can be gathered from the spectrum of the frequencies of turbulence in Figure 5.4. Here the spectra from five different locations in the domain are shown: all are on the same longitude in the center, but on different latitudes. *Far north* is 50 grid points away from the northern edge, *north* 150 grid points, *center* is in the center of the domain, and *south* and *far south* are in 350 and 450 grid points distance from the northern edge, respectively. The data is taken over two hours (1500-1700 UTC 7 July 2016), containing the time step shown in Figure 5.3. Before

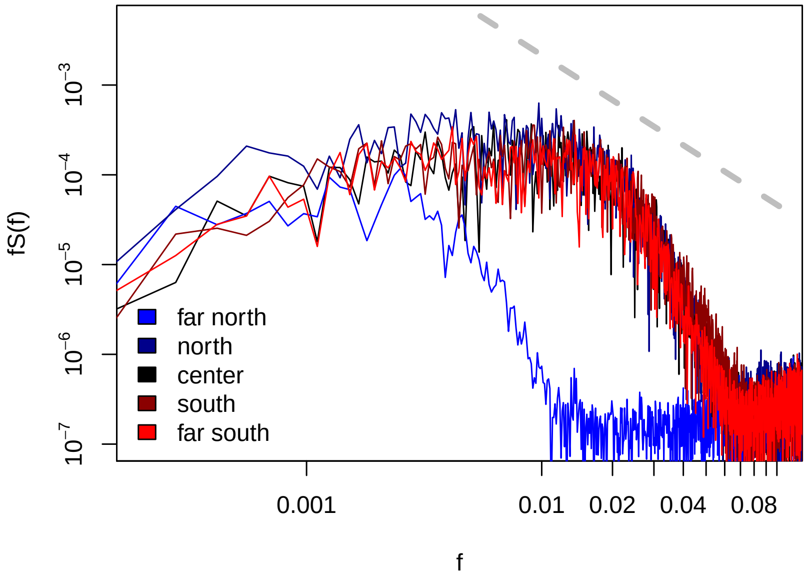

FIGURE 5.4: Spectra of horizontal wind speed at 5 distances from the northern edge: 50 (far north), 150 (north), 250 (center), 350 (south) and 450 (far south) grid points. Data taken from 2 hours of model data (1500-1700 UTC 7 July 2016) and averaged over 3 vertical levels (55 m to 77 m over ground). The grey dashed line is $f^{-\frac{5}{3}}$. It marks the inertial subrange.

performing the Fourier transformation, the data is de-trended and tapered by the use of a cosine bell taper to the first and last 10 % of the data, following the instructions in Stull (1988) by using the function ′spec.taper′ in the statistics software R. Shown are resolved frequencies in the horizontal wind speed. Only the point closest to the inflow edge shows a underdeveloped spectrum, where only the largest structures are resolved and spectral densities drop at high frequencies. All other points show similarly developed spectra with a distinctive inertial subrange. This proves that the simulation results presented here are valid and can be used further, under the condition that grid points without developed turbulence are omitted from the analysis.

In terms of stability criteria, the period shown in Figure 5.3 is different to the one in Figure 5.1: Values for z_i/L are in the range of 0 to –13 over the whole domain. In contrast to cells forming, these values are within the range shown by LeMone (1973) and Deardorff (1972) to possibly produce roll like structures in the boundary layer. A comprehensive review on these rolls can be found in Etling and Brown (1993). There are elongated structures present in Figure 5.3, especially visible in the vertical wind speeds in

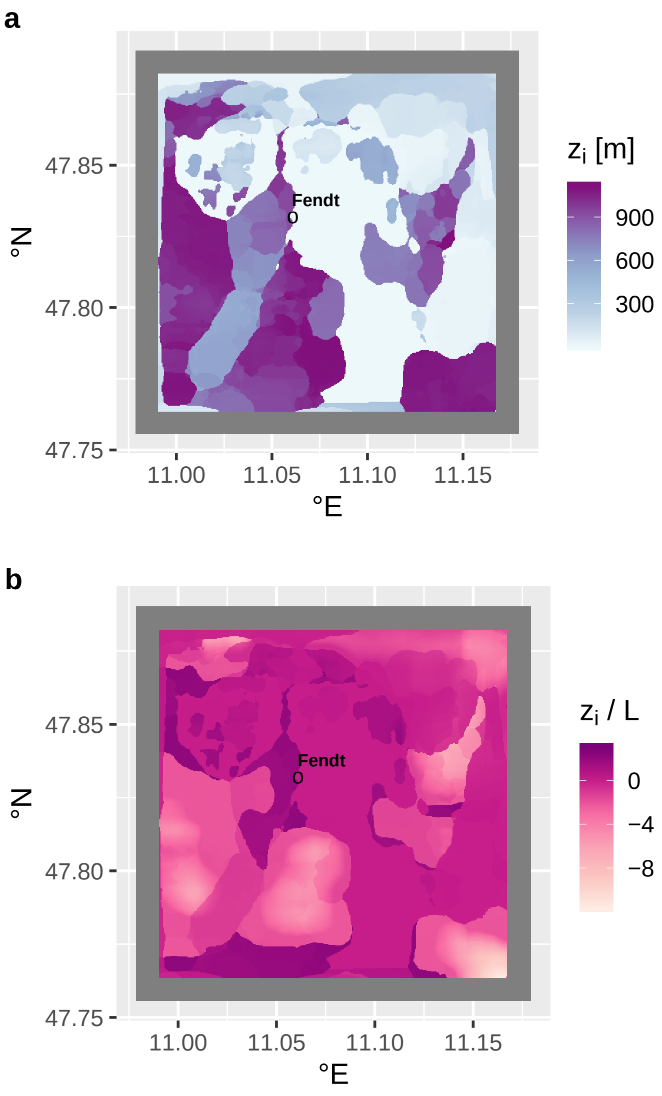

FIGURE 5.5: Boundary layer height (a) and z_i/L (b) for 1600 UTC 07 July 2016. NA values are grey and result from the spatial averaging over 60 x 60 grid points

the eastern part of the domain.

During these conditions the determination of the PBL height by use of the gradient method applied to instantaneous values of temperature has its limitations, as can be seen in Figure 5.5. The range is similar to the one shown in Figure 5.2, but the variability within the domain is higher. Unrealistically low heights are adjacent to very high values. The distribution is in agreement with the horizontal wind speed, especially the north-south component: Very low PBL heights are in areas with high wind speed, while the high values are where V is low. z_i/L is more homogeneous, with slightly unstable conditions prevailing. Where the wind speed is low, convective effects have a stronger influence and the layering is more unstable.

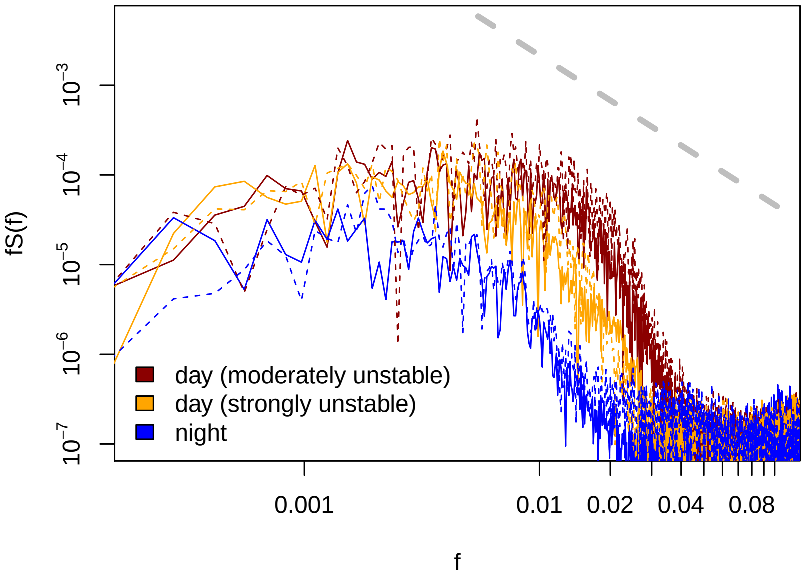

FIGURE 5.6: Spectra of horizontal (solid line) and vertical (dashed line) wind speeds for periods of strongly convective, moderately convective and stable (night) periods. Values taken from 15 vertical levels down from the average boundary layer height over a period of 2 hours. The grey dashed line is $f^{-\frac{5}{3}}$.

The simulated periods of twice 48 hours encompass several states the atmospheric boundary layer can be in. Instances of strongly and moderately convective periods are shown in Figures 5.1 and 5.3, respectively. Neutral stratification is a theoretical construct that happens very rarely in nature. It can be found at times when the unstable boundary layer turns stable or vice versa. These conditions are present during sunset and sunrise. The stable boundary layer on the other hand occurs in most nights. Stable nocturnal boundary layers are characterized by low wind speeds and a strong negative temperature gradient with height. The stable layering dampens turbulence, the turbulent structures are smaller than during day (e.g. Stull, 1988). The smaller the turbulent structures, the smaller the model resolution has to be in order to resolve these structures.

Figure 5.6 shows spectra from times of strongly and moderately convective periods and a night period at the location of the *VirtualTower*. To keep the data comparable, it is in all three cases taken from the 15 vertical levels below the averaged boundary layer height during the time considered. During day, the boundary layer height is determined by using the gradient method. The determination of the nocturnal boundary layer height cannot be accomplished by searching for the largest gradient in the potential temperature, because these gradients are within the boundary layer. Its height is limited by the residual layer above, in which the temperature gradients with height are small. As there is, to the author's knowledge, no formal method of determining the height of the nocturnal boundary layer, it is defined here as the height in which the gradient in potential temperature falls below 5% of the largest gradient measured beneath (see Equation 2.4).

It is evident that turbulence in the moderately convective case shown in Figure 5.6 is best resolved. This is the time shown in Figure 5.3, characterized by high horizontal wind speeds. The spectrum for the strongly convective case is less well developed, there is less power on smaller scales. One reason is that turbulent structures that are predominantly caused by buoyancy are comparatively large. Another factor might be that this data is taken from the 2015 simulation that uses a slightly larger time step. Nevertheless, the inertial subrange is developed. During night the spectrum shows some scales of resolved turbulence. The total intensity is lower than in the two other cases, which is to be expected due to the smaller eddies present in the nocturnal boundary layer. An inertial subrange is discernible, but it is smaller than in the other two cases. In all three cases, the intensities in the vertical wind speed are higher than in the horizontal wind. According to Kaimal and Finnigan (1994), a spectrum shows atmospheric turbulence, when an inertial subrange is present and when the ratio in the intensities between streamwise and vertical wind speed in this inertial subrange is $4/3$. In the shown case the ratio is always positive, but ranging between 1 and 4. This is because the frequency range of the inertial subrange has to be determined by hand and a small shift gives very different results. It is also assumed that the fact that the vertical resolution in this simulation is three times as fine as the horizontal resolution leads to more intensity in the vertical portion of the turbulence. The conclusion from Figure 5.6 is that the resolution of the models is sufficient for well-developed turbulence during daytime, but may be too coarse to properly resolve nighttime turbulence.

5.2 Comparison with *VirtualTower*

The model data for the comparison with the *VirtualTower* wind measurements was taken from four grid points in a 2x2 pattern at the location of the *VirtualTower*. To weaken the influence of outliers, the data was averaged in horizontal space and in time. For the height comparisons, the *VirtualTower* data was linearly interpolated to the model height levels.

Figures 5.7 and 5.8 show the wind directions and wind speeds in the column above the *VirtualTower* for a) the model and b) the measurement in

2015. The directions were calculated from the meridional and zonal wind components, averaged over 10 minutes. Both figures only contain the time steps at which data is available for both the model and the *VirtualTower*. Dotted vertical lines mark the timing of the sunset, dashed lines mark the sunrise.

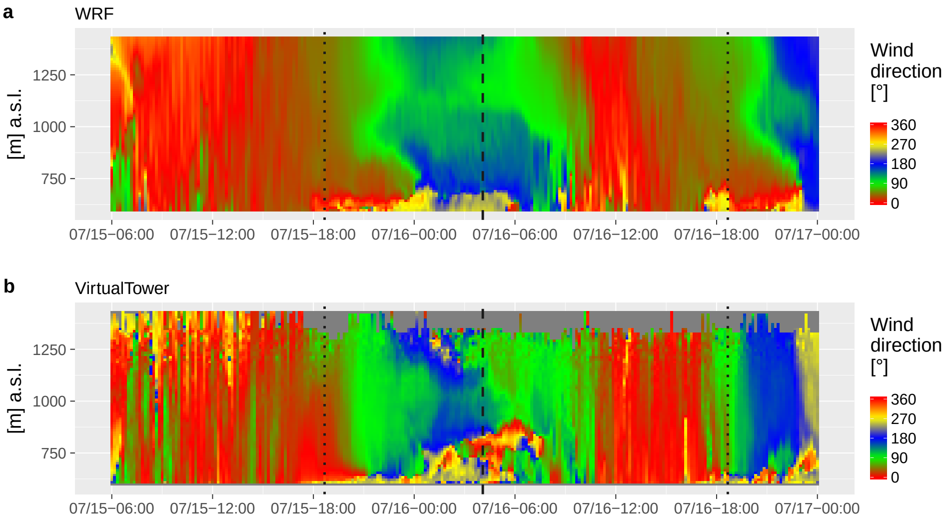

FIGURE 5.7: Wind directions from a) WRF-LES and b) the *VirtualTower* for the 2015 simulation period. Model data taken from 4 grid points in a 2x2 pattern and horizontally averaged. Values are temporally averaged to 10 minute means. *VirtualTower* data linearly interpolated to model levels. Dashed lines: sunrise, dotted lines: sunset. Time steps are on the x-axis, heights above sea level on the y-axis. Values of direction are color coded, NA values due to the limited measurement height of the *VirtualTower* are dark grey.

The comparable period in 2015 contains 42 hours spanning from 0600 UTC 15 July to 0000 UTC 17 July. The first day, according to the measurements, is characterized by a well mixed daytime boundary layer with winds coming from northeast. These conditions are reached in the model by about 1500 UTC. Before that, the model shows an area of shear rising from the ground at 1000 UTC up to 1250 m a.s.l. at 1500 UTC. Above, the wind comes from northwest. After 1500 UTC the model represents the directions measured by the *VirtualTower*. This coincides with growing wind speeds from 2 m s^{-1} to 5 m s^{-1} (see Figure 5.8). After sunset (dotted line), both the model and the measurement show a shift in the wind direction from northeast to east, and in the second half of the night, to south. During night time a shallow nocturnal boundary layer develops. It is characterized by mostly westerly wind direction and very low wind speeds. The nocturnal boundary layer grows to a depth of about 110 m in the model and 150 m in the measurement during the second half of the night. The height of the nocturnal boundary layer is again determined by using the method described in Section 2.3.

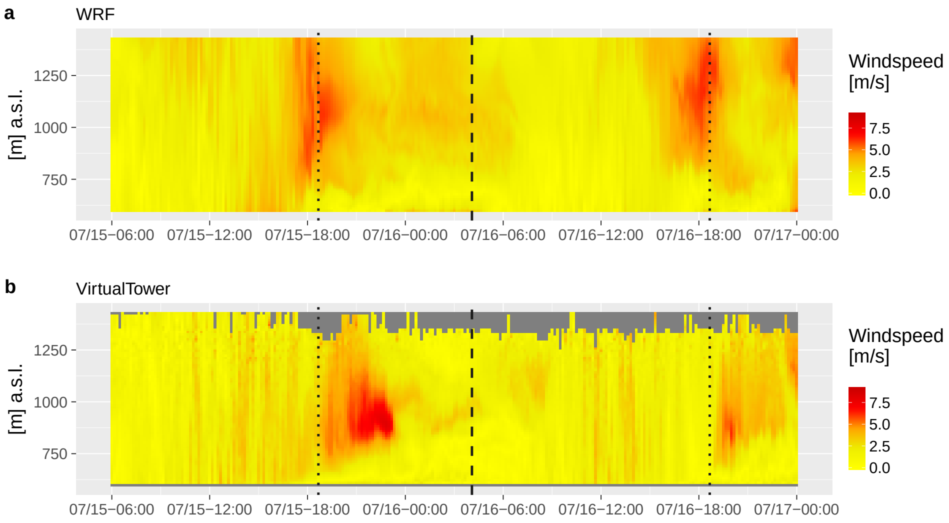

FIGURE 5.8: Wind speeds from a) WRF-LES and b) the *VirtualTower* for the 2015 simulation period.

After sunrise (dashed line) the differences between model and measurement are largest: The observations show that the nocturnal boundary layer starts to transition into the daytime boundary layer after 0600 UTC near the ground with residuals remaining at around 200 m above ground. After the disappearance of the residuals the boundary layer becomes well mixed again with homogeneous directions (east) over the whole column. The model does not capture the growth of the nocturnal boundary layer up to the measured depth during night and simulates wind from south during the morning with a region of shear at 1000 m a.s.l. Starting at around 1100 UTC, the agreement between model and measurement improves. Both show a well mixed boundary layer with wind coming from northwest with increasing wind speeds during that time. During the evening, both show a shift from north over east to south. In the model this happens gradually while the changes in directions are very distinct in the measurements. In both cases, a new shallow nocturnal boundary layer develops.

As can be seen in Figure 5.8 the most prominent feature of the measurements of wind speeds is the low-level jet (LLJ, e.g. Stull, 1988) during the first night at around 900 m a.s.l. It coincides with the top of the stable nocturnal boundary layer and is characterized by high wind speeds in relatively low heights. In many cases it is faster than the geostrophic wind above. The speed shown here grows immediately after sunset to 5 m s^{-1}. It reaches its maximum at 2300 UTC with just below 8 m s^{-1} with a vertical extent shrinking from almost 400 m to 100 m. The jet comes exclusively from the east and disappears suddenly at 2300 UTC, while the wind direction is shifting to the south. WRF-LES does capture the phenomenon of the LLJ, but the representation is insufficient. The simulated jet appears before sunset with the maximum approximately 5 hours early and 200 m higher. The vertical extent is strongly exaggerated and the maximum wind speeds are underestimated by about 2 m s^{-1}. Due to the shift in time, the simulated jet appears to come from northeast. A less pronounced LLJ can be found during the second night. The representation in the model shows the same shortcomings in timing, height and vertical extent as during the first occurrence.

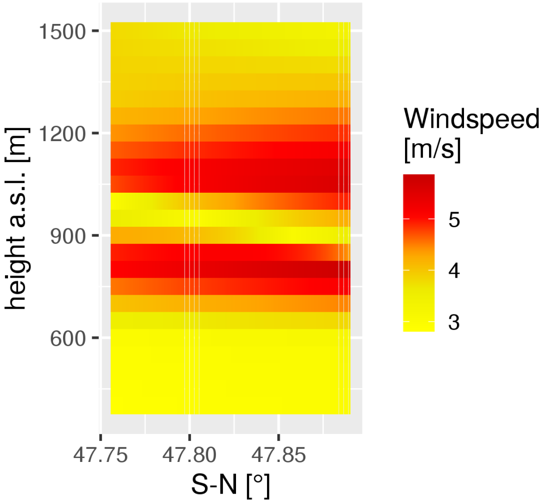

FIGURE 5.9: Wind speed in the meteorological boundary conditions for 15 July 2015, 1800

The reason for the misrepresentation of the LLJ in the model data is the representation of the LLJ in the reanalysis data used as boundary conditions. The LLJ is not a local phenomenon and is not created within the domain. In the reanalysis data used as boundary conditions the temporal and vertical resolutions are not high enough. The ERA-Interim reanalysis uses 38 vertical levels up to a height of 50 km. While no sign of the LLJ is visible in the boundary conditions for 1200 UTC 15 July 2015, it is clearly visible as higher wind speeds in the boundary conditions for the next time step at 1800 UTC (see Figure 5.9). They reach 5.7 m s^{-1} in the fourth level at 820 m a.s.l. and 5.5 m s^{-1} and 4 m s^{-1} in the levels 6 and 7 (1060 and 1300 m a.s.l.). The 5th level in between at 930 m a.s.l. and those above the 7th and below the 4th show lower speeds of 3 m s^{-1}. 1800 UTC is exactly the time when the LLJ appears in the simulated data, as can be seen in Figure 5.8a. It also explains the vertical stretching, caused by the high wind speeds in the reanalysis from 820 to 1300 m a.s.l. and the lower maximum wind speeds of the simulated LLJ compared to the observed, caused by maximum wind speeds of 6.1 m s^{-1} in the reanalysis. In the next set of boundary conditions that is applied at 0000 UTC 16 July 2015, no signs of the LLJ are present in the data and the wind speeds in all essential vertical levels are below 3 m s^{-1}. For a proper representation of the LLJ in WRF-LES, boundary conditions with a high temporal, for example hourly, and a high vertical (<100 m) resolution are required.

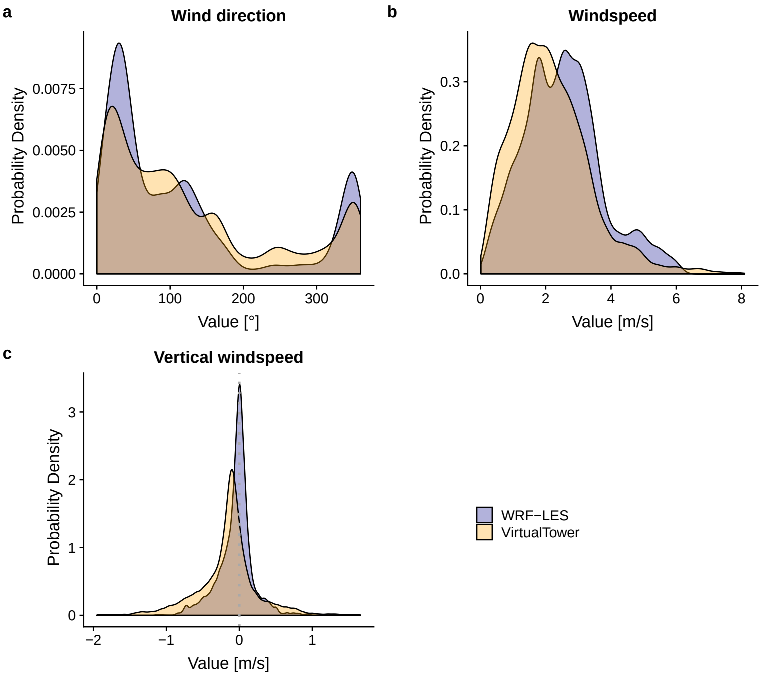

FIGURE 5.10: Density plots of measured and simulated values for a) wind direction, b) horizontal wind speed and c) vertical wind speed from the 2015 simulation period.

The temporal course of the vertical wind speeds (not shown) behaves as is expected: during day and actively incoming solar radiation the 10-minute averaged vertical wind speeds easily reach ±2 m s^{-1} with alternating up- and downdrafts at the *VirtualTower* location. After sunset the vertical motions are quickly dampened and stay below ±0.5 m s^{-1}. Directly after sunrise the turbulence starts weak and takes another 3 hours to reach the strength and vertical extent of the day before.

Density plots of the three discussed variables (direction, horizontal and vertical wind speed) in Figure 5.10 give a broader picture. They show only time steps and heights where both model data and measurement data are available. The direction is simulated well, model and measurement show a distinct maximum around north. The secondary maximum at 100° in the measurements is shifted towards south in the model. Westerly directions are rare in measurement and model. The distributions of the horizontal wind speeds (Figure 5.10b) show two distinct features: the bulk of the wind speeds is slightly overestimated by the model (limit for the first quantile in the model: 1.69 m s^{-1}, measured: 1.33 m s^{-1}), while the maximum wind speeds are underestimated. These maximum wind speeds in the measurements (7.83 m s^{-1}) occur in the center of the LLJ that is, as described above, insufficiently represented in the model. The maximum wind speed in the model reaches 6.23 m s^{-1}. The simulated vertical wind speeds (Figure 5.10c) show a clear mean close to zero (–0.05 m s^{-1}), matching the theory of turbulence according to which vertical motions will average to zero over a sufficiently long time period. The mean of the measured values deviates from 0 and has a value of –0.15 m s^{-1}, hinting at possible surface inhomogeneities that favor downdrafts at the location. The model can not represent this. Both distributions of vertical wind speeds are skewed towards negative values. This is to be expected, since within one convective structure the area on which air rises is small compared to the area on which it sinks. If these structures pass by the *VirtualTower* with the horizontal wind speed, the device will measure downdrafts for a longer time than updrafts.

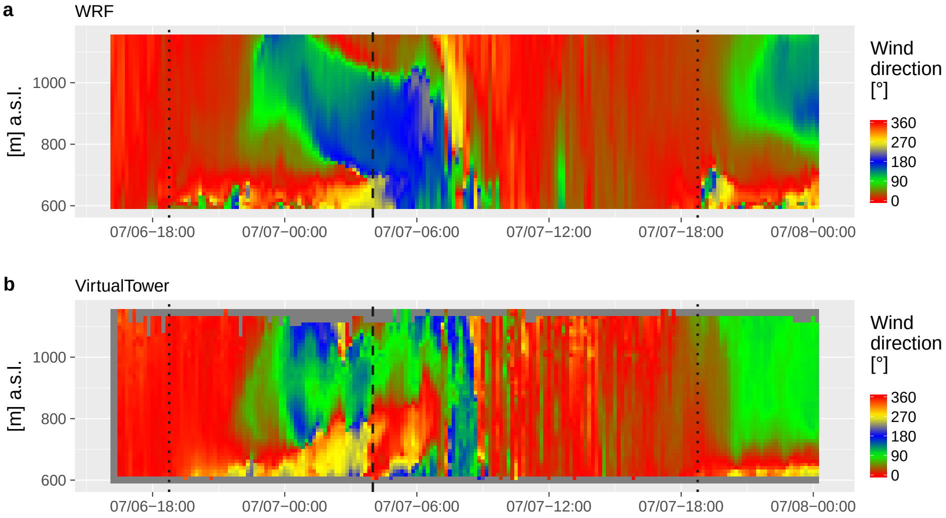

FIGURE 5.11: Wind directions from a) WRF-LES and b) the *VirtualTower* for the 2016 simulation period.

The comparable period for the 2016 model covers 32 hours from 1600 UTC 6 July to 0000 UTC 8 July and therefore contains two sunsets and one sunrise. Both measurement and simulation show high wind speeds of up to 6 m s^{-1} (see Figure 5.12) coming from the north (Figure 5.11) before the first sunset. These high wind speeds were the reason for the required smaller model time step of the 2016 model in comparison to the 2015 model. The high wind speeds disappear during the first nighttime hours in the measurements, while a shallow nocturnal boundary layer develops. Simulated wind speeds diminish about one hour earlier. During the second half of the night, directions shift from north over east to south while the wind speeds are low. The model captures this shift very well in timing and vertical extent. It also hints at an area of shear between 1000 m and 1200 m a.s.l. that can not be validated by the measurements. Both model and measurement show a growth of the nocturnal boundary layer depth during nighttime, while its maximum depth is again underestimated by the model. After sunrise the largest differences in the wind directions can be found. While the measurements show the dissipation of the nocturnal boundary layer due to beginning convection and northwesterly directions within the residuals, the model shows an extension of the conditions above the nocturnal boundary layer down to the ground with southerly directions. The position of the area of shear sinks down accordingly. It has to be noted that the determination of a wind direction from the horizontal wind components during times of low wind speeds, as they can be found here, are less reliable. Starting at 0900 UTC 7 July 2016, the agreement between model and measurement improves again. Both show northeasterly wind directions and growing wind speeds. The measured layer of the atmosphere is well mixed up to the maximum measurement height. After the second sunset the directions in model and measurement agree well, both showing the here often found pattern of a shift from north over east to south. The wind speeds, however, show the model limitation already mentioned in the 2015 data: the LLJ occurring between 800 m and 1000 m a.s.l. after sunset is misrepresented by the model. Here it again occurs earlier and before sunset and the vertical extent is exaggerated. Due to the shift in time, the direction of the LLJ (east) is also not represented in the simulation.

The repeating pattern of northerly wind direction during the day and southerly direction during night, which is observed during both simulation periods, is a consequence of the alpine pumping (Lugauer and Winkler, 2005; Graf et al., 2016). This process is represented in the simulation, despite being a mesoscale phenomenon. While its origin is present neither in the boundary conditions, nor in the LES itself, its modification of the wind field is existent in the reanalysis data. This shows that mesoscale influences are only then absent in the simulation if both the origin and the effect of the phenomenon are not representable on boundary condition or LES scales.

Conditions for the vertical wind speed are very similar to the 2015 model period. During the day, updrafts and downdrafts reach up to ± 2 m s^{-1}. After sunset the vertical motions disappear, first near the ground while the air above the forming nocturnal boundary layer is still in motion, later over

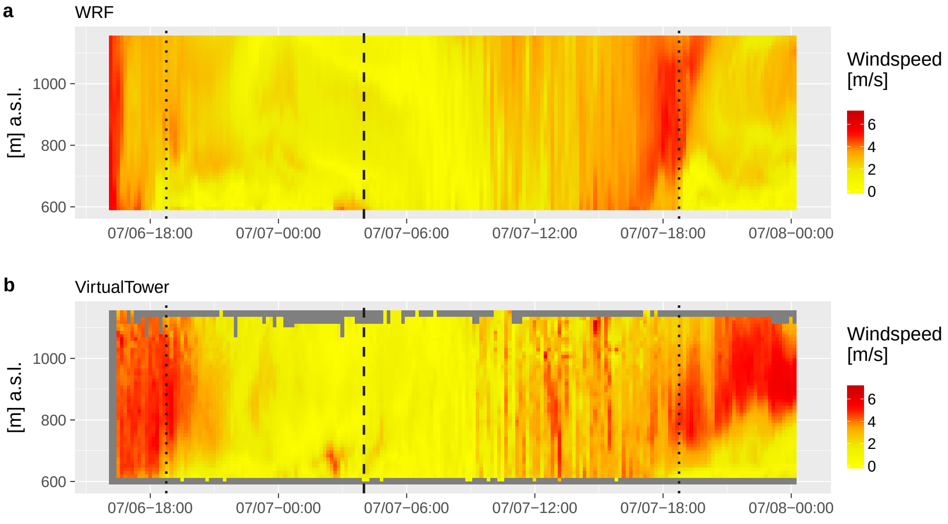

FIGURE 5.12: Wind speeds from a) WRF-LES and b) the *VirtualTower* for the 2016 simulation period.

the whole column. After sunrise it takes about three hours until the high vertical speeds are reached again.

The density plots (Figure 5.13) for the three measured and simulated variables show a similar picture as in the 2015 model period: directions (Figure 5.13a) are mostly north. The secondary maximum of the simulated values at south represents the mismatch between model and measurement just after sunrise on 7 July 2016 (Figure 5.11). The two conclusions made from the wind speed data of the 2015 simulation hold true for 2016: the bulk amount of wind speeds is overestimated by the model (limit for the first quantile in the model: 1.51 m s^{-1}, measured: 1.23 m s^{-1}) and maximum wind speeds are underestimated: the model values only reach 5.2 m s^{-1} while speeds up to 6.59 m s^{-1} were measured during the simulation period. Figure 5.13c, showing the distributions of the vertical wind speeds, also confirms the findings from the 2015 model: the mean of the measured values is strongly negative (–0.25 m s^{-1}) in comparison to the simulation mean of –0.04 m s^{-1}. Both distributions are skewed towards negative values.

5.3 Additional value of model output

Considering the small size of the domain it is possible that WRF-LES with the setup described above primarily mixes the values prescribed by the boundary conditions with little connection to the actual properties of the selected area. To disprove this, a phenomenon within the model data has to be found that is spatially or temporally so confined that it can not originate from the boundary conditions. One such phenomenon can be seen on

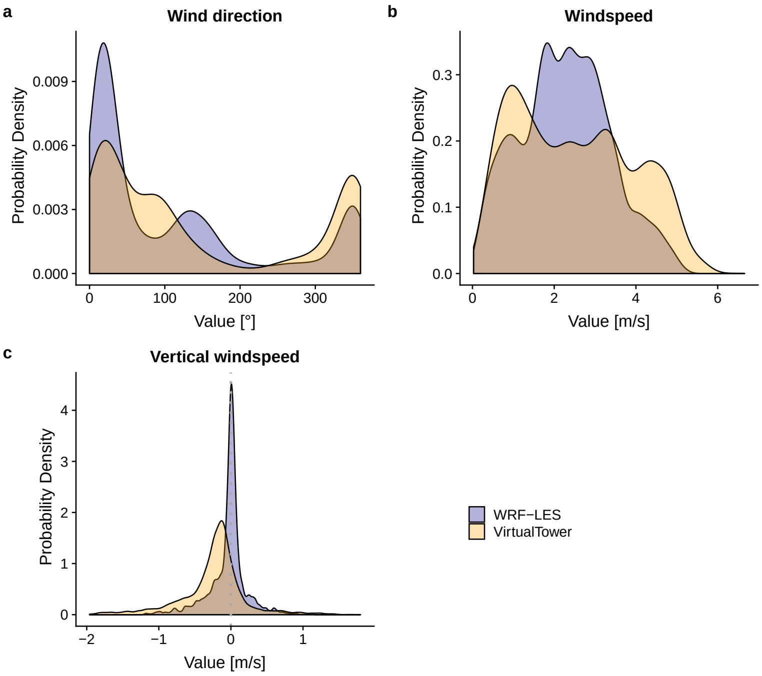

FIGURE 5.13: Density plots of measured and simulated values for a) wind direction, b) horizontal wind speed and c) vertical wind speed from the 2016 simulation period.

0210 UTC 7 July 2016, where the measured wind speeds close to the ground are increasing from <2 m s^{-1} to 5 m s^{-1} for 50 minutes (Figure 5.12b). The phenomenon reaches 150 m in height. The wind is coming from the west (Figure 5.11b). A similar phenomenon is visible in the model data during the same time. The duration is overestimated (90 minutes from 0230 UTC to 0400 UTC), while height (70 m) and value of the wind speed (4 m s^{-1}) are underestimated. During the high wind speeds in the model, the wind direction is also west, as seen in the measurements. This phenomenon is not represented in the boundary conditions and has therefore to originate from the local conditions. Measurements during other times have proven that this phenomenon occurs regularly, always shortly before sunrise and especially during summer. With just the point or column measurements the origin can not be reconstructed. Here, the four dimensional output of the model is a useful tool.

Figure 5.14 shows simulated wind speed data during the time of the phenomenon described above. Each panel shows an area of 3.5 by 3.5 km surrounding the *VirtualTower* (white spot in the center). Just west of the *VirtualTower*, the western ridge (see Figure 4.4) is indented by a small valley from west to east. Starting at 0130 UTC the conditions seen in Figure 5.14a begin to develop: a significant flow from the mountain in the southwestern corner of the domain brings excess air towards the small valley. This forms

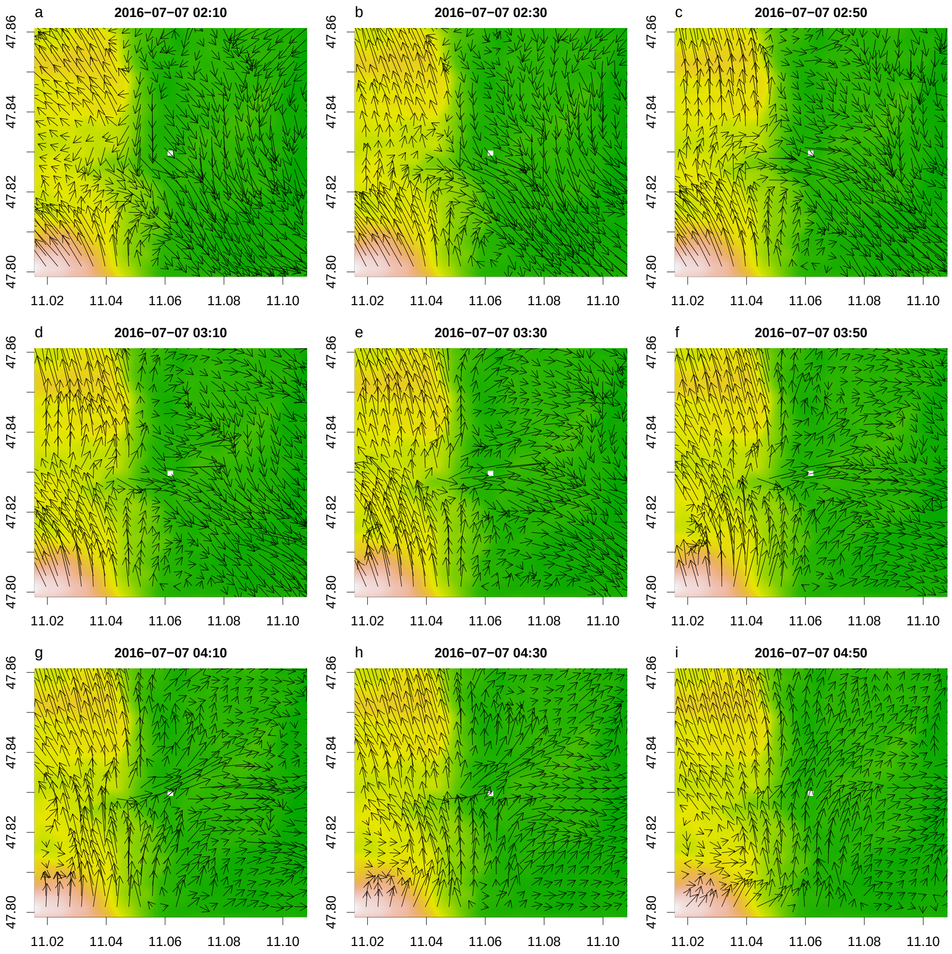

FIGURE 5.14: Temporal development of the flow passing the *VirtualTower* (marked by the white spot) in the early morning of 7 July 2016. Arrows are scaled by the wind speed. Speed data averaged over four vertical levels between 33 m and 66 m above ground.

a pool of cold air with a vertical extent of over 50 m on the ridge west of the *VirtualTower*, illustrated by the blue layer of relatively cold air on the left side of Figure 5.15a. The air here is up to 4 K colder than the average (9 °C) over the observed area up to 850 m a.s.l. and the horizontal wind speed is below 1 m s^{-1}. The cold air leaves the ridge through the valley and accelerates on the plain. Data from the vertical wind speeds show constantly negative values of up to –0.6 m s^{-1} on the steepest part of the slope during the whole second half of the night. This in turn also increases the horizontal wind speeds near the ground. On the plain the flow is deflected towards the south (Figures 5.14a-c) in accordance with the wind direction just above the nocturnal boundary layer measured at the time (cf. Figure 5.11). Due to this deflection, the flow is not measured by the *VirtualTower* until later.

In the following hours (Figures 5.14d-f) the deflection is weakened and the flow takes a more straight western direction. It is during that time that the *VirtualTower* measures increasing wind speeds in low heights. It is also the time in which the vertical extent of the flow reaches its maximum with about 70 m while it was more shallow before. Simultaneously, the depth of the cold air reservoir on top of the ridge shrinks to below 10 m and the deviations from the temperature mean are reduced from –3.2 K to –2.7 K (Figures 5.15d-f, marked by the depth of the blue layer on the left side of the panels). The diminishing gradient is a hint that the cold pool is no longer replenished by flow from the mountain.

Soon after, the deflection takes an opposite sign and gives the flow a northward component (Figure 5.14g), making it pass by the *VirtualTower* to the north. Vertical wind speeds during this time on the slope are still negative, but take an absolute lower value of –0.1 m s^{-1}. The *VirtualTower* only measures this flow during a short moment in its transition from a southward to a northward deflection. Soon afterwards, the sunrise dissolves the temperature gradient on the western hill (visible as the more and more shallow blue layer on the ridge in Figures 5.15g-i), stops the katabatic flows (Figures 5.14h and i) and the flow in the plain vanishes. The temperature deviations on the hill drop to –1 K in the last shown two time steps (Figure 5.15h and i).

If the measured spike in wind speeds really is the result of the described katabatic flow would have to be determined by additional measurements, but the results show that the model data can easily be used to identify possible drivers, while requiring much less effort than measurement campaigns.

To analyze such micrometeorological events, the used simulation has to be run in a very high resolution: the horizontal resolution has to be fine enough to resolve the fine gradients in the elevation model and the vertical resolution has to have enough levels close to the ground that the shown strong temperature gradients can be resolved. LES are the only approach for this scale at the moment: the parameterizations that mesoscale models depend on can not be used in such high resolution and direct numerical simulations are computationally too expensive for an area the size of this.

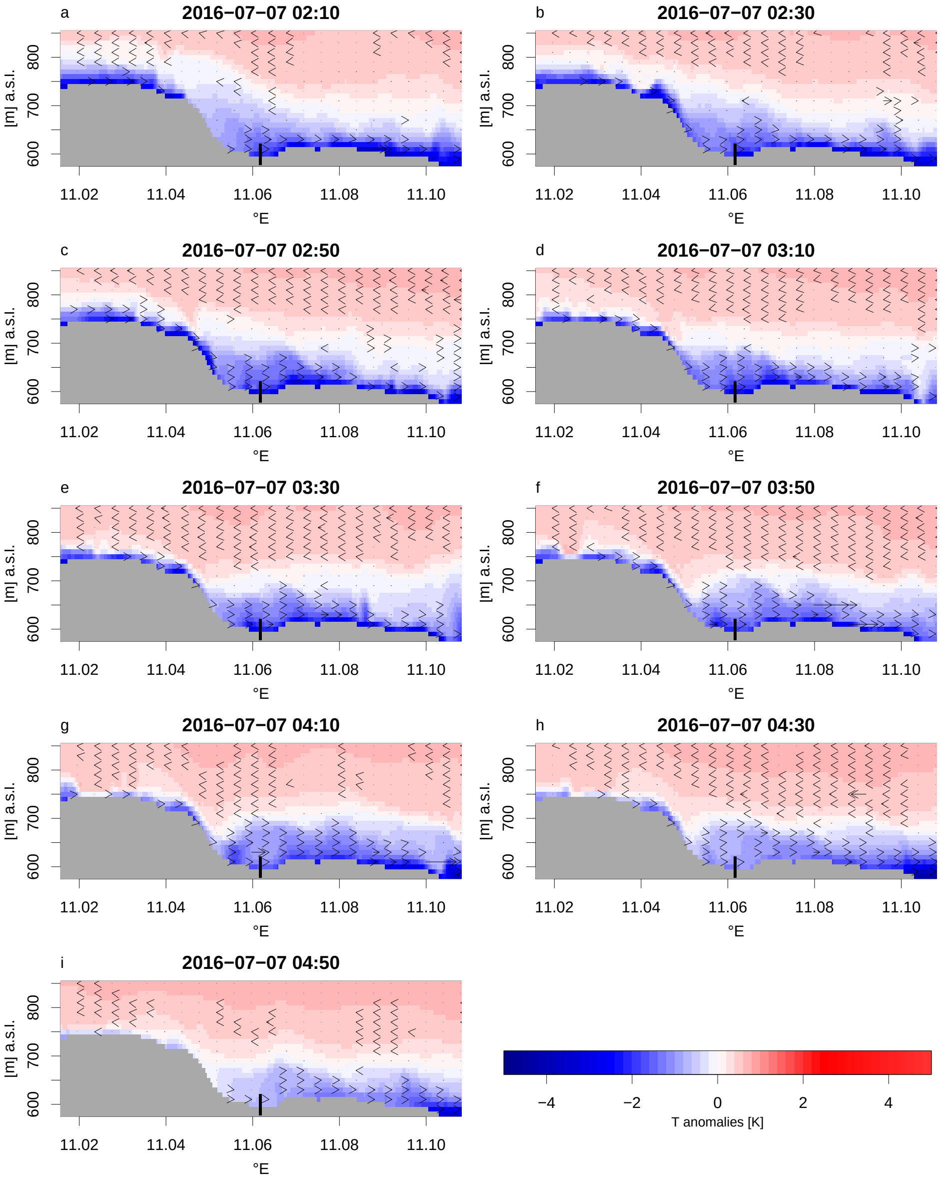

FIGURE 5.15: Temporal development of the potential temperature deviations for the time steps shown in Figure 5.14. The deviations are calculated from the mean of all data points (temporal and spatial averaging). Cut from west to east through the position of the *VirtualTower* (the black "I").

5.4 Results of *soilnet* model

As was shown above, the WRF-LES configuration driving a single domain directly with meteorological boundary conditions taken from reanalysis data can represent the local conditions and improves the data situation over measurements. The same setup can be applied to a set of initial conditions with adapted soil moisture and temperature, as described in Section 4.7. The results of that model run can be evaluated in a multitude of ways: First, the differences of the fluxes from the *Noah* LSM between the models with and without adapted soil information will be shown and compared to the measurements of the EC-station. A second part takes the evaluation of the fluxes calculated with the EC-method from LES data. The last part of the evaluation is a closer look at the spatial differences between grid points, something that is not possible with measurements.

The evaluation of fluxes is limited to the 12 hours between 15 July 2015 0600 UTC and 1800 UTC. This period is characterized by low general wind speed from a constant direction (N) without clouds or precipitation. The EC-station produced a continuous time series of valid observations during the time. Starting at 0600 UTC allows for a sufficient spin up time of 6 hours in the model. Details on the wind field characteristics can be found in Figures 5.7 and 5.8. The prevailing northerly wind direction means that the *soilnet* is downwind of the EC-station and will not be part of its footprint. The evaluation of the EC-station data showed that these are the typical conditions during warm, sunny days and autochthonous weather situations. Cases with southerly wind directions always occur together with changing large scale influence and often times with rain, both of which would further complicate the flux evaluation. It will become evident that the comparison with the EC-station is limited due to the unclosed energy balance, for which reason the problem of the footprint was ignored in the evaluation.

A second limitation lies in the height of the data availability: The EC-station measures in 3.5 m height. A comparison with model data from here is not possible, because the first model level is excluded from the evaluation due to the use of MO and the resulting parameterized fluxes. The lowest height for which LES fluxes are given is therefore $\approx$15 m or the middle of the second grid box from the ground.

5.4.1 Comparison of LSM fluxes with those from the original model and the EC-station

The first condition for a meaningful evaluation of fluxes is that the total amount of available energy that is later distributed by turbulent fluxes, is the same in measurement and model. In both cases this can be described by the net radiation, which is the sum of incoming longwave and shortwave radiation minus the ground heat flux. The temporal development is shown in Figure 5.16 for the original model run described in the previous sections, the *soilnet* run with the adapted soil information and the measurements of the EC-station. The data is taken from the 30 grid points shown in Figure 4.11 and averaged horizontally.

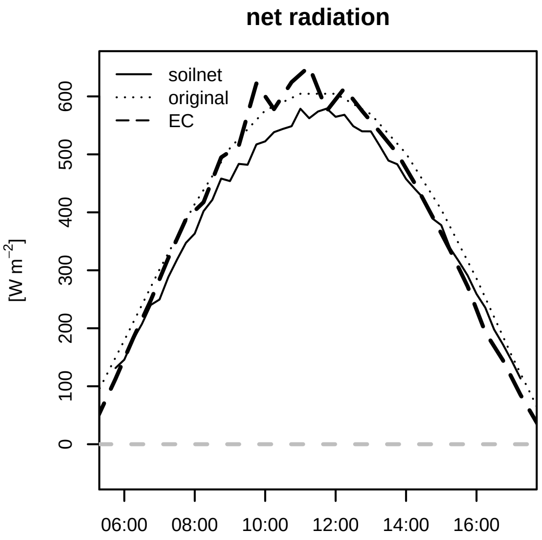

FIGURE 5.16: Temporal development of the net radiation for the unchanged model run, the run with *soilnet* information and the EC-station

The figure shows that the available energy is very well comparable. The temporal course is well matched by the model and absolute deviations between model and measurement are, apart from single values, below 10% of the total net radiation. The differences between the two model runs arise from different values in the ground heat flux, which is about double in magnitude in the *soilnet* run compared to the unchanged model run. This is a result of the changed soil information. Modeled net radiation in the *soilnet* run is above the measured values in the morning and afternoon, and lower during noon. The accumulated net radiation for the evaluated 12 hours reaches 16700 kJ m^{-2} in the *soilnet* model and 17500 kJ m^{-2} in the measurements.

With similar amounts of energy available in both model and measurement, the resulting fluxes should be comparable, too and their distribution in latent (LH) and sensible (HFX) heat flux is expected to be similar, if the properties of the ground are realistic in the model. This comparison is shown in Figure 5.17, again for both the model with and without *soilnet* data. Model fluxes are taken from the *Noah* LSM and are averaged horizontally over the 30 evaluated grid points.

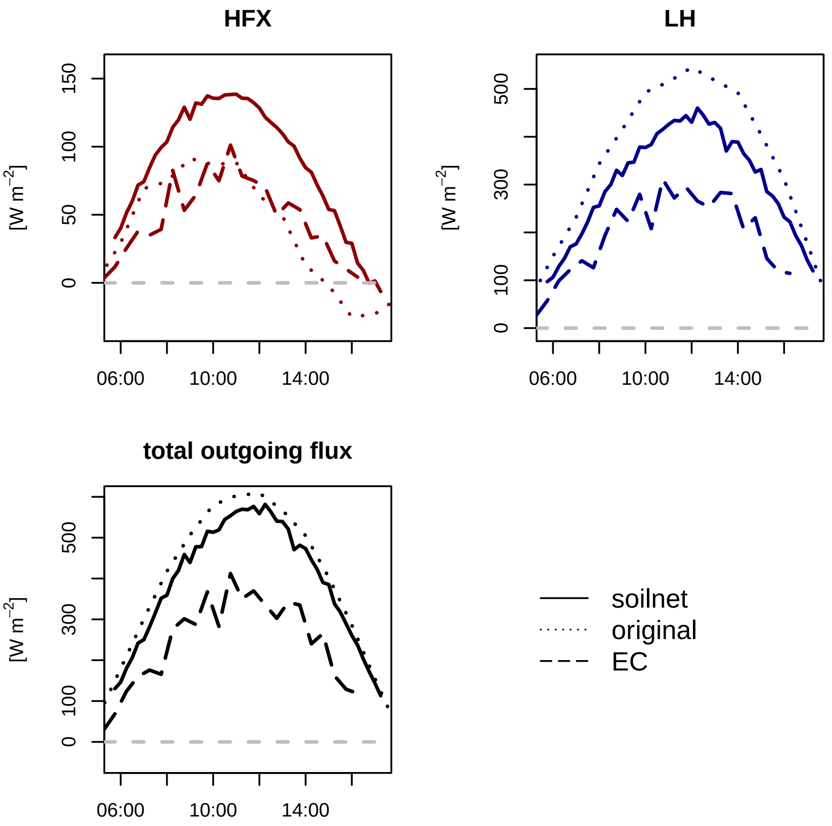

FIGURE 5.17: Temporal development of sensible heat flux (top left), latent heat flux (top right) and total (LH plus HFX) flux (bottom) for the unchanged model run, the run with *soilnet* information and the EC-station

When only considering the HFX, the model without *soilnet* information appears to be closer to the measurement, while the *soilnet* model overestimates the measured values by about 50%. The latent heat flux is overestimated by both models, with the *soilnet* run being closer to the measurements. The total flux shows the reason for the imbalances: Both model runs have similar total fluxes, with different shares in latent and sensible flux that have their origin in the different soil properties. Higher soil temperature and lower moisture result in a higher share of the sensible heat flux. The sum of the modeled fluxes represents exactly the net radiation from Figure 5.16, while the total flux in the measurement stays well below the available energy. This shows that the energy balance of the EC-station is, as expected, not closed for the evaluated time (see Figure 5.18). During the available 24 time steps, only 58% of the incoming net radiation is measured as turbulent fluxes. This EBC lies below the long-term mean for the summer months of 70% (Soltani et al., 2017), caused probably by the low average wind speeds during that day and the resulting, very slow moving TOS found by other studies (Kanda et al., 2004; Inagaki et al., 2006).

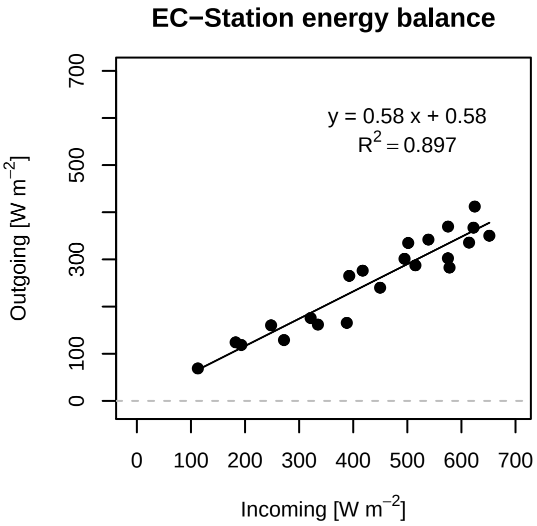

FIGURE 5.18: Energy balance closure of the EC-station for the evaluated time.

The unclosed energy balance limits the possibility of a comparison of measurements with the model, but the available data can still be used to see if the model with *soilnet* information gives a better representation of the fluxes than the model with the original soil data: If the errors in the measurements of LH and HFX are of a similar magnitude (Foken, 2008), the ratio of both (Bowen ratio) can be used as a measure of validity. To see if the errors are equal in LH and HFX, one can use the same form of a scatterplot as in Figure 5.18, but with the *Noah* LSM fluxes on the x-axis as the available energy (keep in mind that *Noah* LSM is energy conserving) and the EC measurements as comparison on the y-axis. If regression lines for the compartments (HFX, LH and total flux) are similar, the error in both is equal, if they differ, the errors are different. This is done in Figure 5.19. The comparison for the *soilnet* model (left side) shows similar slopes and offsets for energy balances in all three compartments. Those for the original model are different: The slopes between HFX and LH differ by 0.04 and the offset even changes sign.

Under such conditions, the model run whose Bowen ratio is equal to that of the measurement does a better job in distributing the fluxes. This is shown in Figure 5.20. *Soilnet* model and measurements agree very well during two thirds of the observed time, while the original model deviates due to its higher LH. On the basis of this figure, the *soilnet* model is shown to better represent the actual fluxes than the original model.

This concludes the comparison of modeled and measured fluxes. It was shown that the model with the updated soil information gives a better representation of the fluxes measured at the EC-station than the original model. Accordingly, the next sections will focus on the model run with *soilnet* data. The fact of the unclosed energy balance limits any further evaluation, as the usual way of taking measurements as the truth and validate model results against them can not be done here. Still, there is a lot more information in the model data than in the measurements, coming from the spatial resolution in the horizontal and the vertical.

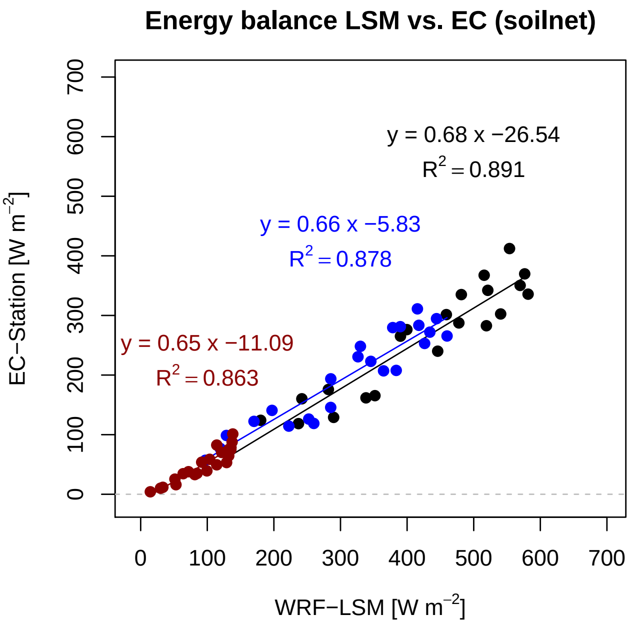

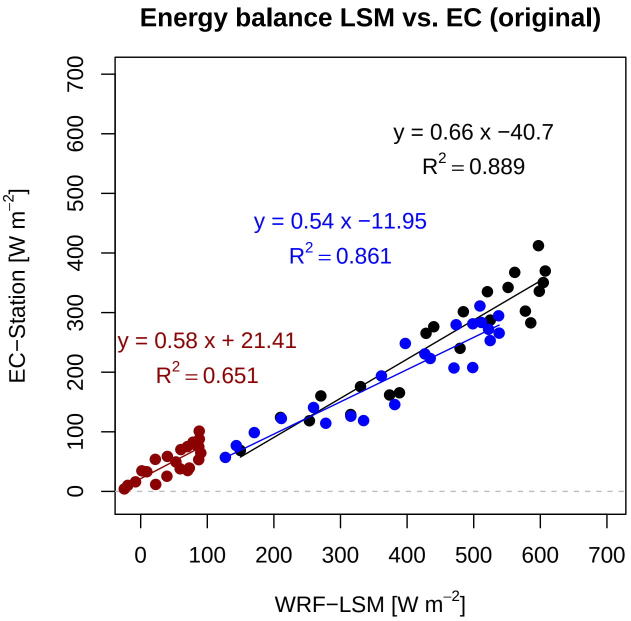

FIGURE 5.19: Energy balance between model (top: *soilnet* model, bottom: original model) and measurement. HFX is red, LH is blue and the sum of both (or total flux) is black. Data is linearly interpolated to the EC-station time steps.

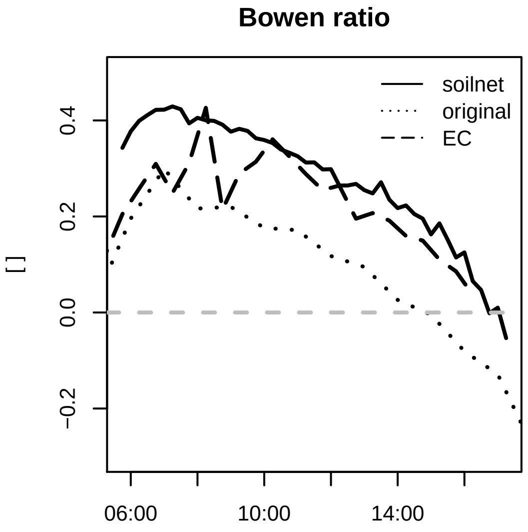

FIGURE 5.20: Bowen ratio (ratio of HFX to LH) of both models and the EC-station.

5.4.2 Comparison of LSM fluxes with LES fluxes

The second part of the evaluation applies the approach shown by Kanda et al. (2004) to compare the turbulent fluxes from the atmospheric part of the model with a 'truth'. This truth, or the real fluxes, will here be derived from the *Noah* LSM fluxes, averaged horizontally over the 30 grid points. It will be compared to the LES fluxes from single grid points, recreating the point measurement of a EC-station, and to horizontally averaged LES fluxes to derive information about the development of turbulent fluxes with height and the influence of the SGS part.

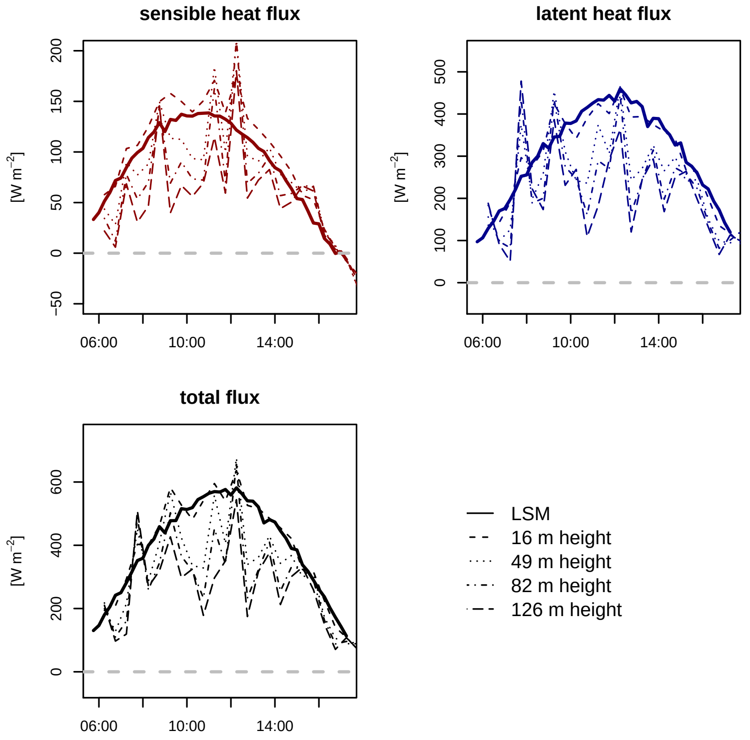

FIGURE 5.21: Temporal course of the LES fluxes compared to the LSM flux in different heights. Heights are given in approximate meters above ground.

A first overview over the horizontally averaged LES fluxes is given in Figure 5.21. Shown are the spatially averaged fluxes from the *Noah* LSM as a reference and the LES fluxes (sum of resolved and SGS) in four selected heights. A first glance shows that the LES fluxes exhibit a much larger temporal variability than the LSM fluxes. Single data points show a doubling or halving of the values. Comparing these spikes between LH and HFX can hint to the cause: if both time series are affected, the reason is to be expected in the values of the vertical wind, as it enters the calculation of both covariances. If the spike occurs only in one flux, the case lies most likely in the moisture or potential temperature data. When overlapping the graphs (not shown) it becomes apparent that the spikes occur at the same time and have therefore to be caused by the vertical wind speed.

Comparing the graphs for the LES fluxes in different heights allows several insights: First, flux magnitudes decrease with height. While LSM flux and LES flux from the lowest evaluated levels match very well in their magnitudes, only 70% of the flux in the lowest level can be found in the height of ≈126 m. This is in accordance with the findings of other studies (e.g. Schalkwijk, Jonker, and Siebesma, 2016) and shows that the energy balance is not closed in greater heights. While the shape of the curves of LSM flux and LES flux in the lowest level match quite well in their temporal course and their variability, the shape varies a lot more in the data points from higher up and the variability increases. The reason for this lies in the SGS part of the fluxes. It is high lower down and shows, when plotted by itself, a very low variability and a diurnal cycle similar to that of the LSM fluxes. With decreasing influence of the SGS part, the strong temporal variability of the resolved part becomes increasingly apparent. Averaged percentages of the SGS flux to the total for the four displayed heights are 66, 17, 6 and 3%, respectively. Accordingly, the topmost level, which is level 12 in the model, is the one where the criterion of SGS fluxes being below 5% of the total fluxes (Steinfeld et al., 2007) is fulfilled.

When the variability is caused, as explained above, by the vertical wind speed, a very probable cause are the TOS that lead to a non-zero average of the vertical wind speed. As the values shown in Figure 5.21 are spatial averages over a surface of 150 by 180 m, this also means that the TOS responsible for the spike has to have a larger diameter than that, otherwise the spikes would be averaged out. Longer temporal averages are another way of ensuring that TOS do not influence the measurements (Mauder and Foken, 2006). When displaying the fluxes for 1 hour averaging periods, most of the spikes become smaller while others are still present. The TOS responsible for the unclosed energy balance are therefore larger than the observed surface and sometimes have a periodicity of over one hour, meaning that even an hour of averaging time is not enough to capture all eddys during the simulated day.

Another observation concerning Figure 5.21 is that in the lowest evaluated level, the HFX in the LES fluxes is higher than the LSM flux on the same surface (average of 6 W m^{-2}). Simultaneously, LH is on average 21 W m^{-2} lower in the LES fluxes than in LSM. This is substantiated by Figure 5.22 where the accumulated fluxes are shown for the same time period. LES sensible heat fluxes in the lowest level accumulate to a surplus of 595 kJ m^{-2}, while LH shows a deficit of 246 kJ m^{-2}. In total, the differences add up to

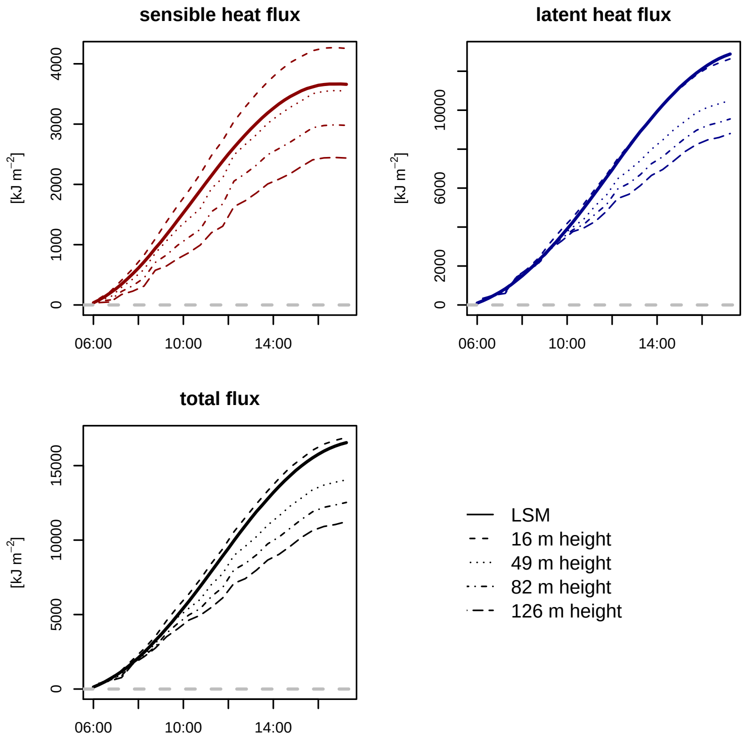

FIGURE 5.22: Temporal course of accumulated LES fluxes in different heights. Heights are given in approximate meters above ground. Averaged fluxes are multiplied by the averaging time.

a overestimation in the LES fluxes of 350 kJ m^{-2}. A reason for the different distribution of fluxes has not been identified; the small difference in the total flux is expected to be a consequence of the different time steps and periods, over which LSM and LES fluxes are calculated and averaged. Due to the energy conserving nature of the model, there can not be a energy surplus or a deficit over the whole domain and model run. Figure 5.22 also again shows the decrease of observed energy with height and worse EBC ratios.

TABLE 5.1: Regression parameters for Figure 5.23

Location	**16 m height**	**49 m height**	**82 m height**	**126 m height**
NW	$1.01x + 18.8$	$0.81x + 65.81$	$0.63x + 107.1$	$0.52x + 133.26$
NE	$0.99x - 3.35$	$0.71x + 13.27$	$0.52x + 36.29$	$0.41x + 38.47$
SW	$1.07x - 9.54$	$0.9x - 9.78$	$0.78x - 0.84$	$0.65x + 30.6$
SE	$1.01x - 10.71$	$0.77x - 6.58$	$0.62x + 28.22$	$0.57x + 22.12$
center	$0.98x + 16.1$	$0.74x + 49.45$	$0.64x + 55.56$	$0.55x + 61.03$
average	$1.02x - 0.26$	$0.81x + 14.4$	$0.66x + 35.37$	$0.54x + 51.06$

Figure 5.23 contains scatterplots for the EBC for several selected grid points

and heights, with the parameters of the regression lines shown in Table 5.1. The grid points lie in the four corners of the evaluated area (c.f. Figure 4.11) and close to the EC-station. The last plot shows the horizontal average of all grid points. The selected heights are the same as above, with the lowest being the lowest evaluated model level and the highest being the one where the SGS part of the fluxes falls below 5%. The true flux is taken as the spatially averaged flux from the LSM. All locations show a decreasing EBC with increasing height. At the same time, the spread in the data points increases, meaning a stronger heterogeneity in the EBC between different time steps. In the lowest level, the energy balance is closed, in some cases even over-closed, apparent as slopes >1. Possible reasons are advection or slight numerical errors caused by the different time resolutions and the temporal interpolation process.

The spatial differences are small near the ground and increase with height. In 49 m height the EBC varies between 71 and 90% with a mean of 81%. In 126 m, it is between 41 and 65%, with a mean of 54%. This shows that in that height where the influence of the SGS model is insignificant, the LES flux calculation does not show better values than the EC-station (c.f. Figure 5.18). Yet, if measured data for the same height would be available, it would be expected to have a lower EBC than in 3.5 m height. The increasing positive offset in the slopes of the EBC regression lines can be interpreted such that the EC-method especially fails to capture small fluxes. Another interpretation is that, if those time steps responsible for the offset occur later during the day, the turbulence in the mixed layer is still driving fluxes while a stable layering is already developing closer to the ground. Such cases can be observed during sunrise and sunset, where the maximum values of the flux occur in heights of 150 and 250 m, respectively, while the flux near the ground is clearly lower. The occurrence during sunrise disappears under a longer averaging period of 60 minutes, while the case during sunset is apparent even then.

It was shown by Mauder and Foken (2006) that longer averaging periods lead to a higher EBC, because then even the largest eddys or TOS have enough time to pass by the point of measurement and their vertical wind speed contributes to the average that is then subtracted from the instantaneous values to get the turbulent fluctuations. Accordingly, the longer the averaging period, the closer the average of the vertical wind speed is supposed to be to 0 m s^{-1}. The effect of longer averaging times on the presented model data is shown in Figure 5.24. Here, moving averages of the vertical wind speed over periods of 30 minutes, 1 hour and 2 hours are shown. The moving average acts as a kind of low-pass filter, retaining only the low frequency changes in the vertical wind speed. It is apparent that in all averaging times, the mean vertical wind speed clearly deviates from 0 m s^{-1}. The magnitude of the deviations decreases with longer periods: For 30 minutes, upwards motions reach up to 1 m s^{-1}, the maxima for 1 hour and 2 hours lie at 0.6 and 0.3 m s^{-1}, respectively. It has therefore to be concluded that even an averaging time of 2 hours is, under the simulated conditions, not enough to include the effect of the largest TOS for flux calculations.

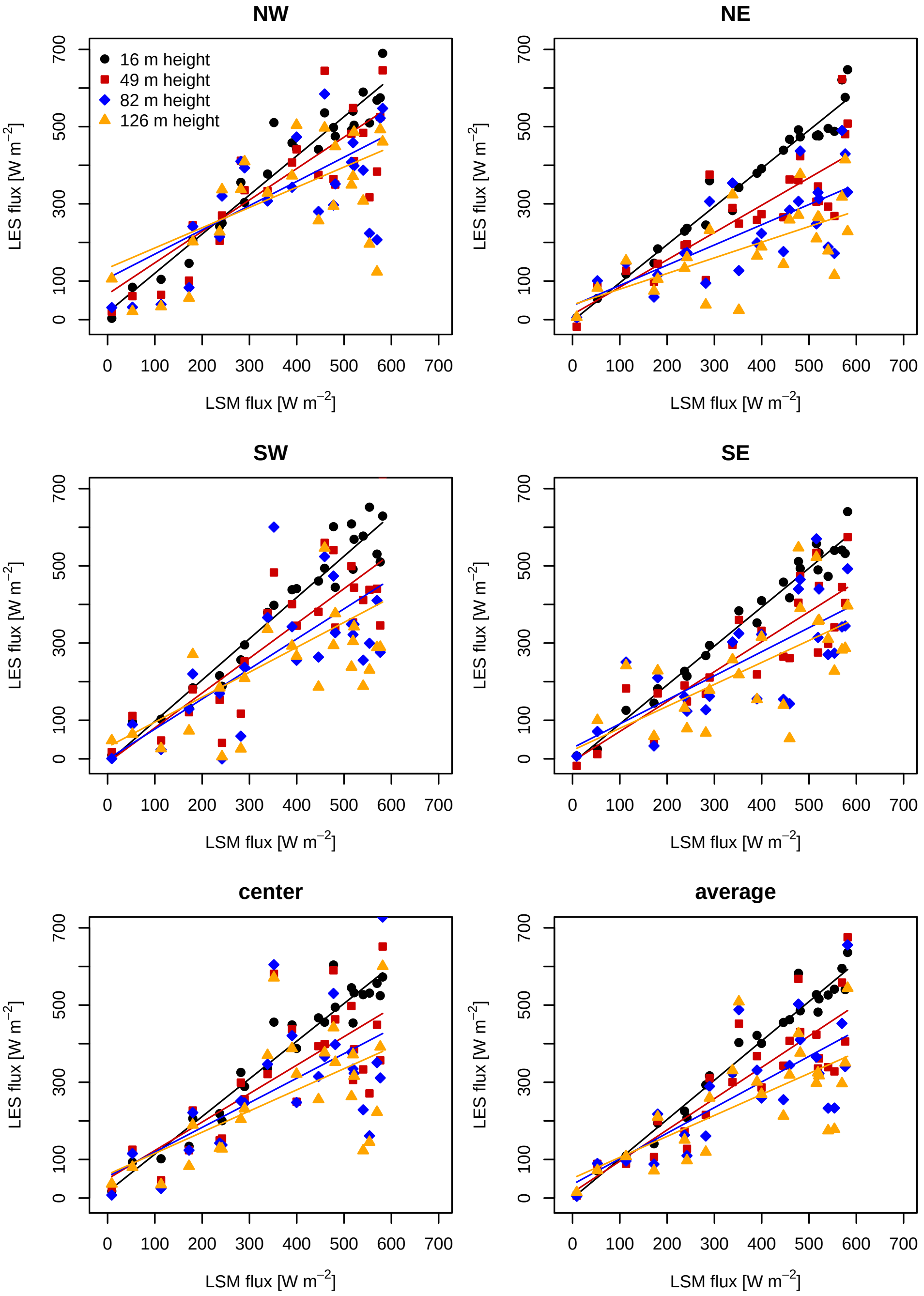

FIGURE 5.23: EBC of several grid points and heights. NW is the northwestern grid point, etc. "center" is one very close to the EC-station. "average" is a horizontal spatial mean over all 30 grid points. Regression parameters see Table 5.1.

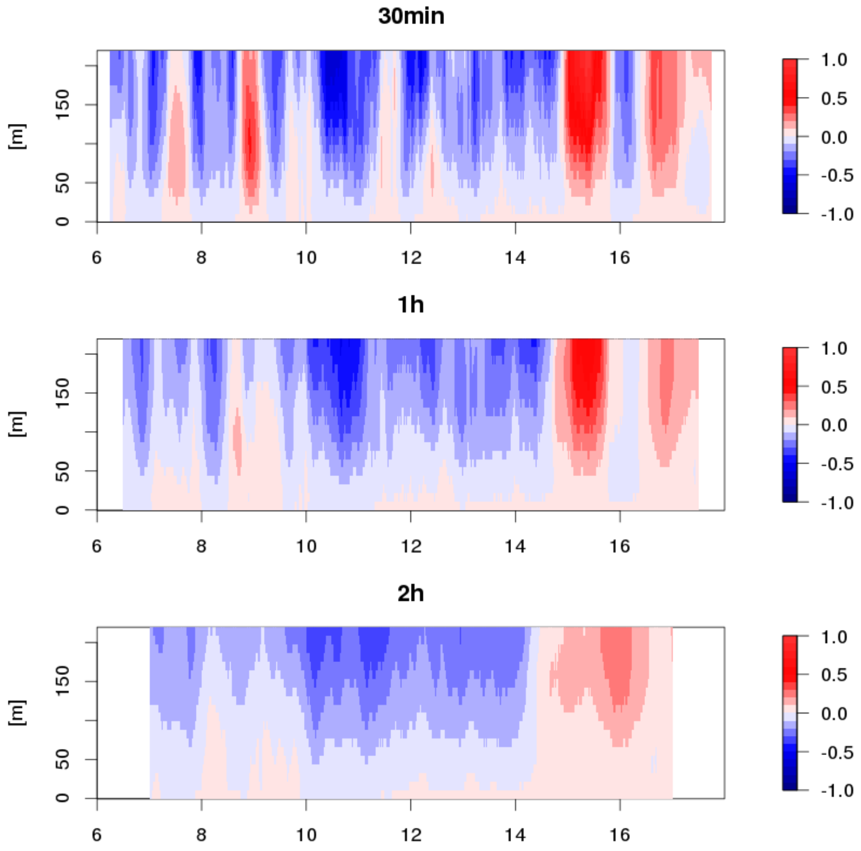

FIGURE 5.24: Moving averages of the vertical wind speed (30 minutes, 1 hour and 2 hours). Wind speed is given in m s^{-1}. Data averaged over the 30 grid points.

5.4.3 Spatial evaluation of the LES fluxes

Up to this point, the fluxes originating from *Noah* LSM were averaged over all 30 observed grid points and taken as the true flux. Yet, from the description of the model setup in Section 4.7 it becomes clear that the ground properties here are not homogeneous, but there are clear gradients present in both soil temperature and soil moisture. It is expected that this has an effect on the fluxes measured above. The hypothesis is that the pattern from soil temperature and moisture can be seen in the fluxes as well, up to a height where turbulent motions mix the air in such a way that the clear properties of the surface disappear. This height is called the blending height (Brutsaert, 1998).

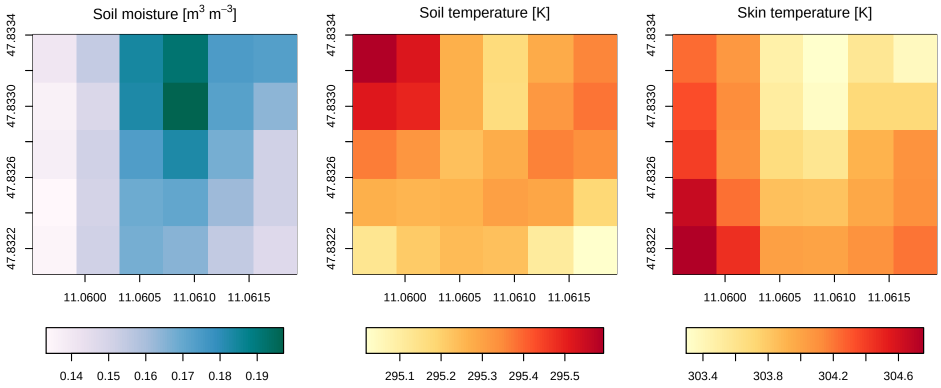

FIGURE 5.25: Temporally averaged patterns of soil moisture, soil temperature and skin temperature.

Soil temperature and soil moisture were specified as initial conditions at the simulation starting time of 15 July 2015 0000 UTC. During the 24 hours of model time, this data was not updated but left to develop freely under the simulated conditions. The soil moisture only showed marginal changes; values in all grid points declined by a constant 2.5% per grid point in the top layer. The original pattern stayed the same. Lower soil levels had constant values. The soil temperature showed small changes until sunrise (–2 K), when the temperature in the top layer started to increase. Maximum temperatures (+5 K) are reached at 1600 UTC. The spatial pattern is constant until 1200 UTC and then slowly changes towards being an inverse mirror image of the soil moisture pattern. The skin temperature, as the third possible driving force of the latent and sensible heat fluxes, shows the largest amplitude during the simulated day. The spatial pattern is connected to that of the soil moisture as well, with high temperatures where soil moisture is low and vice versa. Since this evaluation shows that the change in the spatial pattern is only marginal, the following part of the evaluation will treat temporally averaged fluxes and soil properties.

The temporally averaged patterns of soil moisture, temperature and skin temperature are shown in Figure 5.25. A visual inspection already shows the inverse relationship between soil moisture and skin temperature. The averaged soil temperature pattern is a variation of the initial pattern (correlation of 0.88). These patterns can easily be compared to those of the temporally averaged fluxes. Latent heat fluxes from *Noah* LSM and from the LES in two different heights are shown in Figure 5.26. The LES heights are the lowest evaluated level and where the SGS fluxes drop below 5% of the total fluxes. LH from the LSM clearly represents the soil moisture pattern and is inversely related to the skin temperature. There is no connection to the soil temperature. LES fluxes in both shown heights are very similar to each other (correlation of 0.89), but very different from the LSM fluxes. Correlation of the lower level with soil moisture, temperature and skin temperature are –0.29, 0.47 and 0.39, respectively. From a physical point of view, the latent heat flux is expected to be positively related to the soil moisture and negatively with the skin and soil temperature. This is not the case here, and the soil properties can not adequately explain the pattern in the latent heat flux of the LES. The high LH values in the northwestern area are also not explainable by advection, as there is no patch of high soil moisture in the close vicinity.

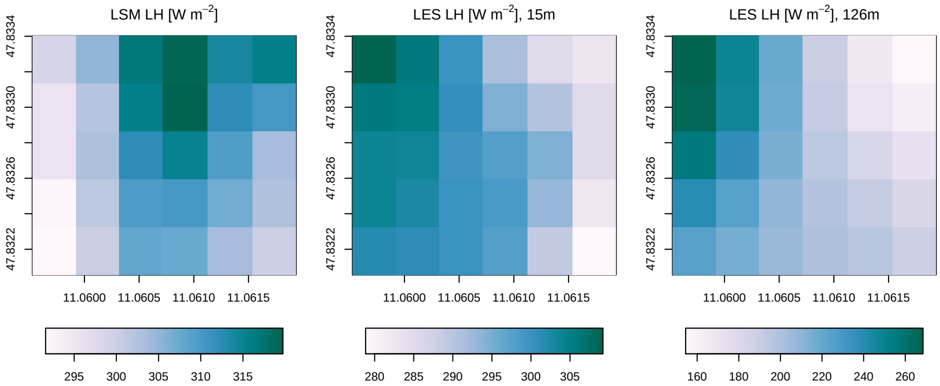

FIGURE 5.26: Temporally averaged patterns of latent heat fluxes from *Noah* LSM and from LES in two heights.

Temporally averaged heat fluxes are given in Figure 5.27. The HFX from the LSM is strongly correlated with the skin temperature (0.93) and negatively correlated with the soil moisture (–0.99). This is a mathematical requirement, as the incoming radiation is distributed into latent and sensible heat fluxes depending on the soil moisture. LES flux from the lowest level shows similar correlations (0.81 and –0.88), the soil pattern is represented in the flux pattern. Correlations of LES fluxes from the 12th level with the ground are clearly lower, while still having the same sign (0.52 and –0.53).

When comparing to Figure 5.26, the similarity to the patterns of LH from LES becomes apparent: the correlation between LH and HFX from the 12th model level is at 0.85.

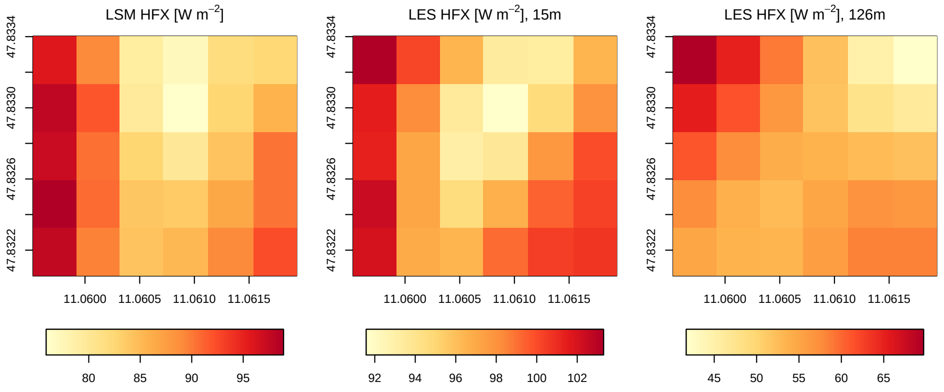

FIGURE 5.27: Temporally averaged patterns of sensible heat fluxes from *Noah* LSM and from LES in two heights.

The evaluation above shows that fluxes from the *Noah* LSM are strongly dependent on the soil moisture and, not quite as pronounced, on the skin temperature. This is valid for both latent and sensible heat flux. LES fluxes behave differently: The HFX, at least in low heights, is also dependent on soil moisture and skin temperature, but the LH shows no connection to the soil properties in any height. LH seems to be more self-similar with height, as the pattern in 126 m height is close to the one near the ground, while HFX is more variable. In larger heights, a connection between LH and HFX becomes apparent.

If the method of correlating spatial patterns is extended to comparing the LES fluxes in different heights, a simple concept for the determination of the blending height can be constructed. This can be done in two ways: (1) the comparison of LES fluxes with the soil properties or the LSM fluxes that showed the largest correlation above or (2) the comparison of LES fluxes of various heights with the LES flux from the lowest evaluated level. The first option is valid for the LES HFX that was shown to have good agreement with the soil, while the second option is better suited for the LES LH that did not show clear connection to the ground. Both approaches are shown in Figure 5.28, with additional level-by-level correlations of LES LH and HFX. The left frame shows the correlation of the LES HFX in different levels with the soil moisture and with the LES HFX in the lowest evaluated level. Both graphs are almost mirror images of themselves, which is to be expected, because the soil moisture was shown to be inversely correlated with the HFX above, while there is a positive correlation of the HFX in the lowest level with the levels above. Yet, the Figure also shows that the positive correlation in the LES fluxes quickly declines with height and drops to 0.66 in level 5, where it stays constant for up to level 9 where correlations decrease again. If a lower limit of 0.5 is set as the blending height, then this height is at ≈140 m above ground. A lower limit of 0.7, where one can speak of a reasonable correlation, is reached already in level 4 or about 45 m above ground.

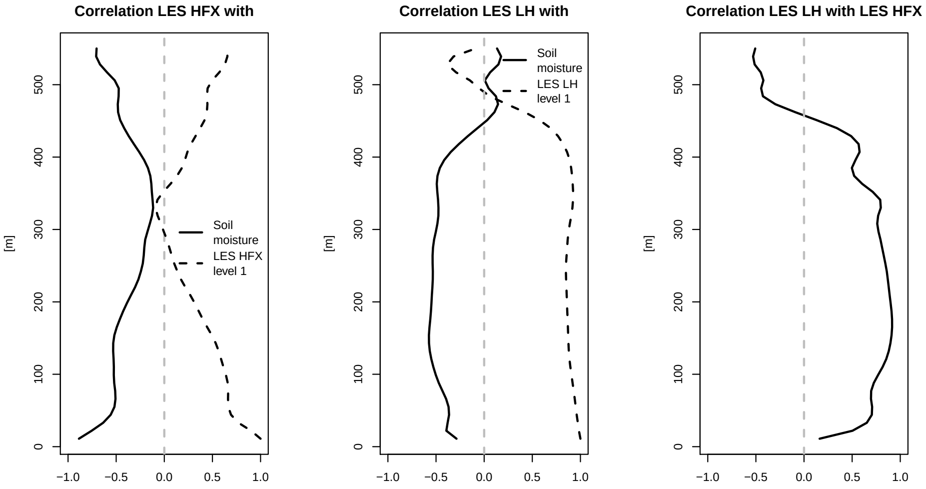

FIGURE 5.28: Correlations of flux and soil property pattern in different heights.

The center frame compares the LES LH with the soil moisture and lowest LES LH pattern. The correlation with the soil moisture is constantly low up to a height of 450 m, and accordingly the correlations of the LH with the lowest level are constant as well. These correlations are high and drop below 0.7 only in 440 m above ground. According to this, the LH has a low connection to the ground properties, but the pattern of the flux is very constant with height. The frame on the right correlates the LES HFX with the LES LH in their respective levels. Apart from the lowest heights, the turbulent latent and sensible heat fluxes are very similar to each other up to where ground and LH lose connection (see center frame). In the lowest levels, the similarity of HFX with the ground properties predominates. According to these findings, blending heights have to be determined separately for HFX and LH.

Chapter 6

Summary

Large eddy simulations are an important tool for studying the atmospheric boundary layer and the turbulent movement of air within. WRF-LES in particular allows for an easy implementation of realistic conditions and the representation of a multitude of physical processes in the model.

The simulations for the *Fendt* area, set up in a computationally efficient way, and the comparison with the Lidar data taken from the state-of-the-art *VirtualTower* measurements, allow the formulations of answers for the questions raised in the Introduction.

Is the LES capable of representing a real period over a real and well- known area?

The evaluation showed that the LES, despite its single domain setup, is able to produce patterns in the boundary layer flows as they are known from more idealized setup published in the literature. Depending on the wind speed, either cell-like or roll-like turbulent features develop in the domain. Spectra showed that the turbulence follows the theory of atmospheric turbulence: Production range, inertial subrange and dissipation range are present. These properties are best simulated during daytime with moderate or no horizontal winds. For resolving the turbulence during stable layering at night the grid resolution is too coarse. WRF-LES has the shortcoming of not transferring information about turbulence over domain borders, which is why areas of under-developed turbulence are created at the inflow edge. Turbulence spectra taken at several grid points across the domain showed that this shortcoming can be mitigated by limiting the evaluated area to such grid points that have fully developed turbulence.

Can vertically resolved measurements of wind speed, taken from a virtual tower constructed with Lidar devices, be used to evaluate the model output?

The *VirtualTower* measurements are innovative due to their combination of three wind Lidar devices that allow for a wind measurement in all three directions and with a high temporal and especially vertical resolution. The comparison of this data with the simulated wind field showed, in the largest part, good agreement: General wind directions and their speeds match well, the timing of changes in direction or speed can be simulated by the model. Both model and simulation show a similar development of nocturnal and daytime boundary layers. The quality of the simulated conditions is limited by the boundary condition data. Measured low-level jets were present in the simulations, but their timing, strength and vertical extent were missed. This is due to the fact that boundary conditions are loaded only once every six hours. Short events like the low-level jet can not properly be represented in such data. Higher resolution boundary conditions are therefore a promising way of improving the results.

It was shown with the example of temporarily increased wind speeds during night that the model is able to reproduce weather phenomena that originate within the domain. In contrast to measurements, which in this case only showed the increase in wind speed, the model data is a four-dimensional representation of the conditions within the domain. It can be used to investigate the origin of micro-meteorological events; in this case it was shown that the higher wind speeds were caused by a katabatic flow from the nearby ridge that passes the location of the *VirtualTower* during the early morning hours.

Despite the small domain and boundary conditions that are directly derived from a very large scale reanalysis products, the model was able to represent many weather phenomena from the micro- to the macroscale: Examples are the katabatic flow, the low-level jets and the alpine pumping. It can not be ruled out that there are phenomena which are missed, but if either the origin or the effect are in the domain itself or the boundary condition, then the phenomenon will be represented.

Can the simulation of realistic conditions successfully recreate the fluxes of latent and sensible heat?

Compared to the model run with standard soil information, the model that used the *soilnet* measurements as initial conditions showed a better agreement with the measurements. This was shown using the fluxes calculated by the land-surface model: The distribution of the total flux in a sensible and a latent part closely follows the measured ratio. Further comparisons of the model data with measurements is limited by the typically unclosed energy balance in EC-station measurements: not all turbulent fluxes are measured. This means that a model evaluation can not use measurements, since the error in the measurements is not known. Further evaluation therefore took the fluxes of the LSM, which is energy conserving, as the true fluxes. Compared to these, the LES fluxes, calculated by using the EC-method, were in general smaller and much more variable. Fluxes decline with height, as it is described in literature.

Which additional benefit has the spatially highly resolved representation of fluxes over point measurements or spatially averaged energy balances?

The high spatial resolution of the LES makes it possible to evaluate spatial differences in the fluxes. EC-stations can only measure at one point and integrate the fluxes over the footprint they are experiencing at the moment. In the model, it is possible to put an imaginary EC-station at every point in horizontal and vertical space and compare. This evaluation showed that latent and sensible heat fluxes depend mostly on the soil moisture and the skin temperature, while the soil temperature has no real impact. The largest connection between fluxes and the soil properties exists in the sensible heat flux, which also changes most quickly with height. Latent heat fluxes show a smaller connection to the soil properties, but are more constant with height. This implies that different blending height concepts might be necessary for latent and sensible heat fluxes.

6.1 Recommendations

The presented single domain modeling approach has two advantages: the setup is comparatively easy and the required computing time is about one order of magnitude lower than comparable nested setups. This makes it possible to set up such an experiment for many different areas and periods and allows for small ensembles of simulations.

Care has to be taken during the setup concerning the used elevation model: Steep slopes in combination with the terrain-following coordinates in WRF promote model errors. The smoothing routines implemented in WPS can mitigate this, an alternative is the removal of single steep areas by hand. This way, working setups for even more complex terrains should be achievable.

Still, the setup of such an LES has to be described as a process of trial and error. There is an enormous number of combinations of domain position, domain size, horizontal resolution, vertical resolution, temporal resolution and weather conditions, but each of these alone can be the cause for a model failure. Yet, changes in one of these parameters can also solve the problems and have to be done for only one domain with the described setup.

The setup can still be improved: Most promising are boundary conditions with a higher temporal and spatial resolution. Such data ensures that the timings and extents of meso- to macroscale phenomena are properly represented. The data can either come from other sources or from a downscaling with WRF itself. Downscaling with WRF would combine the precision of a nested model with the shorter computation time.

With vertical nesting, the setup could be extended with smaller areas of special focus with higher resolution. Applying this to the whole lower area of the domain would allow for the simulation of turbulence in the stable boundary layer, or the resolution could be refined around certain spaces like a measurement system. In the presented case, a higher resolution around the EC-station would have made it possible to include the complete variability shown by the *soilnet* measurements and to compare model data with the original EC-station measurements in 3.5 m height.

6.2 Outlook

The presented approach to modeling a small real area with very high resolution in a computationally efficient way could be used in two ways:

The first is the detailed simulation of meteorological conditions in a known area. Boundary layer flows are influenced by the surface characteristics. Mountains, valleys, buildings and vegetation all influence the speed and direction of the wind and therefore also the temperature, humidity etc. A four dimensional representation of the flow can be a valuable resource for the planning of future land use changes and constructions. Cities are known for their local temperature increase, which will in future be intensified by climate change. Preserving or creating channels for fresh air will become increasingly important. A LES for such an area can help in identifying such channels and ensure that they are not closed off or re-opened. Similarly, the data can be used to find new possible industrial areas from which the exhaust air will not negatively influence nearby residential areas. Airports can be made safer by identifying hot-spots of vertical motions.

Secondly, the flux evaluation on such small scales can be upscaled to improve large scale modeling. Climate models are, in principle, energy balance models, where the influence of the parts of the climate system on the energy fluxes are represented as well as it is possible, limited by the knowledge of certain processes and the model resolution. Studies for a small but well-known area can help to improve the understanding of the connection between soil properties, the vegetation and the incoming radiation on the turbulent fluxes. This knowledge can in turn then be used to improve the parameterizations in climate models that are responsible for the energy exchange between the ground and the atmosphere.

Both ideas are supported by the historical and future increase in computing power. Increasing computing power means shorter computing times, which in turn provides more resources for more simulations, covering larger or different areas, or the same area over a longer time or over different periods. A sophisticated choice of locations and periods can lead to a data set that covers almost all possible meteorological conditions.

Appendix A

Index file for 1-arc-second DEM data

```
type = continuous
signed = yes
projection = regular_ll
dx = 0.0002777
dy = 0.0002777
known_x = 1.0
known_y = 1.0
known_lat = 46.999861111111
known_lon = 9.9998611111111
wordsize = 2
tile_x = 7201
tile_y = 7201
tile_z = 1
units = "meters MSL"
description = "Topography height"
missing_value=-9999
endian = little
row_order = top_bottom
```

`Projection` is the chosen geoid the data is projected on, `dx` and `dy` is the resolution in degree in x and y direction, respectively. `known_y` and `known_lat` give the index number and the latitude of the bottom left corner of the most bottom left grid point, `known_x` and `known_longitude` do the same in y-direction. `tile_x` and `tile_y` give the total amount of grid points available in x and y direction. These can span over several files (which then have to be named accordingly). `missing_value` gives the code for missing values. `units` and `description` are for describing the data.

Appendix B

Namelist files for the 2015 model run

WPS:

```
&share
 wrf_core         = 'ARW',
 max_dom          = 1,
 start_date       = '2015-07-15_00:00:00',
 end_date         = '2015-07-17_00:00:00',
 interval_seconds = 21600,
 io_form_geogrid  = 2,
 debug_level      = 0,
/
&geogrid
 parent_id         =    0,
 parent_grid_ratio =    1,
 i_parent_start    =    1,
 j_parent_start    =    1,
 e_we              =  500,
 e_sn              =  500,
 geog_data_res     =  'landuse_3s+1s_ast',
 dx                = 30,
 dy                = 30,
 map_proj  = 'lambert',
 ref_lat   =  47.823,
 ref_lon   =  11.079,
 truelat1  =  47.823,
 truelat2  =  47.823,
 stand_lon =  11.00,
 geog_data_path = '/pd/modelinput/wrf-terrain/'
/
&ungrib
```

```
 out_format = ’WPS’,
 prefix     = ’FILE’,
/
&metgrid
 fg_name         = ’FILE’
 io_form_metgrid = 2,
/
```

WRF:

```
&time_control
 run_days                            = 0,
 run_hours                           = 48,
 start_year                          = 2015,
 start_month                         = 07,
 start_day                           = 15,
 start_hour                          = 00,
 end_year                            = 2015,
 end_month                           = 07,
 end_day                             = 17,
 end_hour                            = 00,
 interval_seconds                    = 21600,
 input_from_file                     = .true.,
 override_restart_timers             = .true.,
 history_interval_s                  = 900,
 frames_per_outfile                  = 1,
 restart                             = .false.,
 restart_interval                    = 30,
/
&domains
 time_step                           = 0,
 time_step_fract_num                 = 1,
 time_step_fract_den                 = 4,
 max_dom                             = 1,
 e_we                                = 500,
 e_sn                                = 500,
 e_vert                              = 151,
 eta_levels   = 1.000, 0.9973, 0.9946, 0.9919, 0.9891,
                0.9864, 0.9837, 0.981, 0.9783, 0.9756,
                0.9729, 0.9703, 0.9676, 0.9649, 0.9622,
                0.9595, 0.9568, 0.9542, 0.9515, 0.9488,
                0.9462, 0.9435, 0.9408, 0.9382, 0.9355,
                0.9329, 0.9302, 0.9276, 0.9249, 0.9223,
```

```
                0.9196, 0.917, 0.9144, 0.9117, 0.9091,
                0.9065, 0.9038, 0.9012, 0.8986, 0.896,
                0.8934, 0.8907, 0.8881, 0.8855, 0.8829,
                0.8803, 0.8777, 0.8751, 0.8725, 0.8699,
                0.8673, 0.8648, 0.8622, 0.8596, 0.857,
                0.8544, 0.8519, 0.8493, 0.8467, 0.8441,
                0.8416, 0.839, 0.8365, 0.8339, 0.8314,
                0.8288, 0.8263, 0.8237, 0.8212, 0.8186,
                0.8161, 0.8135, 0.811, 0.8085, 0.8059,
                0.8034, 0.8009, 0.7984, 0.7959, 0.7933,
                0.7908, 0.7883, 0.7858, 0.7833, 0.7808,
                0.7783, 0.7758, 0.7733, 0.7708, 0.7683,
                0.7658, 0.7633, 0.7609, 0.7584, 0.7559,
                0.7534, 0.7509, 0.7485, 0.746, 0.7435,
                0.7411, 0.7386, 0.7361, 0.7334, 0.7306,
                0.7276, 0.7245, 0.7211, 0.7175, 0.7136,
                0.7094, 0.7048, 0.6998, 0.6943, 0.6883,
                0.6816, 0.6742, 0.666, 0.6571, 0.6472,
                0.6363, 0.6244, 0.6115, 0.5974, 0.5823,
                0.566, 0.5487, 0.5304, 0.511, 0.4908,
                0.4698, 0.448, 0.4256, 0.4027, 0.3794,
                0.3557, 0.3317, 0.3075, 0.2833, 0.259,
                0.2347, 0.2104, 0.1863, 0.1623, 0.1384,
                0.1147, 0.0913, 0.0681, 0.0451, 0.0224,
                0.000,
p_top_requested                     = 50000,
num_metgrid_levels                  = 38,
num_metgrid_soil_levels             = 4,
dx                                  = 30,
dy                                  = 30,
grid_id                             = 1,
parent_id                           = 0,
i_parent_start                      = 1,
j_parent_start                      = 1,
parent_grid_ratio                   = 1,
parent_time_step_ratio              = 1,
feedback                            = 0,
smooth_option                       = 0,
use_adaptive_time_step              = .true.,
step_to_output_time                 = .true.,
target_cfl                          = 0.9,
target_hcfl                         = 0.84,
```

```
 max_step_increase_pct                = 51,
 starting_time_step                   = 1,
 starting_time_step_den               = 8,
 max_time_step                        = 1,
 max_time_step_den                    = 4,
 min_time_step                        = 1,
 min_time_step_den                    = 16,
 adaptation_domain                    = 1,
 max_ts_level                         = 150,
 max_ts_locs                          = 40,
/
&physics
 mp_physics                           = 4,
 ra_lw_physics                        = 4,
 ra_sw_physics                        = 4,
 radt                                 = 4,
 sf_sfclay_physics                    = 2,
 sf_surface_physics                   = 2,
 bl_pbl_physics                       = 0,
 bldt                                 = 0,
 cu_physics                           = 0,
 cudt                                 = 0,
 isfflx                               = 1,
 ifsnow                               = 0,
 icloud                               = 1,
 num_soil_layers                      = 4,
 sf_urban_physics                     = 0,
 num_land_cat                         = 28,
 topo_wind                            = 0,
/
&dynamics
 w_damping                            = 1,
 diff_opt                             = 2,
 km_opt                               = 2,
 diff_6th_opt                         = 2,
 diff_6th_factor                      = 0.3,
 base_temp                            = 290.
 damp_opt                             = 3,
 zdamp                                = 500.,
 dampcoef                             = 0.2,
 khdif                                = 0,
 kvdif                                = 0,
```

```
 non_hydrostatic                            = .true.,
 moist_adv_opt                              = 1,
 scalar_adv_opt                             = 1,
 mix_full_fields                            = .true.,
 mix_isotropic                              = 1,
 mix_upper_bound                            = 0.1,
 time_step_sound                            = 8,
 sfs_opt                                    = 2,
 epssm                                      = 0.3,
/
&bdy_control
 spec_bdy_width                             = 15,
 spec_zone                                  = 1,
 relax_zone                                 = 14,
 specified                                  = .true.,
 nested                                     = .false.,
/
```

Appendix C

Namelist files for the 2016 model run

WPS:

```
&share
 wrf_core         = 'ARW',
 max_dom          = 1,
 start_date       = '2016-07-06_00:00:00',
 end_date         = '2016-07-08_00:00:00',
 interval_seconds = 21600,
 io_form_geogrid  = 2,
 debug_level      = 0,
/
&geogrid
 parent_id         =   0,
 parent_grid_ratio =   1,
 i_parent_start    =   1,
 j_parent_start    =   1,
 e_we              = 500,
 e_sn              = 500,
 geog_data_res     = 'landuse_3s+1s_ast',
 dx                = 30,
 dy                = 30,
 map_proj  = 'lambert',
 ref_lat   =  47.823,
 ref_lon   =  11.079,
 truelat1  =  47.823,
 truelat2  =  47.823,
 stand_lon =  11.00,
 geog_data_path = '/pd/modelinput/wrf-terrain/'
/
&ungrib
```

```
 out_format = 'WPS',
 prefix     = 'FILE',
/
&metgrid
 fg_name         = 'FILE'
 io_form_metgrid = 2,
/
```

WRF:

```
&time_control
 run_days                            = 0,
 run_hours                           = 48,
 start_year                          = 2016,
 start_month                         = 07,
 start_day                           = 06,
 start_hour                          = 00,
 end_year                            = 2016,
 end_month                           = 07,
 end_day                             = 08,
 end_hour                            = 00,
 interval_seconds                    = 21600,
 input_from_file                     = .true.,
 override_restart_timers             = .true.,
 history_interval_s                  = 900,
 frames_per_outfile                  = 1,
 restart                             = .false.,
 restart_interval                    = 30,
/
&domains
 time_step                           = 0,
 time_step_fract_num                 = 1,
 time_step_fract_den                 = 5,
 max_dom                             = 1,
 e_we                                = 500,
 e_sn                                = 500,
 e_vert                              = 151,
 eta_levels   = 1.000, 0.9973, 0.9946, 0.9919, 0.9891,
                0.9864, 0.9837, 0.981, 0.9783, 0.9756,
                0.9729, 0.9703, 0.9676, 0.9649, 0.9622,
                0.9595, 0.9568, 0.9542, 0.9515, 0.9488,
                0.9462, 0.9435, 0.9408, 0.9382, 0.9355,
                0.9329, 0.9302, 0.9276, 0.9249, 0.9223,
```

```
                  0.9196, 0.917, 0.9144, 0.9117, 0.9091,
                  0.9065, 0.9038, 0.9012, 0.8986, 0.896,
                  0.8934, 0.8907, 0.8881, 0.8855, 0.8829,
                  0.8803, 0.8777, 0.8751, 0.8725, 0.8699,
                  0.8673, 0.8648, 0.8622, 0.8596, 0.857,
                  0.8544, 0.8519, 0.8493, 0.8467, 0.8441,
                  0.8416, 0.839, 0.8365, 0.8339, 0.8314,
                  0.8288, 0.8263, 0.8237, 0.8212, 0.8186,
                  0.8161, 0.8135, 0.811, 0.8085, 0.8059,
                  0.8034, 0.8009, 0.7984, 0.7959, 0.7933,
                  0.7908, 0.7883, 0.7858, 0.7833, 0.7808,
                  0.7783, 0.7758, 0.7733, 0.7708, 0.7683,
                  0.7658, 0.7633, 0.7609, 0.7584, 0.7559,
                  0.7534, 0.7509, 0.7485, 0.746, 0.7435,
                  0.7411, 0.7386, 0.7361, 0.7334, 0.7306,
                  0.7276, 0.7245, 0.7211, 0.7175, 0.7136,
                  0.7094, 0.7048, 0.6998, 0.6943, 0.6883,
                  0.6816, 0.6742, 0.666, 0.6571, 0.6472,
                  0.6363, 0.6244, 0.6115, 0.5974, 0.5823,
                  0.566, 0.5487, 0.5304, 0.511, 0.4908,
                  0.4698, 0.448, 0.4256, 0.4027, 0.3794,
                  0.3557, 0.3317, 0.3075, 0.2833, 0.259,
                  0.2347, 0.2104, 0.1863, 0.1623, 0.1384,
                  0.1147, 0.0913, 0.0681, 0.0451, 0.0224,
                  0.000,
p_top_requested                   = 50000,
num_metgrid_levels                = 38,
num_metgrid_soil_levels           = 4,
dx                                = 30,
dy                                = 30,
grid_id                           = 1,
parent_id                         = 0,
i_parent_start                    = 1,
j_parent_start                    = 1,
parent_grid_ratio                 = 1,
parent_time_step_ratio            = 1,
feedback                          = 0,
use_adaptive_time_step            = .true.,
step_to_output_time               = .true.,
target_cfl                        = 0.9,
target_hcfl                       = 0.84,
max_step_increase_pct             = 51,
```

```
 starting_time_step                   = 1,
 starting_time_step_den               = 10,
 max_time_step                        = 1,
 max_time_step_den                    = 5,
 min_time_step                        = 1,
 min_time_step_den                    = 16,
 adaptation_domain                    = 1,
 max_ts_level                         = 150,
 max_ts_locs                          = 40,
/ &physics
 mp_physics                           = 4,
 ra_lw_physics                        = 4,
 ra_sw_physics                        = 4,
 radt                                 = 4,
 sf_sfclay_physics                    = 2,
 sf_surface_physics                   = 2,
 bl_pbl_physics                       = 0,
 bldt                                 = 0,
 cu_physics                           = 0,
 cudt                                 = 0,
 isfflx                               = 1,
 ifsnow                               = 0,
 icloud                               = 1,
 surface_input_source                 = 1,
 num_soil_layers                      = 4,
 sf_urban_physics                     = 0,
 num_land_cat                         = 28,
 topo_wind                            = 0,
/
&dynamics
 w_damping                            = 1,
 diff_opt                             = 2,
 km_opt                               = 2,
 diff_6th_opt                         = 2,
 diff_6th_factor                      = 0.3,
 base_temp                            = 290.
 damp_opt                             = 3,
 zdamp                                = 500.,
 dampcoef                             = 0.2,
 khdif                                = 0,
 kvdif                                = 0,
 non_hydrostatic                      = .true.,
```

```
 moist_adv_opt                        = 1,
 scalar_adv_opt                       = 1,
 mix_full_fields                      = .true.,
 mix_isotropic                        = 1,
 mix_upper_bound                      = 0.1,
 time_step_sound                      = 8,
 sfs_opt                              = 2,
 epssm                                = 0.3,
/
&bdy_control
 spec_bdy_width                       = 15,
 spec_zone                            = 1,
 relax_zone                           = 14,
 specified                            = .true.,
 nested                               = .false.,
/
```

Bibliography

Aitken, Matthew L et al. (2014). "Large eddy simulation of wind turbine wake dynamics in the stable boundary layer using the Weather Research and Forecasting Model". In: *Journal of Renewable and Sustainable Energy* 6.3, pp. 33–137.

Albertson, John D and Marc B Parlange (1999). "Surface length scales and shear stress: Implications for land-atmosphere interaction over complex terrain". In: *Water Resources Research* 35.7, pp. 2121–2132.

Andren, A (1995). "The structure of stably stratified atmospheric boundary layers: A large-eddy simulation study". In: *Quarterly Journal of the Royal Meteorological Society* 121.525, pp. 961–985.

Andren, A. et al. (1994). "Large-eddy simulation of a neutrally stratified boundary layer: A comparison of four computer codes". In: *Quarterly Journal of the Royal Meteorological Society* 120.520, pp. 1457–1484.

Antonelli, Marta and Richard Rotunno (2007). "Large-eddy simulation of the onset of the sea breeze". In: *Journal of the Atmospheric Sciences* 64.12, pp. 4445–4457.

Arakawa, Akio and Vivian R Lamb (1977). "Computational Design of the Basic Dynamical Processes of the UCLA General Circulation Model". In: *Methods in Computational Physics: Advances in Research and Applications*. Vol. 17. Elsevier, pp. 173–265.

Arthur, Robert S et al. (2019). "Using a Canopy Model Framework to Improve Large-Eddy Simulations of the Neutral Atmospheric Boundary Layer in the Weather Research and Forecasting Model". In: *Monthly Weather Review* 147.1, pp. 31–52.

Aubinet, Marc, Timo Vesala, and Dario Papale (2012). *Eddy covariance: a practical guide to measurement and data analysis*. Springer Science & Business Media.

Avissar, Roni et al. (1998). "An evaluation of the large-eddy simulation option of the regional atmospheric modeling system in simulating a convective boundary layer: a FIFE case study". In: *Journal of the atmospheric sciences* 55.7, pp. 1109–1130.

Bao, Jingyi, Fotini Katopodes Chow, and Katherine A Lundquist (2018). "Large-eddy simulation over complex terrain using an improved immersed boundary method in the Weather Research and Forecasting model". In: *Monthly Weather Review* 146.9, pp. 2781–2797.

Basu, S. and A. Lacser (2017). "A Cautionary Note on the Use of Monin–Obukhov Similarity Theory in Very High-Resolution Large-Eddy Simulations". In: *Boundary-Layer Meteorology* 163.2, pp. 351–355.

Basu, S. and F. Porté-Agel (2006). "Large-eddy simulation of stably stratified atmospheric boundary layer turbulence: a scale-dependent dynamic modeling approach". In: *Journal of the Atmospheric Sciences* 63.8, pp. 2074–2091.

Beare, Robert J. (2008). "The role of shear in the morning transition boundary layer". In: *Boundary-Layer Meteorology* 129.3, pp. 395–410.

Beare, Robert J. et al. (2006). "An intercomparison of large-eddy simulations of the stable boundary layer". In: *Boundary-Layer Meteorology* 118.2, pp. 247–272.

Beck, Christoph (2012). "Are there weekly cycles in occurrence frequencies of large-scale circulation types?" In: *Atmospheric Science Letters* 13.4, pp. 238–243.

Beck, Christoph, Jucundus Jacobeit, and PD Jones (2007). "Frequency and within-type variations of large-scale circulation types and their effects on low-frequency climate variability in central europe since 1780". In: *International Journal of Climatology: A Journal of the Royal Meteorological Society* 27.4, pp. 473–491.

Bogena, Heye R. (2016). "TERENO: German network of terrestrial environmental observatories". In: *Journal of large-scale research facilities JLSRF* 2, p. 52.

Bogena, Heye R. et al. (2010). "Potential of wireless sensor networks for measuring soil water content variability". In: *Vadose Zone Journal* 9.4, pp. 1002–1013.

Botnick, Aaron M and Evgeni Fedorovich (2008). "Large eddy simulation of atmospheric convective boundary layer with realistic environmental forcings". In: *Quality and Reliability of Large-Eddy Simulations*. Springer, pp. 193–204.

Bou-Zeid, Elie, Charles Meneveau, and Marc B. Parlange (Feb. 2004). "Large-eddy simulation of neutral atmospheric boundary layer flow over heterogeneous surfaces: Blending height and effective surface roughness". In: *Water Resources Research* 40.2.

– (2005). "A scale-dependent Lagrangian dynamic model for large eddy simulation of complex turbulent flows". In: *Physics of fluids* 17.2, p. 025105.

Bou-Zeid, Elie et al. (July 2009). "The Effects of Building Representation and Clustering in Large-Eddy Simulations of Flows in Urban Canopies". In: *Boundary-Layer Meteorology* 132.3, 415—436.

Brosy, Caroline et al. (2017). “Simultaneous multicopter-based air sampling and sensing of meteorological variables”. In: *Atmospheric Measurement Techniques* 10, pp. 2773–2784.

Brutsaert, Wilfried (1998). “Land-surface water vapor and sensible heat flux: Spatial variability, homogeneity, and measurement scales”. In: *Water Resources Research* 34.10, pp. 2433–2442.

Businger, Joost A. (1982). “Atmospheric turbulence and air pollution modelling”. In: ed. by Frans T Nieuwstadt and Han Van Dop. Reidel. Chap. Equations and concepts, pp. 1–36.

Businger, Joost A. et al. (1971). “Flux-profile relationships in the atmospheric surface layer”. In: *Journal of the atmospheric Sciences* 28.2, pp. 181–189.

Catalano, Franco and Chin-Hoh Moeng (2010). “Large-eddy simulation of the daytime boundary layer in an idealized valley using the Weather Research and Forecasting numerical model”. In: *Boundary-Layer Meteorology* 137.1, pp. 49–75.

Caughey, SJ, JC Wyngaard, and JC Kaimal (1979). “Turbulence in the evolving stable boundary layer”. In: *Journal of the Atmospheric Sciences* 36.6, pp. 1041–1052.

Chen, Qinglin and Chenning Tong (2006). “Investigation of the subgrid-scale stress and its production rate in a convective atmospheric boundary layer using measurement data”. In: *Journal of Fluid Mechanics* 547, pp. 65–104.

Cheng, Yinguo and Wilfried Brutsaert (2005). “Flux-profile relationships for wind speed and temperature in the stable atmospheric boundary layer”. In: *Boundary-Layer Meteorology* 114.3, pp. 519–538.

Chow, Fotini Katopodes and Robert L. Street (May 2009). “Evaluation of Turbulence Closure Models for Large-Eddy Simulation over Complex Terrain: Flow over Askervein Hill”. In: *Journal of Applied Meteorology and Climatology* 48.5, 1050—1065.

Chow, Fotini Katopodes et al. (2005). “Explicit filtering and reconstruction turbulence modeling for large-eddy simulation of neutral boundary layer flow”. In: *Journal of the Atmospheric Sciences* 62.7, pp. 2058–2077.

Chu, Xia et al. (2014). “A case study of radar observations and WRF LES simulations of the impact of ground-based glaciogenic seeding on orographic clouds and precipitation. Part I: Observations and model validations”. In: *Journal of Applied Meteorology and Climatology* 53.10, pp. 2264–2286.

Clarke, Russell Henry and RR Brook (1979). *The Koorin Expedition: atmospheric boundary layer data over tropical savanna land*. Canberra, Department of Science and the Environment.

CLC (2000). *Corine land cover 100 m, ver. 5*. European Environment Agency (©EEA, Copenhagen).

Collins, Sarah N et al. (2013). "Grids in numerical weather and climate models". In: *Climate Change and Regional/Local Responses*. InTech.

Courant, Richard, Kurt Friedrichs, and Hans Lewy (1967). "On the partial difference equations of mathematical physics". In: *IBM journal of Research and Development* 11.2, pp. 215–234.

Crosman, Erik T. and John D. Horel (Apr. 2012). "Idealized Large-Eddy Simulations of Sea and Lake Breezes: Sensitivity to Lake Diameter, Heat Flux and Stability". In: *Boundary-Layer Meteorology* 144.3, 309—328.

Cuijpers, JWM and PG Duynkerke (1993). "Large eddy simulation of trade wind cumulus clouds". In: *Journal of the Atmospheric Sciences* 50.23, pp. 3894–3908.

Cuxart, Joan, Philippe Bougeault, and J-L Redelsperger (2000). "A turbulence scheme allowing for mesoscale and large-eddy simulations". In: *Quarterly Journal of the Royal Meteorological Society* 126.562, pp. 1–30.

Daniels, Megan H. et al. (2016). "A New Vertical Grid Nesting Capability in the Weather Research and Forecasting (WRF) Model". In: *Monthly Weather Review* 144.10, 3725—3747.

De Roo, Frederik and Matthias Mauder (2018). "The influence of idealized surface heterogeneity on virtual turbulent flux measurements". In: *Atmospheric Chemistry and Physics* 18.7, pp. 5059–5074.

Deardorff, James W (1970). "A three-dimensional numerical investigation of the idealized planetary boundary layer". In: *Geophysical and Astrophysical Fluid Dynamics* 1.3-4, pp. 377–410.

– (1972). "Numerical investigation of neutral and unstable planetary boundary layers". In: *Journal of the Atmospheric Sciences* 29.1, pp. 91–115.

– (1974). "Three-dimensional numerical study of the height and mean structure of a heated planetary boundary layer". In: *Boundary-Layer Meteorology* 7.1, pp. 81–106.

– (1980). "Stratocumulus-capped mixed layers derived from a three-dimensional model". In: *Boundary-Layer Meteorology* 18.4, pp. 495–527.

Dipankar, Anurag et al. (2015). "Large eddy simulation using the general circulation model ICON". In: *Journal of Advances in Modeling Earth Systems* 7.3, pp. 963–986.

Dyer, AJ (1974). "A review of flux-profile relationships". In: *Boundary-Layer Meteorology* 7.3, pp. 363–372.

ECMWF (2009, updated monthly). *ERA-Interim Project*. Research Data Archive at the National Center for Atmospheric Research, Computational and Information Systems Laboratory. Boulder CO. DOI: `10.5065/D6CR5RD9`.

Eder, Fabian et al. (2015). “Secondary circulations at a solitary forest surrounded by semi-arid shrubland and their impact on eddy-covariance measurements”. In: *Agricultural and Forest Meteorology* 211, pp. 115–127.

Etling, D.O. and R.A. Brown (1993). “Roll vortices in the planetary boundary layer: A review”. In: *Boundary-Layer Meteorology* 65.3, pp. 215–248.

Fairall, Chris W et al. (1996). “Bulk parameterization of air-sea fluxes for tropical ocean-global atmosphere coupled-ocean atmosphere response experiment”. In: *Journal of Geophysical Research: Oceans* 101.C2, pp. 3747–3764.

Fersch, B et al. (2018). “Synergies for Soil Moisture Retrieval Across Scales From Airborne Polarimetric SAR, Cosmic Ray Neutron Roving, and an In Situ Sensor Network”. In: *Water Resources Research* 54.11, pp. 9364–9383.

Finnigan, J. J. et al. (2003). “A Re-Evaluation of Long-Term Flux Measurement Techniques Part I: Averaging and Coordinate Rotation”. In: *Boundary-Layer Meteorology* 107.1, pp. 1–48.

Foken, Thomas (2008). “The energy balance closure problem: an overview”. In: *Ecological Applications* 18.6, pp. 1351–1367.

Germano, Massimo et al. (1991). “A dynamic subgrid-scale eddy viscosity model”. In: *Physics of Fluids A: Fluid Dynamics* 3.7, pp. 1760–1765.

Gibbs, Jeremy A. and Evgeni Fedorovich (2014). “Comparison of Convective Boundary Layer Velocity Spectra Retrieved from Large- Eddy-Simulation and Weather Research and Forecasting Model Data”. In: *Journal of Applied Meteorology and Climatology* 53.2, 377—394.

Graf, Maximilian et al. (2016). “Identification and climatology of Alpine pumping from a regional climate simulation”. In: *Frontiers in Earth Science* 4, p. 5.

Grell, Georg A, Jimy Dudhia, David R Stauffer, et al. (1994). “A description of the fifth-generation Penn State/NCAR mesoscale model (MM5)”. In:

Hald, Cornelius et al. (2019). “Large-eddy simulations of real-world episodes in complex terrain based on ERA-reanalysis and validated by ground-based remote sensing data”. In: *Monthly Weather Review* 147.12, pp. 4325–4343.

Harris, Lucas M and Dale R Durran (2010). “An idealized comparison of one-way and two-way grid nesting”. In: *Monthly Weather Review* 138.6, pp. 2174–2187.

Hattori, Yasuo et al. (2010). “Numerical simulation of turbulence structures in the neutral atmospheric surface layer with a mesoscale moteorological model, WRF”. In: *Proceedings of the fifth International Symposium on Computational Wind Engineering*. Vol. 5, p. 385.

Hechtel, Leslie M, Roland B Stull, and Chin-Hoh Moeng (1990). “The effects of nonhomogeneous surface fluxes on the convective boundary layer: A case study using large-eddy simulation". In: *Journal of the Atmospheric Sciences* 47.14, pp. 1721–1741.

Heinze, Rieke et al. (2017). "Large-eddy simulations over Germany using ICON: a comprehensive evaluation". In: *Quarterly Journal of the Royal Meteorological Society* 143.702, pp. 69–100.

Hong, Song-You, Jimy Dudhia, and Shu-Hua Chen (2004). "A revised approach to ice microphysical processes for the bulk parameterization of clouds and precipitation". In: *Monthly Weather Review* 132.1, pp. 103–120.

Huang, Jianping, Xuhui Lee, and Edward G Patton (2008). "A modelling study of flux imbalance and the influence of entrainment in the convective boundary layer". In: *Boundary-layer meteorology* 127.2, pp. 273–292.

Huang, Jing and Elie Bou-Zeid (June 2013). "Turbulence and Vertical Fluxes in the Stable Atmospheric Boundary Layer. Part I: A Large-Eddy Simulation Study". In: *Journal of the Atmospheric Sciences* 70.6, 1513—1527.

Huang, Jing, Elie Bou-Zeid, and Jean-Christophe Golaz (2013). "Turbulence and vertical fluxes in the stable atmospheric boundary layer. Part II: A novel mixing-length model". In: *Journal of the Atmospheric Sciences* 70.6, pp. 1528–1542.

Hutchinson, Todd A (2007). "An adaptive time-step for increased model efficiency". In: *Extended Abstracts, Eighth WRF Users' Workshop*.

Iacono, Michael J et al. (2008). "Radiative forcing by long-lived greenhouse gases: Calculations with the AER radiative transfer models". In: *Journal of Geophysical Research: Atmospheres* 113.D13.

Imukova, K et al. (2016). "Energy balance closure on a winter wheat stand: comparing the eddy covariance technique with the soil water balance method". In: *Biogeosciences* 13.1, pp. 63–75.

Inagaki, Atsushi et al. (2006). "Impact of surface heterogeneity on energy imbalance: a study using LES". In: *Journal of the Meteorological Society of Japan. Ser. II* 84.1, pp. 187–198.

Izumi, Yutaka (1971). *Kansas 1968 Field Program Data Report.* Tech. rep. Air Force Cambridge Research Labs LG Hanscom Field Mass.

Jacobson, Mark Z (2005). *Fundamentals of atmospheric modeling*. Cambridge university press.

Janjić, Zavisa I (1989). "On the pressure gradient force error in σ-coordinate spectral models". In: *Monthly Weather Review* 117.10, pp. 2285–2292.

– (1996). "The surface layer parameterization in the NCEP Eta Model". In: *World Meteorological Organization-Publications-WMO TD*, pp. 4–16.

Jiménez, Pedro A et al. (2012). "A revised scheme for the WRF surface layer formulation". In: *Monthly Weather Review* 140.3, pp. 898–918.

Kaimal, Jagadish Chandran and John J Finnigan (1994). *Atmospheric boundary layer flows: their structure and measurement*. Oxford University Press.

Kanda, Manabu et al. (2004). "LES study of the energy imbalance problem with eddy covariance fluxes". In: *Boundary-Layer Meteorology* 110.3, pp. 381–404.

Khanna, Samir and James G Brasseur (1997). "Analysis of Monin–Obukhov similarity from large-eddy simulation". In: *Journal of Fluid Mechanics* 345, pp. 251–286.

Kiese, R et al. (2018). "The TERENO Pre-Alpine Observatory: Integrating meteorological, hydrological, and biogeochemical measurements and modeling". In: *Vadose Zone Journal* 17.1.

Kirkil, Gokhan et al. (2012). "Implementation and Evaluation of Dynamic Subfilter-Scale Stress Models for Large-Eddy Simulation Using WRF". In: *Monthly Weather Review* 140.1, pp. 266–284.

Klose, Martina and Yaping Shao (Mar. 2013). "Large-eddy simulation of turbulent dust emission". In: *Aeolian Research* 8, 49—58.

Kosović, Branko (1997). "Subgrid-scale modelling for the large-eddy simulation of high-Reynolds-number boundary layers". In: *Journal of Fluid Mechanics* 336, pp. 151–182.

Kosović, Branko and Judith A Curry (2000). "A large eddy simulation study of a quasi-steady, stably stratified atmospheric boundary layer". In: *Journal of the Atmospheric Sciences* 57.8, pp. 1052–1068.

Kraus, Helmut, Jürgen Malcher, and Eberhard Schaller (1985). "A nocturnal low level jet during PUKK". In: *Boundary-Layer Meteorology* 31.2, pp. 187–195.

Kučerová, Monika et al. (2017). "Trends in frequency and persistence of atmospheric circulation types over Europe derived from a multitude of classifications". In: *International Journal of Climatology* 37.5, pp. 2502–2521.

Kunstmann, Harald, J Krause, and S Mayr (2006). "Inverse distributed hydrological modelling of Alpine catchments". In: *Hydrology and Earth System Sciences Discussions* 10.3, pp. 395–412.

Kunstmann, Harald et al. (2004). "Impact analysis of climate change for an Alpine catchment using high resolution dynamic downscaling of ECHAM4 time slices". In: *Hydrology and Earth System Sciences Discussions* 8.6, pp. 1031–1045.

Lamaud, E et al. (2001). "Validation of eddy flux measurements above the understorey of a pine forest". In: *Agricultural and Forest Meteorology* 106.3, pp. 187–203.

Lang, MN, A Gohm, and JS Wagner (2015). "The impact of embedded valleys on daytime pollution transport over a mountain range". In: *Atmospheric Chemistry and Physics* 15.20, pp. 11981–11998.

Lanzinger, Eckhard and Hans Langmack (2005). "Measuring air temperature by using an ultrasonic anemometer". In: *Technical Conference on*

Meteorological and Environmental Instruments and Methods of Observation (TECO-2005), WMO Tech. Doc. 1265, P3.

Laux, Patrick and Harald Kunstmann (2008). "Detection of regional weekly weather cycles across Europe". In: *Environmental Research Letters* 3.4, p. 044005.

LeMone, Margaret A (1973). "The structure and dynamics of horizontal roll vortices in the planetary boundary layer". In: *Journal of the Atmospheric Sciences* 30.6, pp. 1077–1091.

– (1976). "Modulation of turbulence energy by longitudinal rolls in an unstable planetary boundary layer". In: *Journal of the Atmospheric Sciences* 33.7, pp. 1308–1320.

Leonard, A (1975). "Energy cascade in large-eddy simulations of turbulent fluid flows". In: *Advances in geophysics*. Vol. 18. Elsevier, pp. 237–248.

Lettau, Heinz and Ben Davidson (1957). "Exploring the Atmosphere's First Mile: Proceedings of the Great Plains Turbulence Field Program, 1 August to 8 September 1953, O'Neill, Nebraska". In: Symposium Publications Division, Pergamon Press.

Lilly, DK (1967). "The representation of small-scale turbulence in numerical simulation experiments". In: *Proc. IBM Sci. Compt. Symp. Environ. Sci., White Plains, IBM, 1967*.

Liu, Yubao et al. (2011). "Simultaneous nested modeling from the synoptic scale to the LES scale for wind energy applications". In: *Journal of Wind Engineering and Industrial Aerodynamics* 99.4, pp. 308–319.

Ludwig, Francis L, Fotini Katopodes Chow, and Robert L Street (2009). "Effect of turbulence models and spatial resolution on resolved velocity structure and momentum fluxes in large-eddy simulations of neutral boundary layer flow". In: *Journal of Applied Meteorology and Climatology* 48.6, pp. 1161–1180.

Lugauer, Matthias and Peter Winkler (2005). "Thermal circulation in South Bavaria–climatology and synoptic aspects". In: *Meteorologische Zeitschrift* 14.1, pp. 15–30.

Lundquist, Julie K, JD Mirocha, and Branko Kosovic (2010). "Nesting large-eddy simulations within mesoscale simulations in WRF for wind energy applications". In: *Proceedings of the Fifth International Symposium on Computational Wind Engineering, Chapel Hill, NC, May*, pp. 23–27.

Lundquist, Katherine A, Fotini Katopodes Chow, and Julie K Lundquist (Mar. 2010a). "An Immersed Boundary Method for the Weather Research and Forecasting Model". In: *Monthly Weather Review* 138.3, 796—817.

– (2010b). "Numerical errors in flow over of steep topography: analysis and alternatives". In: *14th Conference on Mountain Meteorology*.

Marusic, Ivan, Gary J Kunkel, and Fernando Porté-Agel (2001). "Experimental study of wall boundary conditions for large-eddy simulation". In: *Journal of Fluid Mechanics* 446, pp. 309–320.

Mason, Paul J (1989). "Large-eddy simulation of the convective atmospheric boundary layer". In: *Journal of the Atmospheric Sciences* 46.11, pp. 1492–1516.

– (1994). "Large-eddy simulation: A critical review of the technique". In: *Quarterly Journal of the Royal Meteorological Society* 120.515, pp. 1–26.

Mason, Paul J and SH Derbyshire (1990). "Large-eddy simulation of the stably-stratified atmospheric boundary layer". In: *Boundary-layer meteorology* 53.1-2, pp. 117–162.

Mason, Paul J and David J Thomson (1992). "Stochastic backscatter in large-eddy simulations of boundary layers". In: *Journal of Fluid Mechanics* 242, pp. 51–78.

Mauder, Matthias and Thomas Foken (2006). "Impact of post-field data processing on eddy covariance flux estimates and energy balance closure". In: *Meteorologische Zeitschrift* 15.6, pp. 597–609.

– (2011). "Documentation and instruction manual of the eddy-covariance software package TK3". In: *Arbeitsergebnisse der Uni Bayreuth* 46.

Mirocha, Jeff, Branko Kosović, and Gokhan Kirkil (2014). "Resolved turbulence characteristics in large-eddy simulations nested within mesoscale simulations using the Weather Research and Forecasting Model". In: *Monthly Weather Review* 142.2, pp. 806–831.

Mirocha, Jeff, Julie K Lundquist, and Branko Kosović (2010). "Implementation of a nonlinear subfilter turbulence stress model for large-eddy simulation in the Advanced Research WRF model". In: *Monthly Weather Review* 138.11, pp. 4212–4228.

Mirocha, Jeff et al. (2013). "Transition and Equilibration of Neutral Atmospheric Boundary Layer Flow in One-Way Nested Large-Eddy Simulations Using the Weather Research and Forecasting Model". In: *Monthly Weather Review* 141.3, 918—940.

Mirocha, Jeff et al. (2014). "Implementation of a generalized actuator disk wind turbine model into the weather research and forecasting model for large-eddy simulation applications". In: *Journal of Renewable and Sustainable Energy* 6.1, p. 013104.

Moeng, Chin-Hoh (1984). "A large-eddy-simulation model for the study of planetary boundary-layer turbulence". In: *Journal of the Atmospheric Sciences* 41.13, pp. 2052–2062.

– (1986). "Large-eddy simulation of a stratus-topped boundary layer. Part I: Structure and budgets". In: *Journal of the Atmospheric Sciences* 43.23, pp. 2886–2900.

Moeng, Chin-Hoh (1987). “Large-eddy simulation of a stratus-topped boundary layer. Part II: Implications for mixed-layer modeling”. In: *Journal of the Atmospheric Sciences* 44.12, pp. 1605–1614.

Moeng, Chin-Hoh and Peter P Sullivan (1994). “A comparison of shear- and buoyancy-driven planetary boundary layer flows”. In: *Journal of the Atmospheric Sciences* 51.7, pp. 999–1022.

Moeng, Chin-Hoh et al. (2007). “Examining two-way grid nesting for large eddy simulation of the PBL using the WRF model”. In: *Monthly Weather Review* 135.6, pp. 2295–2311.

Monin, Andreĭ Sergeevich and Aleksandr Mikhaĭlovich Obukhov (1954). “Basic laws of turbulent mixing in the surface layer of the atmosphere”. In: *Contrib. Geophys. Inst. Acad. Sci. USSR* 151.163, e187.

Muñoz-Esparza, Domingo and Branko Kosović (2018). “Generation of inflow turbulence in large-eddy simulations of non-neutral atmospheric boundary layers with the cell perturbation method”. In: *Monthly Weather Review* 146.6, pp. 1889–1909.

Muñoz-Esparza, Domingo et al. (2014a). “Bridging the transition from mesoscale to microscale turbulence in numerical weather prediction models”. In: *Boundary-layer meteorology* 153.3, pp. 409–440.

Muñoz-Esparza, Domingo et al. (2014b). “Nesting turbulence in an offshore convective boundary layer using large-eddy simulations”. In: *Boundary-layer meteorology* 151.3, pp. 453–478.

Muñoz-Esparza, Domingo et al. (2017). “Coupled mesoscale-LES modeling of a diurnal cycle during the CWEX-13 field campaign: From weather to boundary-layer eddies”. In: *Journal of Advances in Modeling Earth Systems* 9.3, pp. 1572–1594.

NASA/METI/AIST/Japan Spacesystems and U.S./Japan ASTER Science Team (2009). *ASTER Global Digital Elevation Model*. distributed by NASA EOSDIS Land Processes DAAC. DOI: `10.5067/ASTER/ASTGTM.002`.

Newman, Jennifer F et al. (2016). “Testing and validation of multi-lidar scanning strategies for wind energy applications”. In: *Wind Energy* 19.12, pp. 2239–2254.

Nieuwstadt, Frans TM (1990). “Direct and large-eddy simulation of free convection”. In: *Proc. Ninth Int. Heat Transfer Conf.* Vol. 1, pp. 37–47.

Nieuwstadt, Frans TM et al. (1993). “Large-eddy simulation of the convective boundary layer: A comparison of four computer codes”. In: *Turbulent Shear Flows 8*. Springer, pp. 343–367.

Nunalee, Christopher G, Branko Kosović, and Paul E Bieringer (2014). “Eulerian dispersion modeling with WRF-LES of plume impingement in neutrally and stably stratified turbulent boundary layers”. In: *Atmospheric environment* 99, pp. 571–581.

Pasquill, F (1972). “Some aspects of boundary layer description”. In: *Quarterly Journal of the Royal Meteorological Society* 98.417, pp. 469–494.

Phillips, Norman A (1957). “A coordinate system having some special advantages for numerical forecasting”. In: *Journal of Meteorology* 14.2, pp. 184–185.

Pielke Sr, Roger A (2013). *Mesoscale meteorological modeling*. Vol. 98. Academic press.

Rai, K et al. (2017). “Comparison of Measured and Numerically Simulated Turbulence Statistics in a Convective Boundary Layer Over Complex Terrain”. In: *Boundary-Layer Meteorology* 163.1, pp. 69–89.

Raupach, MR (1979). “Anomalies in flux-gradient relationships over forest”. In: *Boundary-Layer Meteorology* 16.3, pp. 467–486.

Rotach, Mathias Walter et al. (2015). “On the vertical exchange of heat, mass and momentum over complex, mountainous terrain”. In: *Frontiers in Earth Science* 3, p. 76.

Saiki, Eileen M, Chin-Hoh Moeng, and Peter P Sullivan (2000). “Large-eddy simulation of the stably stratified planetary boundary layer”. In: *Boundary-Layer Meteorology* 95.1, pp. 1–30.

Schalkwijk, Jerôme, Harm JJ Jonker, and A Pier Siebesma (2016). “An investigation of the eddy-covariance flux imbalance in a year-long large-eddy simulation of the weather at Cabauw”. In: *Boundary-layer meteorology* 160.1, pp. 17–39.

Schär, Christoph et al. (2002). “A new terrain-following vertical coordinate formulation for atmospheric prediction models”. In: *Monthly Weather Review* 130.10, pp. 2459–2480.

Schmidt, Helmut and Ulrich Schumann (1989). “Coherent structure of the convective boundary layer derived from large-eddy simulations”. In: *Journal of Fluid Mechanics* 200, pp. 511–562.

Seidel, Dian J, Chi O Ao, and Kun Li (2010). “Estimating climatological planetary boundary layer heights from radiosonde observations: Comparison of methods and uncertainty analysis”. In: *Journal of Geophysical Research: Atmospheres* 115.D16.

Shen, Shaohua and Monique Y Leclerc (1995). “How large must surface inhomogeneities be before they influence the convective boundary layer structure? A case study”. In: *Quarterly Journal of the Royal Meteorological Society* 121.526, pp. 1209–1228.

Shin, Hyeyum Hailey and Song-You Hong (2013). “Analysis of Resolved and Parameterized Vertical Transports in Convective Boundary Layers at Gray-Zone Resolutions”. In: *Journal of the Atmospheric Sciences* 70.10, 3248—3261.

Siebesma, A Pier et al. (2003). "A large eddy simulation intercomparison study of shallow cumulus convection". In: *Journal of the Atmospheric Sciences* 60.10, pp. 1201–1219.

Skamarock, WC et al. (2008). "A description of the advanced research WRF version 3: NCAR/TN-475". In: *STR, NCAR technical note. NCAR, Boulder* 88.

Smagorinsky, Joseph (1963). "General circulation experiments with the primitive equations: I. the basic experiment*". In: *Monthly Weather Review* 91.3, pp. 99–164.

Soltani, Mohsen et al. (2017). "Turbulent flux variability and energy balance closure in the TERENO prealpine observatory: a hydrometeorological data analysis". In: *Theoretical and applied climatology*, pp. 1–20.

Sommeria, Gilles (1976). "Three-dimensional simulation of turbulent processes in an undisturbed trade wind boundary layer". In: *Journal of the Atmospheric Sciences* 33.2, pp. 216–241.

Sorbjan, Zbigniew (1986). "On similarity in the atmospheric boundary layer". In: *Boundary-Layer Meteorology* 34.4, pp. 377–397.

– (1996). "Effects caused by varying the strength of the capping inversion based on a large eddy simulation model of the shear-free convective boundary layer". In: *Journal of the atmospheric sciences* 53.14, pp. 2015–2024.

– (2004). "AIR QUALITY MODELING - Theories, Methodologies, Computational Techniques, and Available Databases and Software. Vol. II – Advanced Topics". In: ed. by P. Zannetti. The EnviroComp Institute and Air & Waste Management Association. Chap. 5B Large-Eddy Simulations of the Atmospheric Boundary Layer.

– (2007). "A numerical study of daily transitions in the convective boundary layer". In: *Boundary-layer meteorology* 123.3, pp. 365–383.

Stawiarski, Christina et al. (2013). "Scopes and challenges of dual-Doppler lidar wind measurements—an error analysis". In: *Journal of Atmospheric and Oceanic Technology* 30.9, pp. 2044–2062.

Steinfeld, Gerald et al. (2007). "Spatial representativeness of single tower measurements and the imbalance problem with eddy-covariance fluxes: results of a large-eddy simulation study". In: *Boundary-Layer Meteorology* 123.1, pp. 77–98.

Stoll, Rob and Fernando Porté-Agel (2006). "Dynamic subgrid-scale models for momentum and scalar fluxes in large-eddy simulations of neutrally stratified atmospheric boundary layers over heterogeneous terrain". In: *Water Resources Research* 42.1.

Stull, Roland B (1988). *An introduction to boundary layer meteorology*. Vol. 13. Springer Science & Business Media.

Stull, Roland B and Edwin W Eloranta (1984). "Boundary layer experiment—1983". In: *Bulletin of the American Meteorological Society* 65.5, pp. 450–456.

Sühring, Matthias and Siegfried Raasch (2013). "Heterogeneity-induced heat-flux patterns in the convective boundary layer: can they be detected from observations and is there a blending height?—a large-eddy simulation study for the LITFASS-2003 experiment". In: *Boundary-layer meteorology* 148.2, pp. 309–331.

Sullivan, Peter P, James C McWilliams, and Chin-Hoh Moeng (1994). "A subgrid-scale model for large-eddy simulation of planetary boundary-layer flows". In: *Boundary-Layer Meteorology* 71.3, pp. 247–276.

– (1996). "A grid nesting method for large-eddy simulation of planetary boundary-layer flows". In: *Boundary-Layer Meteorology* 80.1-2, pp. 167–202.

Sullivan, Peter P et al. (1998). "Structure of the entrainment zone capping the convective atmospheric boundary layer". In: *Journal of the atmospheric sciences* 55.19, pp. 3042–3064.

Sullivan, Peter P et al. (2003). "Structure of subfilter-scale fluxes in the atmospheric surface layer with application to large-eddy simulation modelling". In: *Journal of Fluid Mechanics* 482, pp. 101–139.

Sullivan, Peter P et al. (2016). "Turbulent winds and temperature fronts in large-eddy simulations of the stable atmospheric boundary layer". In: *Journal of the Atmospheric Sciences* 73.4, pp. 1815–1840.

Talbot, Charles, Elie Bou-Zeid, and Jim Smith (Oct. 2012). "Nested Mesoscale Large-Eddy Simulations with WRF: Performance in Real Test Cases". In: *Journal of Hydrometeorology* 13.5, 1421—1441. ISSN: 1525-7541. DOI: `10.1175/jhm-d-11-048.1`.

Turnipseed, AA et al. (2002). "Energy budget above a high-elevation subalpine forest in complex topography". In: *Agricultural and Forest Meteorology* 110.3, pp. 177–201.

Udina, Mireia et al. (2016). "Exploring Vertical Turbulence Structure in Neutrally and Stably Stratified Flows Using the Weather Research and Forecasting–Large-Eddy Simulation (WRF–LES) Model". In: *Boundary-Layer Meteorology* 161.2, pp. 355–374.

Van der Hoven, Isaac (1957). "Power spectrum of horizontal wind speed in the frequency range from 0.0007 to 900 cycles per hour". In: *Journal of meteorology* 14.2, pp. 160–164.

Vasiljević, Nikola et al. (2017). "Perdigão 2015: methodology for atmospheric multi-Doppler lidar experiments". In: *Atmospheric Measurement Techniques* 10.9, pp. 3463–3483.

Wagner, Johannes S., Alexander Gohm, and Mathias W. Rotach (2014). "The Impact of Horizontal Model Grid Resolution on the Boundary Layer

Structure over an Idealized Valley". In: *Monthly Weather Review* 142.9, 3446—3465.

Wagner, JS, A Gohm, and MW Rotach (2015). "The impact of valley geometry on daytime thermally driven flows and vertical transport processes". In: *Quarterly Journal of the Royal Meteorological Society* 141.690, pp. 1780–1794.

Walko, Robert L, William R Cotton, and Roger A Pielke (1992). "Large-eddy simulations of the effects of hilly terrain on the convective boundary layer". In: *Boundary-Layer Meteorology* 58.1-2, pp. 133–150.

Wicker, Louis J and William C Skamarock (1998). "A time-splitting scheme for the elastic equations incorporating second-order Runge–Kutta time differencing". In: *Monthly Weather Review* 126.7, pp. 1992–1999.

– (2002). "Time-splitting methods for elastic models using forward time schemes". In: *Monthly weather review* 130.8, pp. 2088–2097.

Wieringa, J (1976). "An objective exposure correction method for average wind speeds measured at a sheltered location". In: *Quarterly Journal of the Royal Meteorological Society* 102.431, pp. 241–253.

Wolf, Benjamin et al. (2017). "The SCALEX Campaign: Scale-Crossing Land Surface and Boundary Layer Processes in the TERENO-preAlpine Observatory". In: *Bulletin of the American Meteorological Society* 98.6, pp. 1217–1234.

Wyngaard, John C (2004). "Toward numerical modeling in the "Terra Incognita"". In: *Journal of the Atmospheric Sciences* 61.14, pp. 1816–1826.

Xue, Lulin et al. (2016). "A case study of radar observations and WRF LES simulations of the impact of ground-based glaciogenic seeding on orographic clouds and precipitation. Part II: AgI dispersion and seeding signals simulated by WRF". In: *Journal of Applied Meteorology and Climatology* 55.2, pp. 445–464.

Yamaguchi, Takanobu and Graham Feingold (Mar. 2012). "Technical note: Large-eddy simulation of cloudy boundary layer with the Advanced Research WRF model". In: *Journal of Advances in Modeling Earth Systems* 4.3.

Zacharias, Steffen et al. (2011). "A network of terrestrial environmental observatories in Germany". In: *Vadose Zone Journal* 10.3, pp. 955–973.

Zängl, Günther et al. (2015). "The ICON (ICOsahedral Non-hydrostatic) modelling framework of DWD and MPI-M: Description of the non-hydrostatic dynamical core". In: *Quarterly Journal of the Royal Meteorological Society* 141.687, pp. 563–579.

Zeeman, MJ et al. (2017). "Reduced snow cover affects productivity of upland temperate grasslands". In: *Agricultural and forest meteorology* 232, pp. 514–526.

Zhang, Dalin and Richard A Anthes (1982). “A high-resolution model of the planetary boundary layer—Sensitivity tests and comparisons with SESAME-79 data”. In: *Journal of Applied Meteorology* 21.11, pp. 1594–1609.

Zhou, Yanzhao et al. (2018). “Diurnal variations of the flux imbalance over homogeneous and heterogeneous landscapes”. In: *Boundary-layer meteorology* 168.3, pp. 417–442.